EDGEWOOD

CHEMICAL BIOLOGICAL CENTER

U.S. ARMY SOLDIER AND BIOLOGICAL CHEMICAL COMMAND

ECBC-SP-006

PROCEEDINGS OF THE 1998 SCIENTIFIC CONFERENCE ON OBSCURATION AND AEROSOL RESEARCH

Amy L. Coverstone
Heather L. Cowan
Alice I. Vickers

BATTELLE EDGEWOOD OPERATIONS
Bel Air, MD 21015

Edward W. Stuebing

RESEARCH AND TECHNOLOGY DIRECTORATE

October 1999

20000426 053

Aberdeen Proving Ground, MD 21010-5424

DTIC QUALITY INSPECTED 3

Disclaimer

The findings in this report are not to be construed as an official Department of the Army position unless so designated by other authorizing documents.

REPORT DOCUMENTATION PAGE

1. AGENCY USE ONLY (Leave blank)	2. REPORT DATE 1999 October	3. REPORT TYPE AND DATES COVERED Final; 1998 December

4. TITLE AND SUBTITLE

Proceedings of the 1998 Scientific Conference on Obscuration and Aerosol Research

5. FUNDING NUMBERS

PR-10161102A71A

6. AUTHOR(S)

Coverstone, Amy L.; Cowan, Heather L.; Vickers, Alice I. (Battelle); and Stuebing, Edward W. (ECBC)*

7. PERFORMING ORGANIZATION NAME(S) AND ADDRESS(ES)

Battelle Edgewood Operations, 2012 Tollgate Road, Suite 206, Bel Air, MD 21015

DIR, ECBC, ATTN: AMSSB-RRT-TA, APG, MD 21010-5424

8. PERFORMING ORGANIZATION REPORT NUMBER

ECBC-SP-006

9. SPONSORING/MONITORING AGENCY NAME(S) AND ADDRESS(ES)

DIR, ECBC, ATTN: AMSSB-RRT-TA, APG, MD 21010-5424

10. SPONSORING/MONITORING AGENCY REPORT NUMBER

11. SUPPLEMENTARY NOTES

* When this conference was conducted, the U.S. Army Edgewood Chemical Biological Center (ECBC) was known as the U.S. Army Edgewood Research, Development and Engineering Center (ERDEC).

12a. DISTRIBUTION/AVAILABILITY STATEMENT

Approved for public release; distribution is unlimited.

12b. DISTRIBUTION CODE

13. ABSTRACT (Maximum 200 words)

The 1998 Scientific Conference on Obscuration and Aerosol Research was held 16-18 June 1998, at the Edgewood Area Conference Center, Aberdeen Proving Ground, MD, USA. The program consisted of 38 presentations on Obscuration and Aerosol Research. Subject areas included: Aerosol Particle Generation and Dynamics, Aerosol Characterization Methods-Aerosol Samplers and Collectors, Preparing, Aerosolizing and Characterizing Erwinia Herbicola, and Optical Properties of Aerosols. There were over 96 people in attendance.

14. SUBJECT TERMS

Obscurants	Aerosol	Extinction	Transmission
Obscuration	Aerosols	Absorption	Infrared
Scattering	Sizing	Smoke	

15. NUMBER OF PAGES

120

16. PRICE CODE

17. SECURITY CLASSIFICATION OF REPORT	18. SECURITY CLASSIFICATION OF THIS PAGE	19. SECURITY CLASSIFICATION OF ABSTRACT	20. LIMITATION OF ABSTRACT
UNCLASSIFIED	UNCLASSIFIED	UNCLASSIFIED	UL

THIS PAGE INTENTIONALLY LEFT BLANK

PREFACE

The 1998 Scientific Conference on Obscuration and Aerosol Research was held 16 - 18 June 1998 at the Edgewood Area Conference Center on Aberdeen Proving Ground, MD, USA. This year's conference was organized under the direction of Dr. Edward Stuebing, U.S. Army Edgewood Chemical Biological Center (ECBC).

This report was authorized under Project No. 10161102A71A, CB Defense Assessment Technology.

The participants develop some familiarity with the U. S. Army aerosol and obscuration science research programs and also become personally acquainted with the other investigators and their research interests and capabilities. Each attendee is invited to present any aspect of a topic of interest and may make either last minute changes or alterations in this presentation as the flow of ideas in the Conference develops.

While all participants in the Conference are invited to submit papers for the proceedings of the Conference, each investigator, who is funded by the U. S. Army Research Program, is requested to provide one or more written papers that document specifically the progress made in his funded effort during the previous year and indicate future directions. Also, the papers for the proceedings are collected in the Fall to allow time for the fresh ideas that arise at the Conference to be incorporated. Therefore, while the papers in these proceedings tend to closely correspond to what was presented at the Conference, there is not an exact correspondence.

When this conference was held, ECBC was known as the U.S. Army Edgewood Research, Development and Engineering Center (ERDEC).

THIS PAGE INTENTIONALLY LEFT BLANK

CONTENTS

AEROSOL PARTICLE GENERATION AND DYNAMICS

AEROSOL CHARACTERIZATION METHODS-AEROSOL SAMPLERS AND COLLECTORS

WORKSHOP: PREPARING, AEROSOLIZING AND CHARACTERIZING ERWINIA HERBICOLA

POSTER PROGRAM

OPTICAL PROPERTIES OF AEROSOLS

INDEXES

APPENDIXES

Aerosol Particle Generation and Dynamics

THIS PAGE INTENTIONALLY LEFT BLANK

SIMULATING AIRFLOW AND DISPERSION OF AEROSOL OVER VARIABLE TERRAIN AND LAND MORPHOLOGY FEATURES

RONALD M. CIONCO

US ARMY RESEARCH LABORATORY
ATTN: AMSRL-IS-EE   (e-mail: rcionco@arl.mil)
2800 POWDER MILL ROAD
ADELPHI, MD 20783

RECENT PUBLICATIONS AND SUBMITTALS FOR PUBLICATIONS:

Cionco, R. M. And R. Ellefsen, 1998: "High Resolution Urban Morphology Data for Urban Wind Flow Modeling, Atmospheric Environment, Special Issue on Urban Forest", Vol 32, No.1, p7-17 Elsevier Science, Great Britain.

Cionco, R. M. Et al, (Jan 1999): "An Overview of MADONA: A Multi-National Field Study of High Resolution Meteorology and Diffusion over Complex Terrain", Bulletin of the American Meteorological; Society, Boston, MA.

Cionco, R. M., 1998: 'Detection of Boundary Layer Forcing in a Desert Canopy using Wavelet Analysis Methods", 1997 Battlespace Atmospherics Conference, San Diego, CA.

Cionco, R. M. et al, 1998: "High Resolution Meteorological Transport and Diffusion Simulations in a Complex River Valley", 1997 Battlespace Atmospherics Conference, San Diego, CA

Cionco, R. M., 1998: 'Simulating Wind Fields for Different Resolutions of Terrain and Morphological Land Features', Proceedings of the 2nd Symposium on Urban Environment, AMS, Boston, MA

Cionco, R. M., 1998: 'Remote Sensing of Wind Profiles Within and Above an Urban Domain' Proceedings of the 2nd Symposium on Urban Environment, AMS, Boston, MA.

Cionco, R. M., H. Weber, and W. aufm Kampe, 1998: High Resolution Simulations of Meteorology and Diffusion in a Complex River Valley", 23rd Conference on Agricultural and Forest Meteorology, AMS, Boston, MA.

Cionco, R. M., 1998: "High Resolution Modeling and Urban-Related Data Bases', Documentation of the DOD/DOE Meeting on Urban Hazard Modeling, Arlington, VA

RECENT PRESENTATIONS:

"High Resolution Wind Model", 2nd Annual GMU/DSWA Transport and Diffusion Modeling Workshop, George Mason University, Va 1998.

"Simulating Airflow and Dispersion of Aerosol over Variable Terrain and Land Morphology Features", 1998 Scientific Conference on Obscuration and Aerosol Research, ERDEC, MD, 1998 ·

"High Resolution Modeling and Urban-Related Data Bases', DOD/DOE Urban Hazard Modeling Conference, 1998

"High Resolution Modeling and Urban Morphology and Meteorological Data Bases", DSWA HPAC Integration Meeting, Arlington, VA, 1998.

"High Resolution Meteorological Transport and Diffusion Simulations in a Complex River Valley", 1997 Battlespace Atmospherics Conference, San Diego, CA. 1997.

"Detection of Boundary Layer Forcing in a Desert Canopy using Wavelet Analysis Methods", 1997 Battlespace Atmospherics Conference, San Diego, CA 1997.

SEMINARS on high resolution wind modeling and urban meteorology and morphology data bases at:
   Arizona State University, Aerospace and Mechanical Engineering Department, Tempe, AZ
   San Jose State University, Department of Geography, San Jose, CA
   Environmental Protection Agency, Microenvironmental Program, NERL, RTP, NC.

ABSTRACT

When developing a compatible set of airflow and dispersion models for the transport and diffusion of aerosols over variable terrain and changing land features, a variety of simulations must be run to test model responses to a combination of meteorological, terrain, and surface roughness conditions. A gaussian puff dispersion model is selected to be integrated with and driven by a high resolution airflow model. Simulations of the meteorological fields are affected by mechanical and thermal forcing producing terrain- and buoyancy-influenced flow fields. The dispersion model, driven by the high resolution wind fields, analyzes the downwind and lateral gaussian dispersion of puffs of aerosols in these deformed wind fields. The dispersion analysis produces concentration and dosage values and contour plots and also can include plume meander. The simulated high resolution wind fields clearly respond to the variety of meteorological, terrain, and surface roughness conditions posed to the wind model. The resultant solutions exhibit greater deformation and speed changes in the stable atmospheric condition than it did for the unstable condition with its additional buoyancy contribution. Angle of attack of the wind field upon the orientation of the terrain significantly influences the flow field. The diffusion code is easily driven by these simulated wind fields. For stable conditions, plumes exhibit less lateral diffusion and higher concentrations farther downwind than is obtained for unstable conditions.

INTRODUCTION: During the development of a compatible set of airflow and dispersion models for the transport and diffusion of aerosols over variable terrain and changing land features, a variety of simulations are run to test model responses to meteorological, terrain, and surface roughness conditions. A gaussian puff dispersion model is selected to be integrated with and driven by a high resolution airflow model. The high resolution micrometeorological model analyzes the flow field in the lower part of the boundary layer for computational grids of 40 m to 400 m and domains of 2 km x 2 km to 20 km x 20 km. For these simulations, 5 km x 5 km domains with a 100 m grid are imposed. The meteorological fields are affected by mechanical and thermal forcing producing terrain- and buoyancy-influenced flow fields. The dispersion model, driven by the high resolution wind fields, analyzes the downwind and lateral gaussian dispersion of puffs of aerosols in these deformed wind fields. The dispersion analysis produces concentration and dosage values and contour plots and also can include plume meander. Graphics packages are also prepared to plot and view the simulation results of wind vectors, streamlines, turbulence parameters, terrain effects, puff positions, plumes, concentration contours and, of course, contoured terrain and surface element roughness.

SIMULATIONS. Data inputs required to simulate flow and dispersion fields are a) meteorological data at one location of wind speed, direction, temperature, pressure, and an upper air sounding, b) digitized terrain elevation and morphological feature type and height, and c) aerosol source type and strength.

Table I lists the input conditions imposed for terrain and meteorological situations that exhibit minimal, moderate, and strong terrain effects upon surface layer meteorology and dispersion. Only a few solutions will be presented in this brief summary of the research.

TABLE I. A variety of meteorological, terrain, and morphological conditions for simulation

EFFECTS	SPEED	DIRECTION	STABILITY	SURFACE
MINIMAL	2 M/S	90, 180,270, 360,135, & 225°	UNSTABLE	TERRAIN
MODERATE	1-11 M/S	70 - 360°	UNST, NEU, STABLE	TERRAIN & MORPHOLOGY
STRONG	2,5,10 M/S	225,315°	UNSTABLE, STABLE	TERRAIN & MORPHOLOGY
DISPERSION	2 M/S	225,315°	UNSTABLE, STABLE	TERRAIN & MORPHOLOGY

Minimal Effects: Minimum terrain effects are obtained for airflow solutions applied to the Gunpowder Neck Peninsula terrain. Figure 1 shows the contoured terrain (elevations of 0 to 24 m)and water surroundings. Figure 2 exhibits minimal terrain effects upon the flow field as streamlines for this simple set of variable terrain for southeasterly flow at 2 m/s. Initiallizing the simulation with onshore flow produces slight, but notable speed and directional changes over the land area especially along the west edge of the Peninsula and 3 to 4 km inland. By contrast, westerly flow (of 2 m/s) shown in figure 3 interacts with the terrain mass with converging and diverging streamline flow and extensive accelerating and decelerating speed areas over land and to the lee of the Peninsula. Both cases are for unstable afternoon conditions.

Moderate Effects: Solutions previously run for the MADONA field study at Porton Down display moderate terrain effects upon flow fields. Figure 4 presents conoured terrain (80 to 180 m)of forested and grass-covered rolling hills with a uniform wind field for initialization from 255° at 4.0 m/s. Figure 5 shows the results of the somewhat oblique winds interacting with the underlying variable surfaces. Considerable directional deformation is occurring depicted by the streamline flow while extensive areas of speed changes are perturbed by terrain channeling and blocking. Figures 6 and 7 exhibit flow patterns that result from changing the angle of attack of the flow field upon the fixed terrain configuration for more parallel flow of 240° (fig 6) and an additional 15° change to 210° (Fig 7) for another different response. The closer the initial flow aligns with the long axis of the dominant terrain features, the smoother the resultant flow (less deformation (shown)and speed variations (not shown)).

Strong Effects: Stronger terrain interactions with the flow field are obtained for the complex configuration of the Mosel River Valley. Figure 8 sets the terrain and morphology scenario with the river cutting a looping path with steep valley walls of vineyards and forested/farming uplands (villages also exist along the river's edge). The following four simulation cases are initialized, as listed in Table I, with speeds of 2 m/s for pairs of unstable and stable conditions for along main river valley flow and cross main river valley flow. The resultant wind fields exhibit strong contrasting conditions as stability and the wind's angle of attack change.

Figure 9 presents the along main valley flow (225°) of 2 m/s and unstable (day time) conditions. The imposed wind field flows smoothly as it follows the terrain with minor variations occurring downwind from two isolated 'finger' ridges as

APG-EDGEWOOD TERRAIN 5KM X 5KM - 100M
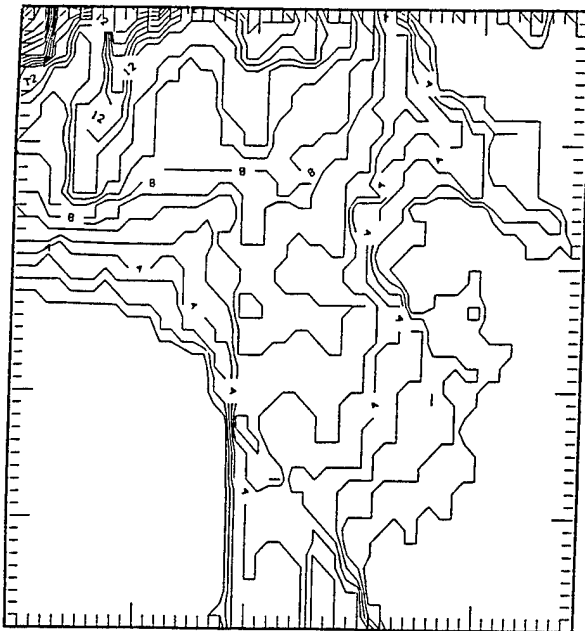
Figure 1. Contours of terrain elevation for Gunpowder Neck Peninsula, MD
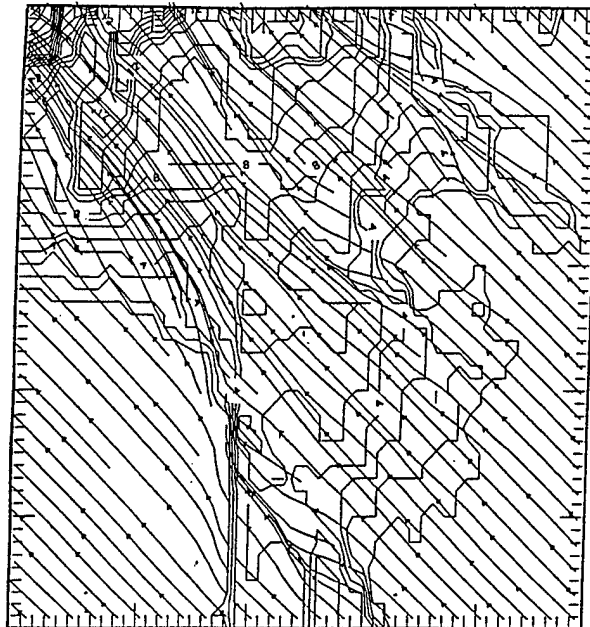
Figure 2. Simulated streamline flow for Southeasterly flow at 2 m/s for GNP
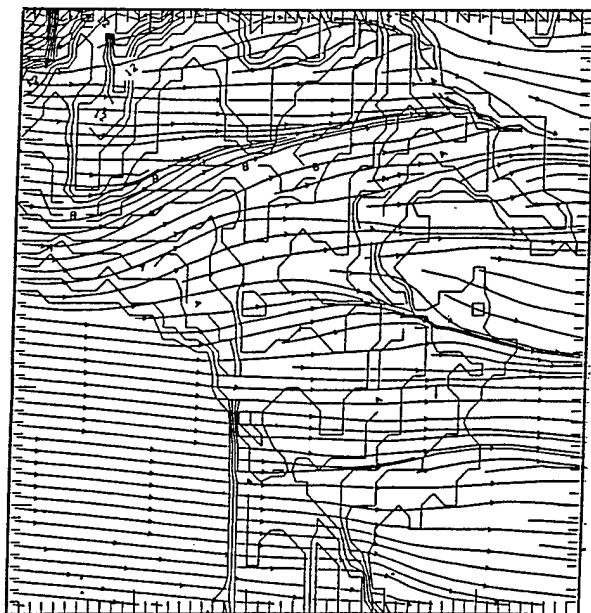
Figure 3. Simulated streamline field for Westerly flow at 2 m/s for GNP.
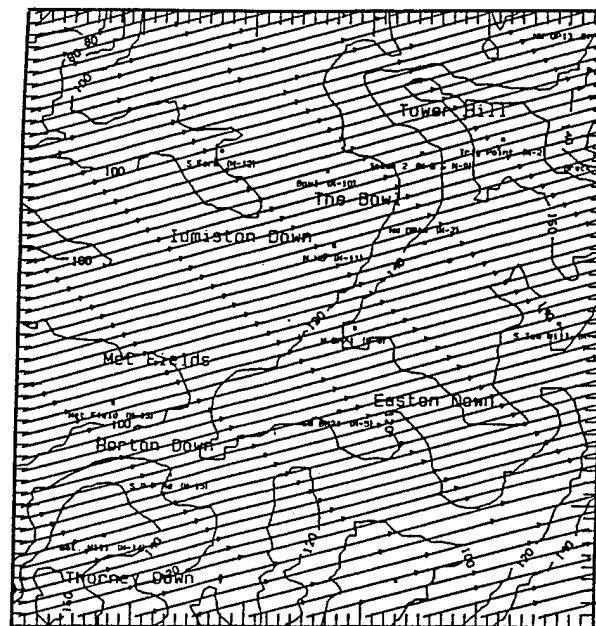
Figure 4. Contoured terrain elevation and an uniform initial flow at Porton Down,

6
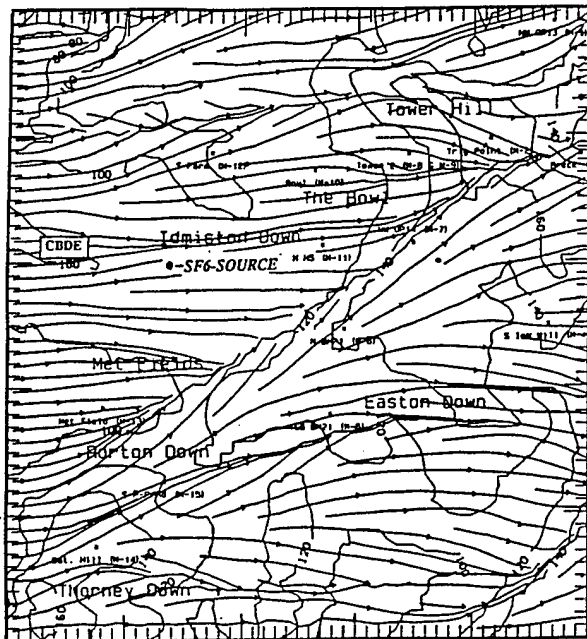
Figure 5.Simulated streamline field for flow oblique to ridge line: 4m/2 @ 255°
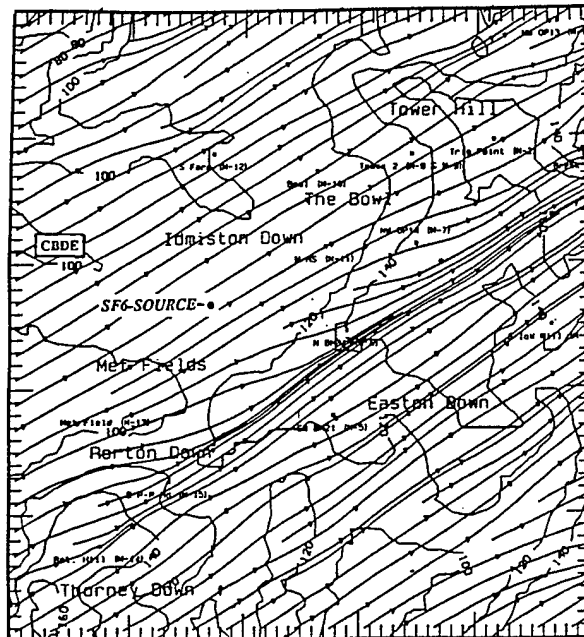
Figure 6. Simulated streamline field for flow parallel to ridge line: 5.5m/s @240
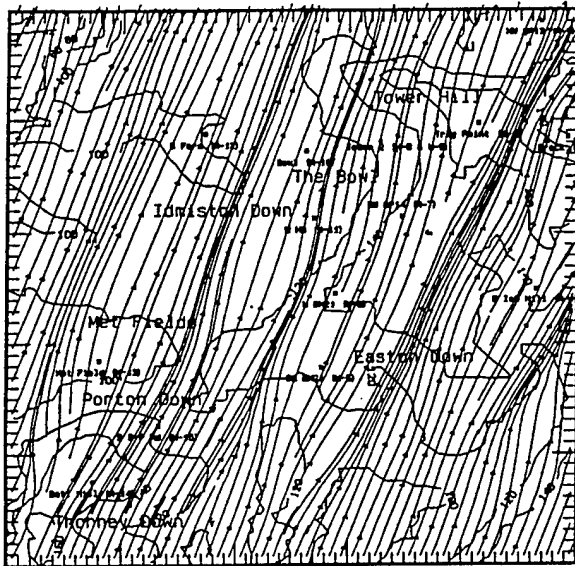
Figure 7. Simulated streamline field for flow oblique to ridge line: 4.5m/2 @210°
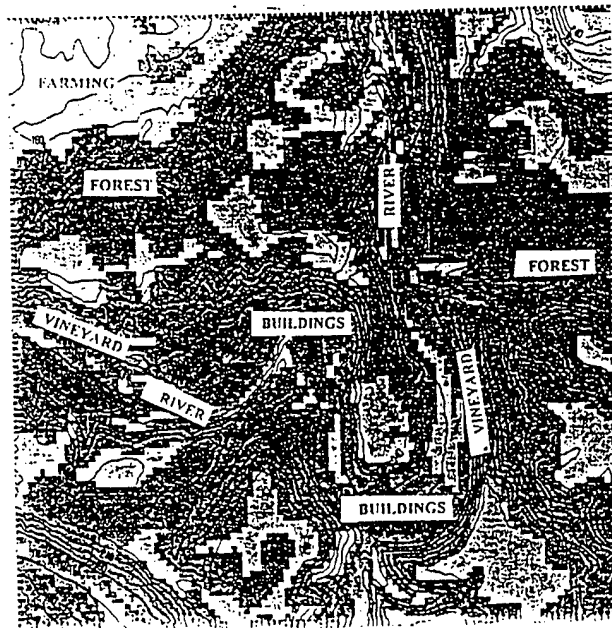
Figure 8. Map of terrain and morphology feature of the Mosel River area.

7

well as along the downwind slope of the Mount Royal 'Loop'. Figure 10 depicts the same along valley flow expect for stable (night) conditions. Changing only the bulk stability, the wind field shows significant down slope accelerations and channeling especially at the river level and over the 'neck' of the 'Loop'.

Figure 11 shows cross valley flow (315^0) of 2 m/s for unstable conditions. By changing the wind direction to cross valley flow but not the speed, this change in the wind's angle of attack produces notable deformation and accelerations enhanced by the orientation of the 'Loop' and some 'finger' ridges as well as some channeling up several canyons which are basically oriented some 315 · . The resultant field shown in figure 11 exhibits more terrain interactions than is apparent in figure 9. Figure 12 displays cross valley flow (315^0) of 2 m/s for stable conditions. Retaining speed and direction but changing the bulk stability generates significant areas of down slope acceleration as well as greatly enhanced up-canyon flow and more areas of along-river-valley flow alignment.

DIFFUSION SIMULATIONS: Calculations of the downwind diffusion of plumes (smoke plumes) driven by the simulated high resolution wind fields of figures 9 through 12 are shown in figures 13, 14, 15, and 16 for conditions of 2 m/s from 225^0 and 315^0 for unstable and stable atmospheric conditions. Note that only every other vector is plotted over the full array of the plume structures.

For the wind field of figure 9, figure 13 shows the release of puffs at two locations in the bottom of the river valley in a wind field of light to moderate deformation. The two plumes are transported in a parallel manner with moderate lateral diffusion and minor steering and the highest concentrations have difficulty leaving the main valley (about 1200 m downwind). Conversely for the stable condition solution of figure 14, the two plumes are released at exactly the same points now in the more stable atmosphere, but now converge while still in the river valley within a field of greater deformation. Higher concentrations also are notable at the east wall (some 1600-1800 m) of the valley (near center of the domain) and even farther downwind (more than 3600 m) into the hills than had occurred in the unstable flow condition.

As the wind direction is rotated to be cross valley, the solution for unstable conditions in figure 15 exhibits a long broad plume with higher concentrations not reaching (about 1200 m) the Mount Royal "loop" (hill in the center of the domain) in a wind field of moderate deformation. For the stable flow condition of figure 16, the plume's higher concentrations travel farther beyond the "loop" to the next hill (about 3800 m) with less lateral diffusion even though the wind field has greater deformation into and out of the river valley.

SUMMARY. During the development and integration of a compatible set of airflow and dispersion models for variable terrain and morphological features scenarios, a variety of simulations were run to test model responses to a combination of conditions. The simulated high resolution wind fields clearly respond to the variety of meteorological, terrain, and surface roughness conditions posed to the wind model. The resultant solutions exhibit greater deformation and speed changes in the stable atmospheric condition than it did for the unstable condition with its additional buoyancy contribution. Angle of attack of the wind field upon the orientation of the terrain significantly influences the flow field. The diffusion code is easily driven by these simulated wind fields. For stable conditions, plumes exhibit less lateral diffusion and higher concentrations farther downwind than is obtained for unstable conditions. Given the proper source type and strength, the code can produce credible plume dispersion of aerosols over and about significant morphological land features driven by these high resolution wind fields.

8

Figure 9.Simulated streamline field for Figure 10. Simulated streamline field
2 m/s wind @ 225° - unstable condition   for 2 m/s wind @ 225° - stable condition
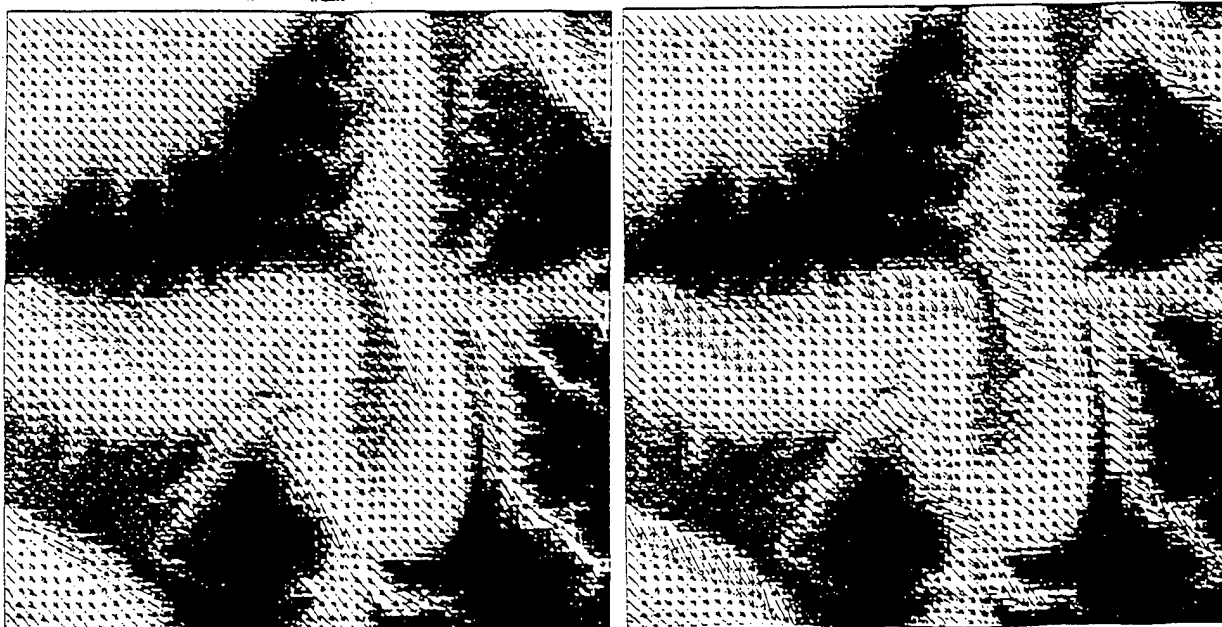
Figure 11.Simulated streamline field for   Figure 12.Simulated streamline field
2m/s wind @ 315° - unstable condition   2 m/s wind @ 315° - stable condition

Figure 13.Plume behavior in the along valley simulated wind field - unstable
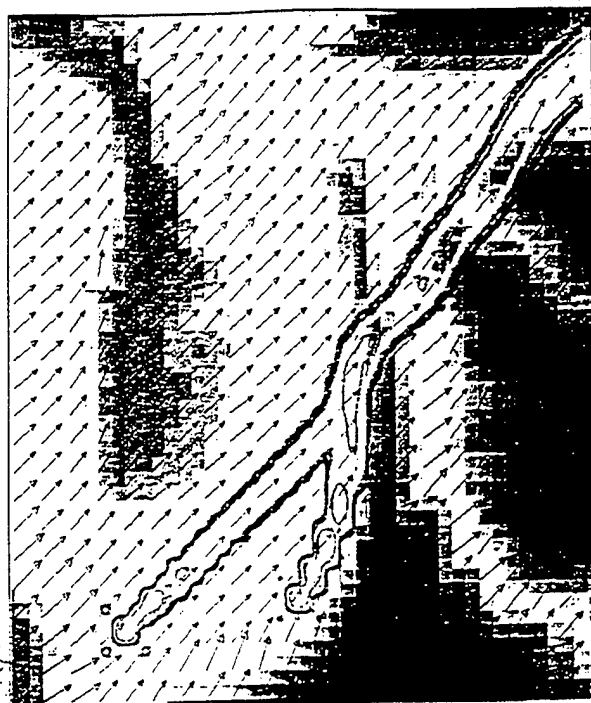
Figure 14. Plume behavior in the along valley simulated wind field - stable

Figure 15.Plume behavior in the cross valley simulated wind field - unstable

Figure 16.Plume behavior in the cross valley simulated wind field - stable

10

Aerosol Characterization Methods-Aerosol Samplers and Collectors

THIS PAGE INTENTIONALLY LEFT BLANK

Title: Absolute Reference Sampler

Authors: Robert W. Doherty, Paul J. DeLuca, Daryl W. Jones,
          Daniel J. Weber, Daniel G. Wise at CBDCOM and Edwin Parry
          at NSWC, Dahlgren, VA

Abstract: Most outdoor aerosol samplers operate at a fixed volumetric
flow without regard to ambient wind speed or direction. For wind speeds
in excess of a few mph, such sampling will result in over or under
sampling of aerosol particles larger than a few microns in aerodynamic
diameter. An aerosol sampling inlet which points into the wind and
pulls at that volumetric flow which establishes an inlet air stream
speed equal to the ambient wind speed has been built and is currently
being evaluated.

Report: In order to minimize aerosol sampling bias when sampling from
the environment, it is necessary to meet both the iso-axial and the iso-
kinetic sampling criterion. The iso-axial condition is met when the
axis of the sampler inlet is pointing into the direction of the ambient
wind. The iso-kinetic condition is met when the sampler's inlet air
stream speed equals the ambient wind speed. Both of these conditions
have been achieved in the Absolute Reference Sampler (ARS) recently
developed at the Aerosol Science and Technology laboratory, CBDCOM.
Figure 1 shows a schematic of the sampler head and flow train for the
ARS
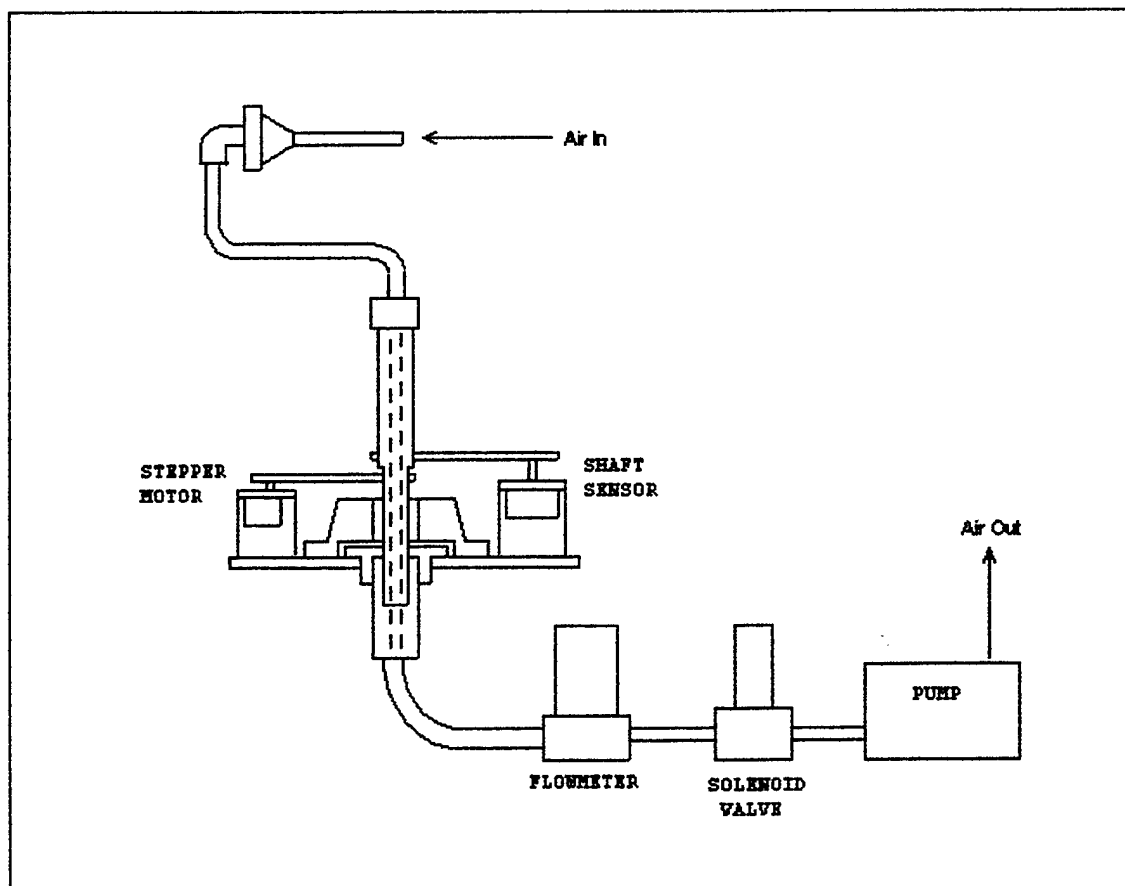
Figure 1: Air Flow Diagram for Iso-Kinetic Reference Sampler

13

Data from a meteorological (met) station provides the direction of
the wind referenced to a northerly wind of 0 degrees. A position sensor
reads the present position of a rotating shaft which supports the
aerosol inlet and through which the volumetric flow is drawn. A
comparator circuit, schematically shown in Figure 2, compares the
current position (angle) of the sampler inlet with the met station's
current wind direction signal. If the signals are equal,
no change in the location of the sampler inlet is taken. If the signals
are unequal, a stepper motor rotates the shaft in the appropriate
direction until an equality in signal magnitudes is achieved. This
establishes the iso-axial condition.
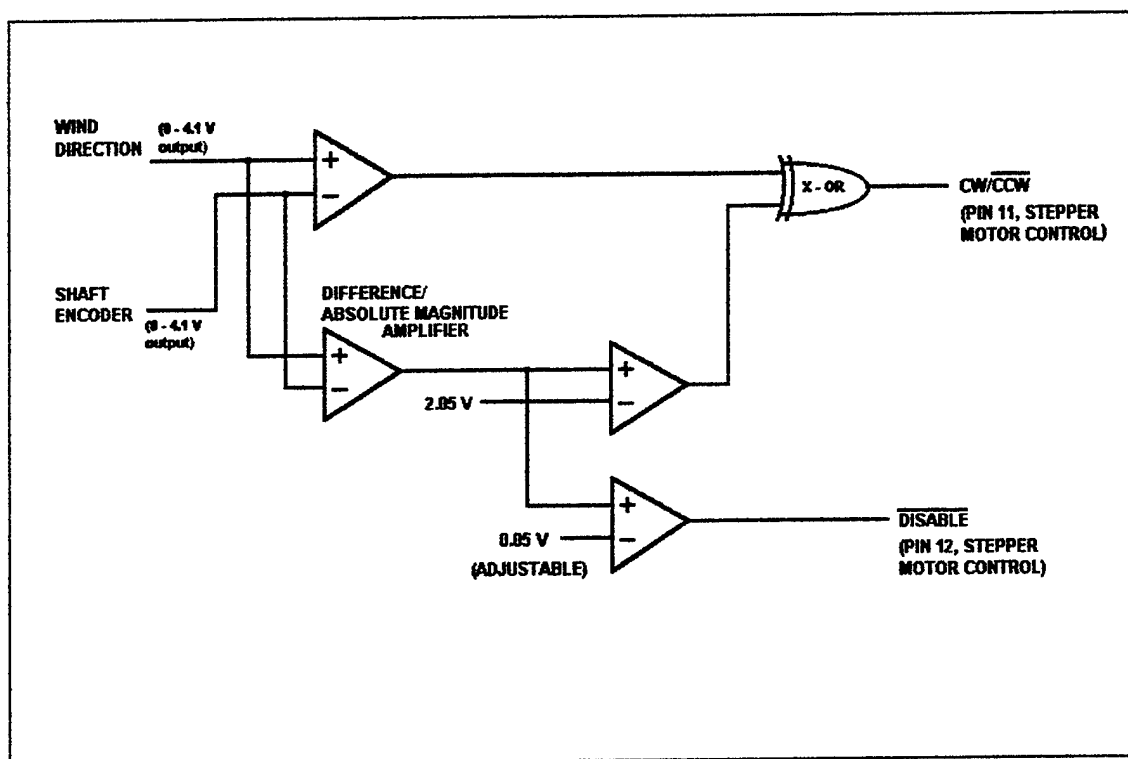
**Figure 2: Schematic overview of stepper motor control circuit for positioning of sampler head into
wind direction**

The met station also provides wind speed data as a square wave whose
frequency is linearly proportional to the wind speed. Figure 3
illustrates the use of a frequency to voltage converter, to provide an
output voltage proportional to the met station's ambient wind speed.
This output voltage is compared with the output voltage from the mass
flow meter of Figure 3. If the signals are equal, no adjustment is made
on the proportional solenoid valve. An inequality in these signals
produces a change in the voltage being applied to the proportional
solenoid valve which connects a fixed vacuum source to the sampler. The
proportioning valve input is pre-scaled in accordance with the ARS inlet
cross-sectional area such that equality of input signals at the
comparator of Figure 3, corresponds to equality between ambient wind
speed and inlet air stream speed. This enables the ARS to meet the iso-
kinetic sampling criterion.

14

Figure 3: Schematic overview of flow control circuit

Figure 4 shows a comparison of met station devised wind direction against the ARS's inlet axial position measurement. Data was taken in an open air test range at Dugway Proving Ground during the May/Jun 98 field trials. The data shows good agreement between the met station wind direction and the self-adjusted direction of the ARS inlet.

Figure 4: Data from Dugway field trials demonstrating sampler head position vs. wind direction over a 2.5 minute period

Figure 5 compares the met station wind speed measurement with the ARS adjusted inlet air stream speed. Again the agreement is quite favorable.

Figure 5: Data from Dugway field trials demonstrating sampler flow rate vs. wind speed (flow rate has been normalized to wind speed by multiplying by a factor of 3.4)

The overall dynamic range of the presently configured ARS is 1 to 10 mph. Below 1 mph, the cupped vane anemometer of the present met station is u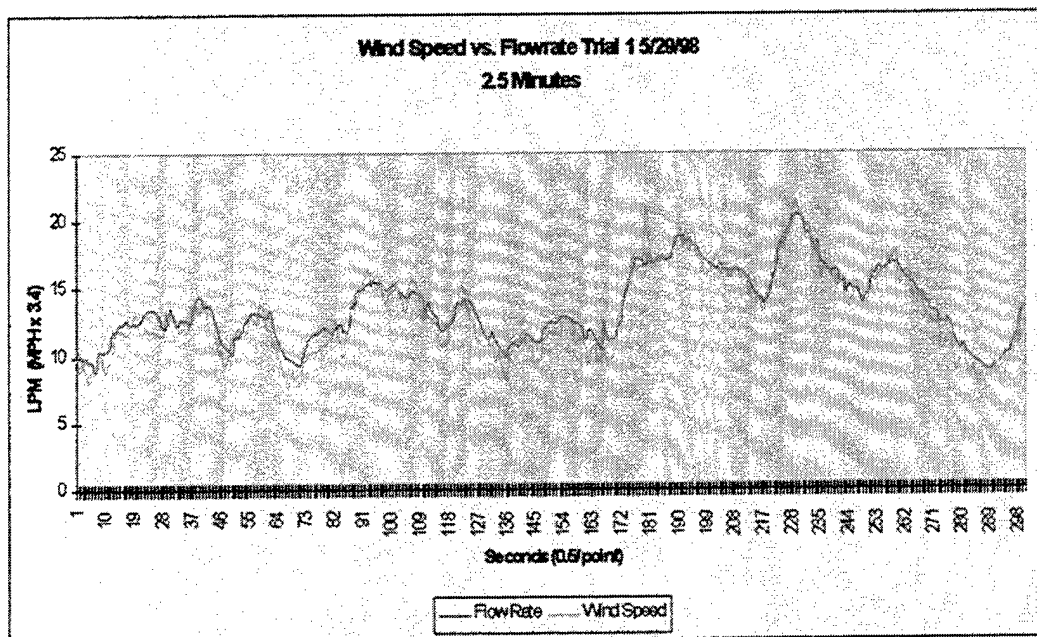nreliable due to frictional problems in the rotational bearings. A little above 10 mph the proportioning valve is wide open such that no further flow control of the vacuum level is possible. The ARS has been tested both with membrane filters having a pore size of 1 micrometer and HEPA quality glass fiber filters. Pressure drop across the membrane filters is much greater than across the glass fiber filter, but the mass flow meter reading is independent of the pressure drop such that either filter media can be used up to the 10 mph current limit. The limiting factor to sampling from higher wind speeds remains the small passage ways through the present electrical proportioning valve.

Wind tunnel testing of the ARS is in progress. As expected, the ARS has shown itself to adjust to changes in wind tunnel speed while maintaining a fixed orientation to the sampler inlet (pointing upstream). Preliminary comparative testing of the ARS against a fixed reference filter using 2 micrometer fluorescing polystyrene latex spheres in the wind tunnel at 7 mph has brought to our awareness a non-uniformity to the spacial homogeneity of the aerosol in the tunnel test section. Correcting for this inconsistency, yields fair agreement at 80%. Further work on the wind tunnel to produce larger monodisperse aerosols up to 20 micrometers aerodynamic equivalency, and greater homogeneity in aerosol concentration both spatially and temporally is needed to further test the ARS.

16

Figures 6, 7 and 8 show respectively the ARS system, the wind tunnel test facility, and the insertion sleeve with 36 jet nebulizer for the fluorescing polystyrene latex spheres.
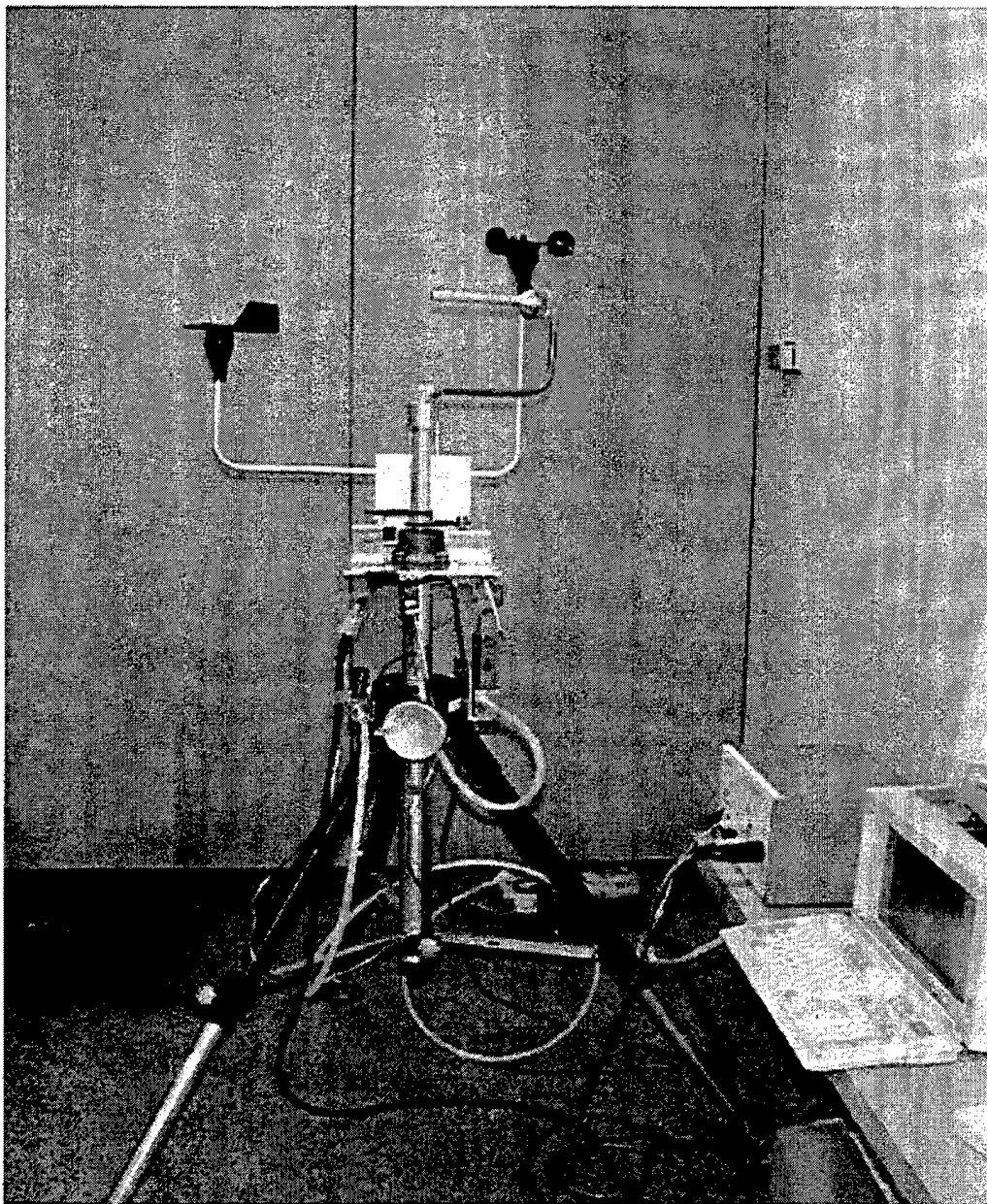
Figure 6: The Absolute Reference Sampler mounted on a tripod.

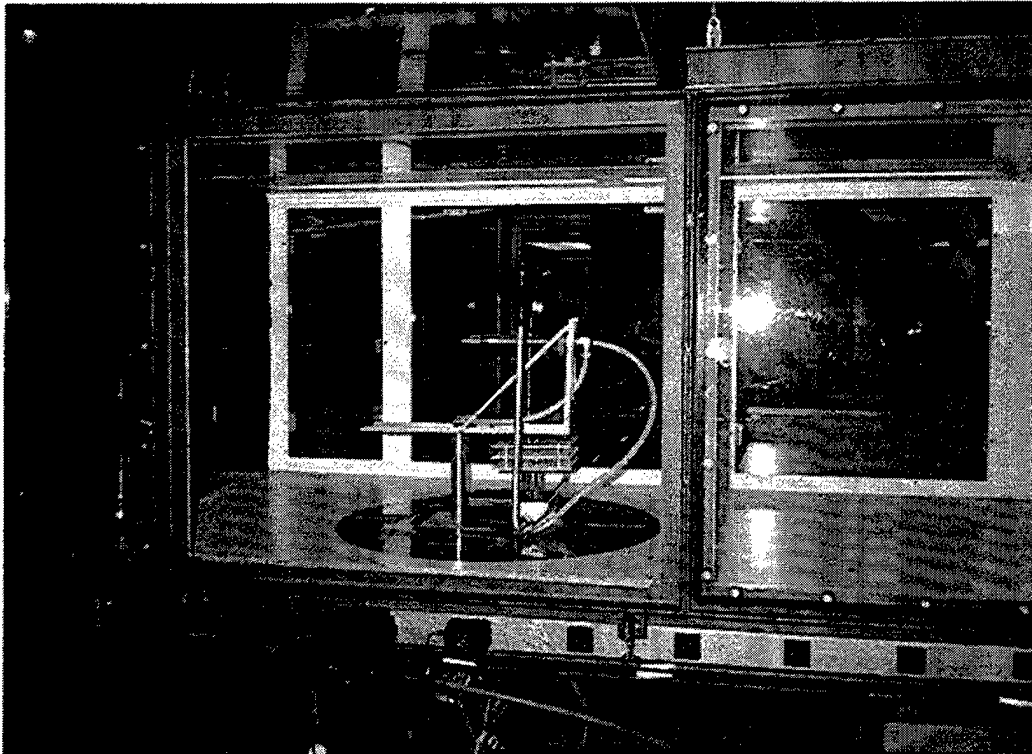Figure 7: Sampler in wind tunnel during testing.
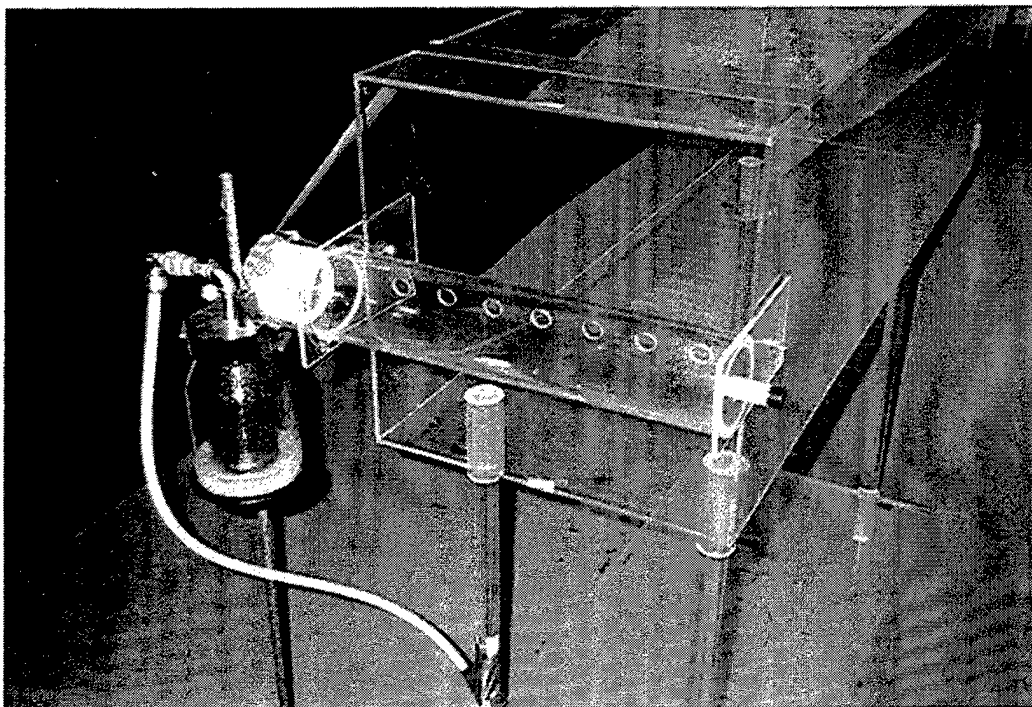
Figure 8: Nebulizer used to produce even particle distribution throughout containment sleeve inside wind tunnel

Figure 9 shows the ARS system at the Dugway Proving Ground test sight.
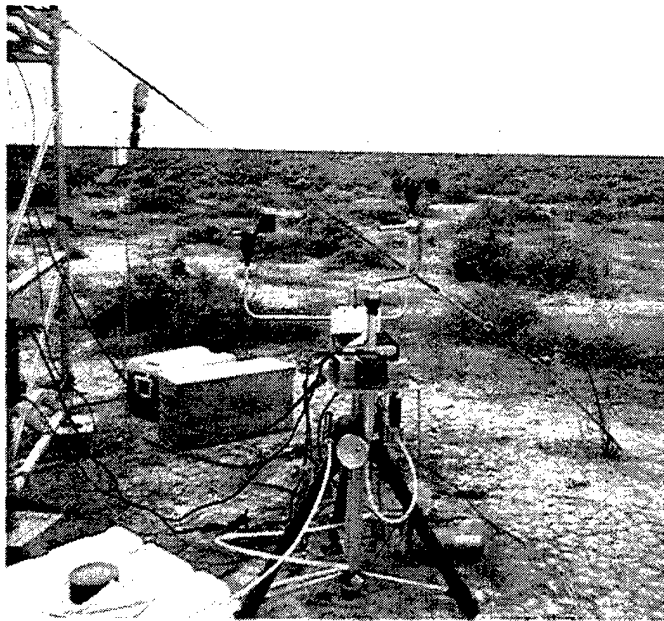
Figure 9: Reference Sampler during Dugway field trials.

Figure 10 shows the flat velocity profile obtained at the exit of the test sleeve.

Figure 10

19
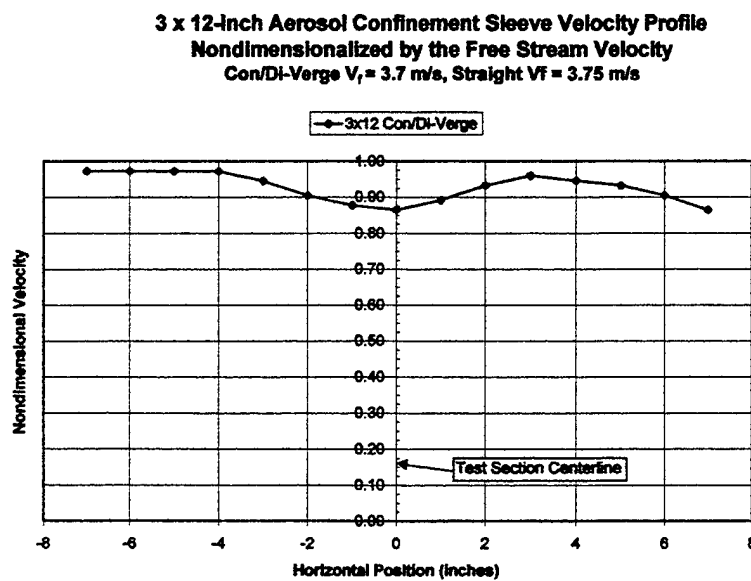
Figure 11 shows the spacial non-uniformity for the 2 micrometer fluorescing polystyrene latex spheres as measured by an Aerodynamic Particle Sizer (APS) at the exit of the test sleeve.

3 x 12-inch Aerosol Confinement Sleeve Consentration Profile
Nondimensionalized to the Centerline Concentration
Concentration (dN/dlog Dp) along centerline = 47.5
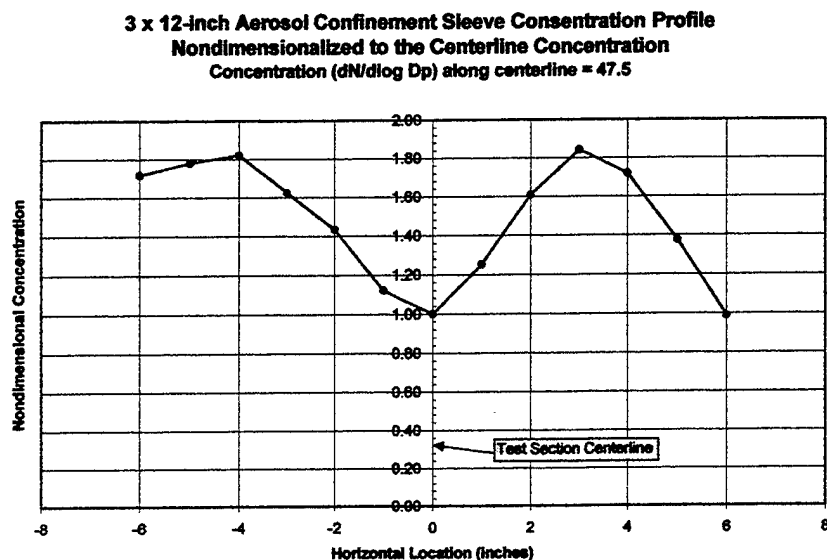
Figure 11

Summary:

        The Absolute Reference Sampler (ARS) has been demonstrated to meet both the iso-axial and iso-kinetic ambient aerosol sampling criterion both in wind tunnel and field experiments. However, in order to fully prove the ARS' advantage over fixed sampling systems, refinement in the present techniques for generating monodispersed, large particle aerosols in our wind tunnel facilities are necessary.

        The present ARS is designed as an absolute aerosol mass monitoring device. This should be readily expandable to providing an aerosol mass concentration device by incorporation of a low cost aerosol particle counter to deconvolve cloud arrival and intensity versus time, and cloud departure. Ultimately a second iso-kinetic stage will be added with a varying cross-sectional inlet area to interface the ARS to such fixed volumetric devices as aerosol particle counters, viable cascade impactors, slit to agar impactors, and all glass impinges (AGI).

WETTED WALL CYCLONES FOR SAMPLING BIOAEROSOLS

ANDREW R. MCFARLAND
DEPARTMENT OF MECHANICAL ENGINEERING
TEXAS A&M UNIVERSITY
COLLEGE STATION, TX 77843
e-mail: arm9136@acs.tamu.edu

H. WES DAVIS
ANDERSEN INSTRUMENTS INC.
500 TECHNOLOGY COURT
SMYRNA, GA 30082

ABSTRACT

Two wetted wall cyclonic biological aerosol sampling systems were designed, fabricated and tested. The first system utilizes an Andersen Instruments Model 1200 PM-10 Inlet followed by a Porton Downs Glass Cyclone, where the cyclone is fitted with an upstream water spray for washing the cyclone wall. Sampling flow rate is 990 L/min and is controlled by a critical flow venturi. The cyclone has a cutpoint of 1 μm aerodynamic diameter.

The second system has a shrouded probe inlet that samples at a flow rate of 1060 L/min, followed by a virtual impactor with a cutpoint of 1 μm that inertially concentrates the large particles into a flow rate of 57 L/min. The large particle flow stream is drawn through a transpirated-wall cyclone that has a cutpoint of 1 μm and the small particle flow (1003 L/min) is drawn through a critical flow venturi and discharged from the system. Liquid flow, which contains the large-particle fraction, is aspirated from the cyclone with a peristaltic pump.

TECHNICAL DISCUSSION

We developed two prototype biological samplers that use cyclones for the collection of biological aerosols and operate at sampling flow rates of approximately 1000 L/min. With reference to Figures 1 and 2, the two systems, which are designated as Models 1 and 2, can be seen to differ considerably in design. The entire sampled flow stream is drawn through the cyclone in Model 1, whereas an aerosol enrichment device (virtual impactor) is used in Model 2 so that only 57 L/min of aerosol is drawn into the cyclone.

Description of Model 1 System.

The Model 1 biological aerosol sampling system, Figure 1, draws air through an Andersen Model 1200 inlet at a flow rate of 990 L/min (35 cfm) and passes the air through a glass cyclone where aerosol particles with sufficient inertia are deposited. Water mist is introduced into the airflow upstream of the cyclone, the droplets are entrained by the flow, and they are subsequently deposited on the internal wall of the cyclone. Under ideal conditions, the deposited water droplets would coalesce in the cyclone to form a uniform film that would wash the biological particles from the collection surface to the base of the cyclone, where the liquid would be aspirated by a peristaltic pump. By careful control of the liquid flow rate to compensate for evaporation in the cyclone, an effluent flow rate of about 10 mL/min can be achieved.

Description of Model 2 System.

The Model 2 system that we fabricated and tested is shown schematically in Figure 2, where it may be noted that aerosol fractionation occurs in two stages. The sampled air stream first enters a 1 μm AD virtual impactor (MSP Corp., Minneapolis, MN), where a significant degree of aerosol concentration takes place. A flow rate of 1060 L/min (37 cfm) enters the virtual impactor and two flow streams leave the device: the first at a flow rate of 1003 L/min, which contains only aerosol particles with sizes ≤ 1μm aerodynamic diameter (AD); and, the second at a flow rate of 57 L/min, which contains particles with sizes > 1 μm AD and 2/37 of the aerosol particles with

sizes ≤ 1 μm AD. The small particle air stream (1003 L/min) is discharged from the system and the 57 L/min flow rate is air stream drawn through a cyclone with a cutpoint of about 1 μm AD, where cutpoint is defined as the particle size for which the collection efficiency is 50%. The cyclone has a porous wall so liquid can be transpirated through it. Aerosol particles collected in the cyclone are aspirated as a hydrosol at a liquid flow rate of about 1 mL/min.

LABORATORY TESTING OF THE SAMPLING SYSTEMS

Test Protocol and Results for the Model 1 System.

The Model 1 system was tested in the laboratory using the arrangement shown in Figure 3. Aerosol, generated with a vibrating jet atomizer (Berglund and Liu, 1973), was introduced into the body of the Andersen Model 1200 Inlet. The aerosol was formed from a mixture of alcohol, oleic acid and sodium fluorescein, which following evaporation of the alcohol, produced monodisperse liquid droplets of oleic acid tagged sodium fluorescein (about 10% m/v). Aerosol size was measured by collecting samples on glass slides treated with an oil-phobic agent and examining the slides under a microscope. The gravitationally-caused flattening of droplets on glass slides was compensated by the factor of Olan-Figueroa et al. (1982). The microscopically determined particle sizes were converted to aerodynamic size using an approach such as that given by Wong et al. (1996).

During a test, the aerosol was first collected on a filter placed in the filter holder at the base of the Andersen Model 1200 Inlet. Next, the filter at the base of the inlet was removed and the aerosol was allowed to flow through the system to be collected by the cyclone. The filter was placed in a mixture of water and alcohol to elute the tracer and the inside wall of the cyclone was washed with a mixture of water and alcohol to extract the tracer, then the two solutions were analyzed fluorimetrically. For each particle size, at least three replicate tests were conducted. A

filter at the exit of the cyclone was used on occasion for a mass balance; however the results given herein are based on use of the upstream filter and the wash from the cyclone wall.

The performance parameter of interest is the total aerosol collection, where total collection is defined as the ratio of the aerosol concentration based on the particulate matter collected by the cyclone to aerosol concentration based on particulate matter collected at the sampler inlet.

With reference to Figure 4, a plot is given of the performance of the Model 1 system, where the total collection by the cyclone is shown as a function of aerodynamic particle diameter. The curve shows an increase in efficiency for particle sizes from 0.8 to 9.2 μm AD, then a decrease in collection efficiency for sizes larger than about 10 μm AD. The increasing part of the curve is due to the cyclone fractionation characteristics, where larger particles have higher inertia and are therefore more efficiently collected (Moore and McFarland, 1993 and 1996). This cyclone has a cutpoint of 0.8 μm AD and collects 2 μm AD aerosol particles with an efficiency of 85%. For sizes larger than 10 μm AD, the internal losses in the flow system become so significant that the overall collection efficiency is degraded; indeed, the collection efficiency of the cyclone is reduced to about 50% at a particle size of 20 μm AD. These losses occur in the 90° bend that is located below the inlet, in the tubing and contraction connecting the bend with the cyclone, and in the cyclone inlet itself.

Test Protocol and Results for the Model 2 System.

The Model 2 cyclone was tested using two setups, which are combined in the schematic diagram shown in Figure 5. For the first test setup, aerosol generated with a Berglund-Liu vibrating jet atomizer was introduced directly into the sampler inlet. With this setup, only the virtual impactor was evaluated, and that was done by alternately sampling the total aerosol concentration in the chamber that contains the virtual impactor and the aerosol concentration of the large particle flow stream at the exit of the virtual impactor. This approach allowed the

24

penetration of the large particle fraction of the virtual impactor to be characterized. At least triplicate tests were conducted for each particle size. Next, with the virtual impactor removed from the system, the cyclone was tested separately, where aerosol was alternately sampled upstream and downstream of the cyclone (see Figure 5). Again, at least three tests were conducted for each particle size. In addition, aerosol penetration through the 90° bend of the transport line between the virtual impactor and the cyclone was calculated through use of DEPOSITION software (Riehl et al., 1996). The efficiency of the cyclone, the penetration through the virtual impactor, and the penetration through the bend were combined to provide a total collection efficiency for the system (fraction of total aerosol collected by the cyclone).

With reference to Figure 6, the total collection efficiency of the Model 2 system is shown as a function of particle size. The cutpoint of the cyclone (not shown) is about 1 μm AD; however, the virtual impactor also has a cutpoint of 1 μm AD, so the particle size associated with an overall or total collection efficiency of 50% is about 1.5 μm AD. The combination of losses and the fractional efficiency of the virtual impactor limit the maximum total efficiency to 92%, which occurs at a particle size of 2.8 μm AD. For larger particle sizes, the total efficiency is reduced due to wall losses on internal surfaces of the virtual impactor and wall losses in the bend.

CONCLUSIONS AND RECOMMENDATIONS

Two cyclonic biological aerosol samplers were designed, fabricated and tested with non-viable aerosols. Each of these units has certain advantages; in particular, the Model 1 system accommodates collection of a broader range of aerosol sizes due to the lack of a virtual impactor and larger dimensions in the aerosol transport system. This system has the potential to be an excellent aerosol sampler; however there are several design changes that should be made before it could be considered for general field use. In particular, changes should be made to:

1) Obtain a uniform liquid film on the walls of the cyclone. For the Model 2 unit, we have developed a transpirated wall cyclone, where liquid is forced through the porous inner wall of the cyclone. This approach assures a uniform film on the cyclone wall and perhaps the concept could be incorporated into a cyclone with dimensions similar to those of the Model 1 unit.

2) Heat the system to prevent freezing of the liquid in cold conditions. As the Model 1 currently exists, it is not realistic to heat the air stream to prevent freezing. However, if a transpirated wall cyclone were used, only the cyclone, the liquid flow sub-systems, and an enclosure need to be heated.

3) Reduce the size of the inlet. The Model 1 utilizes a commercially available PM-10 inlet, which has a characteristic dimension of about 600 mm (2 ft). The entire system could be made smaller and thus less readily identifiable in the field.

On the other hand, the Model 2, which has a transpirated wall cyclone, is more compatible with the goals of obtaining a uniform film of liquid over the collection surface and prevention of freezing during cold conditions. The Model 2 system has three inherent advantages over the Model 1 unit, namely:

1. The walls of the cyclone are uniformly wetted by the transpiration process.

2. The amount of liquid evaporation is smaller because the air flow rate in contact with the liquid is only 57 L/min.

3. The cyclone and the 57 L/min air flow could be heated to prevent freezing of the liquid. A heat input of about 50 W to the 57 L/min air flow line would provide the needed thermal protection.

However, there are also disadvantages to the existing design of the Model 2 system, in particular:

1. The virtual impactor is a commercially available unit that was designed for the collection of PM-10 aerosol, and loss of particles with sizes greater than 10 μm was not of concern in that application. When we tested the Model 2 with 8.4 μm AD

26

particles, the losses in the virtual impactor were 21%; and, the losses were higher for larger particles

2. Currently we use a pump for the 57 L/min flow rate and a blower for the 1000 L/min flow. A single blower could be used for both flows and critical flow venturis could be used to control the flow in each line.

REFERENCES

Berglund, R.N. ; Liu, B.Y.H. (1973). Generation of monodisperse aerosol standards. *Env. Sci. Technol.* 7:147-153.

Moore, M.E.; McFarland, A.R. (1993). Performance modeling of single inlet aerosol sampling cyclones. *Environ. Sci. & Technol.* 27: 1842-1848.

Moore, M.E.; McFarland, A.R. (1996). Design methodology for multiple inlet cyclones. *Environ. Sci. & Technol.* 30: 271-276.

Olan-Figueroa, E.; McFarland A.R.; Ortiz, C.A. (1982). Flattening coefficients for DOP and oleic acid droplets deposited on treated glass slides. *Am. Ind. Hyg. Assoc. J.* 43:395-399.

Riehl, J.R., Dileep, V.R., Anand, N.K., McFarland, A.R. (1996). DEPOSITION 4.0: An illustrated user's guide. Aerosol Technology Laboratory, Texas A&M University, College Station, TX.

Wong, F.S.; McFarland, A.R.; Anand, N.K. (1996). An experimental study of aerosol penetration through horizontal tubes and Strom-type loops. *Health Physics* 71: 886-891.
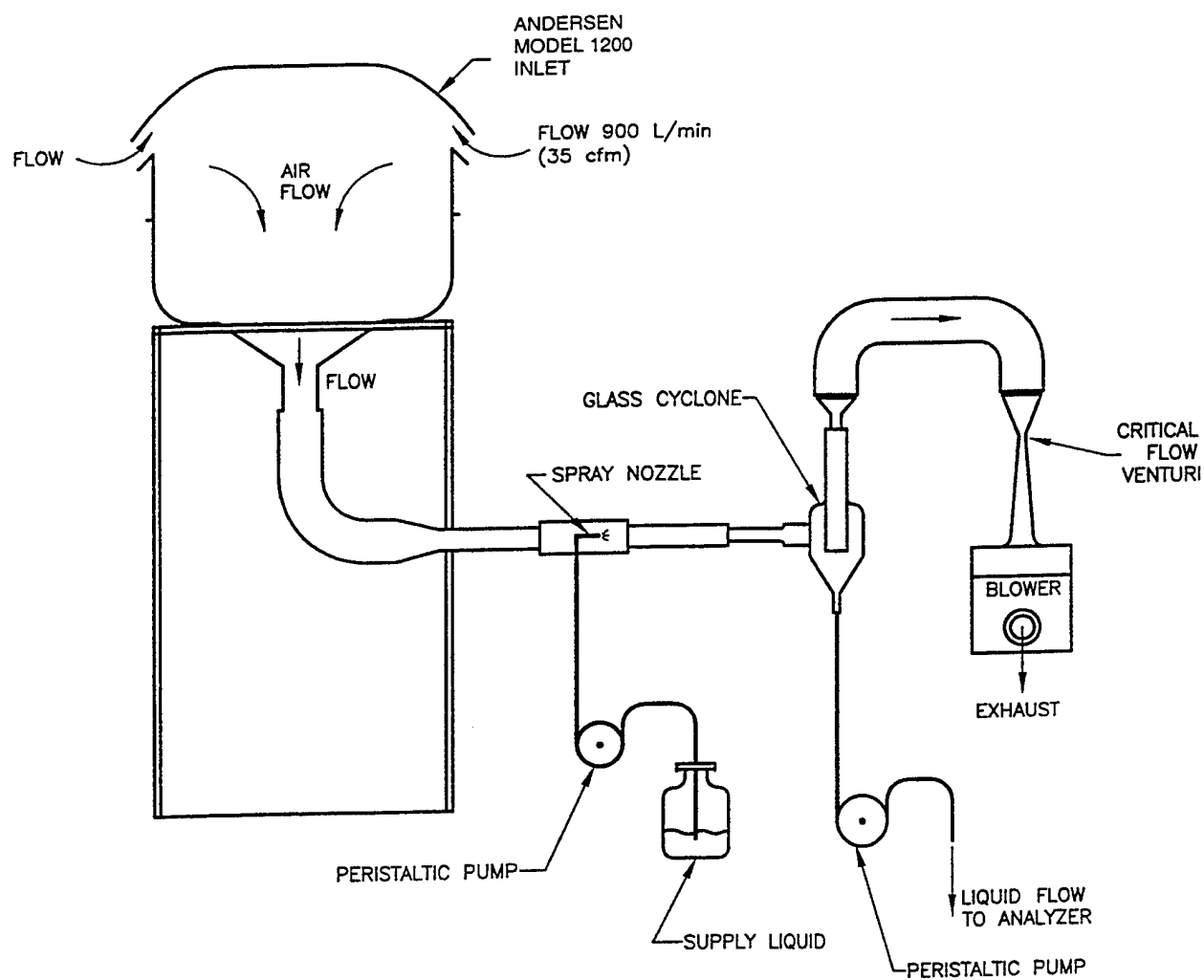
Figure 1. Model 1 biological aerosol sampling system. A glass cyclone is used for aerosol particle collection, and the cyclone is irrigated by a upstream spray of liquid.
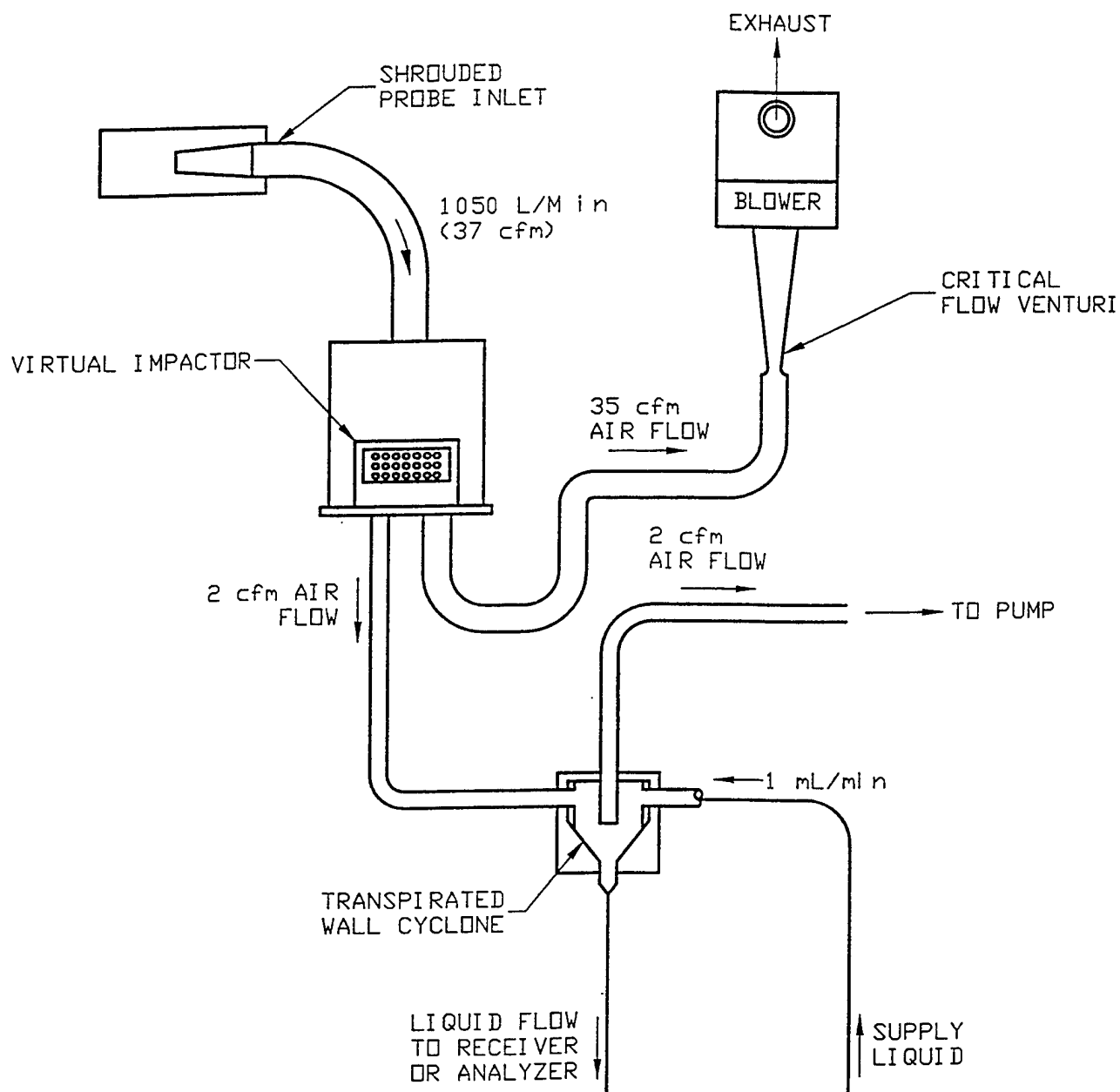
Figure 2. Model 2 biological aerosol sampling system. A virtual impactor is used to concentrate the particulate matter of interest into a flow rate of 57 L/min before the aerosol particles of interest are collected by a transpirated-wall cyclone.

29
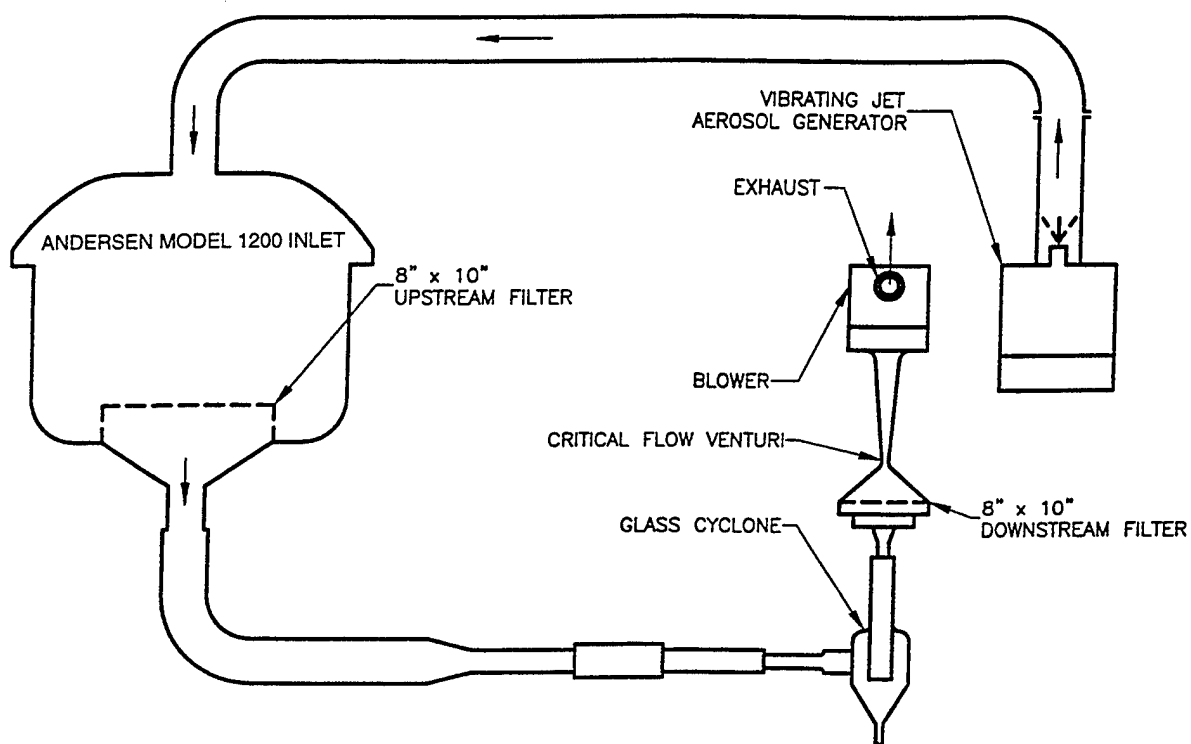
Figure 3. Setup used to test the Model 1 biological aerosol sampler.
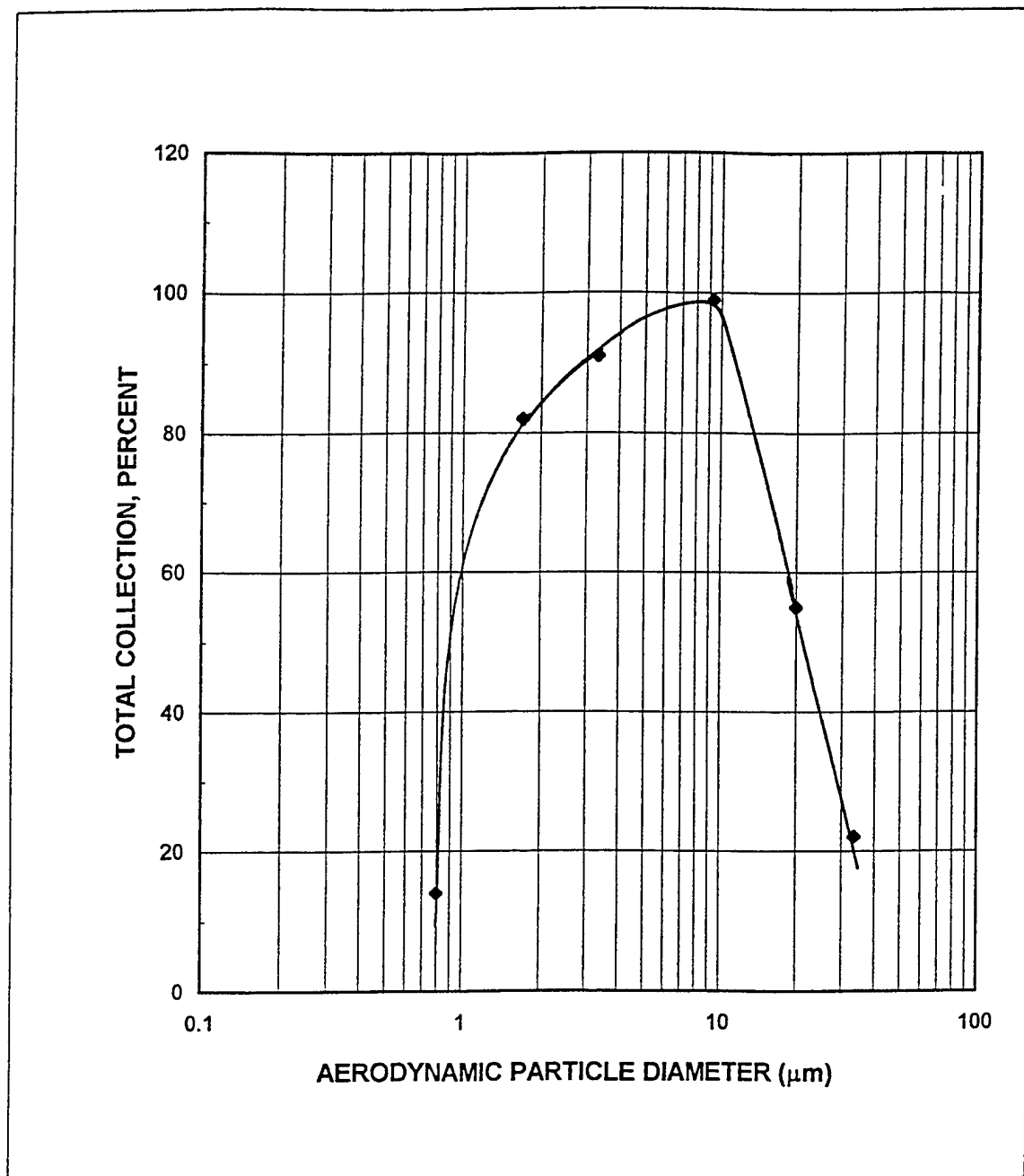
Figure 4. Total collection of aerosol particles by the cyclone of the Model 1 system.
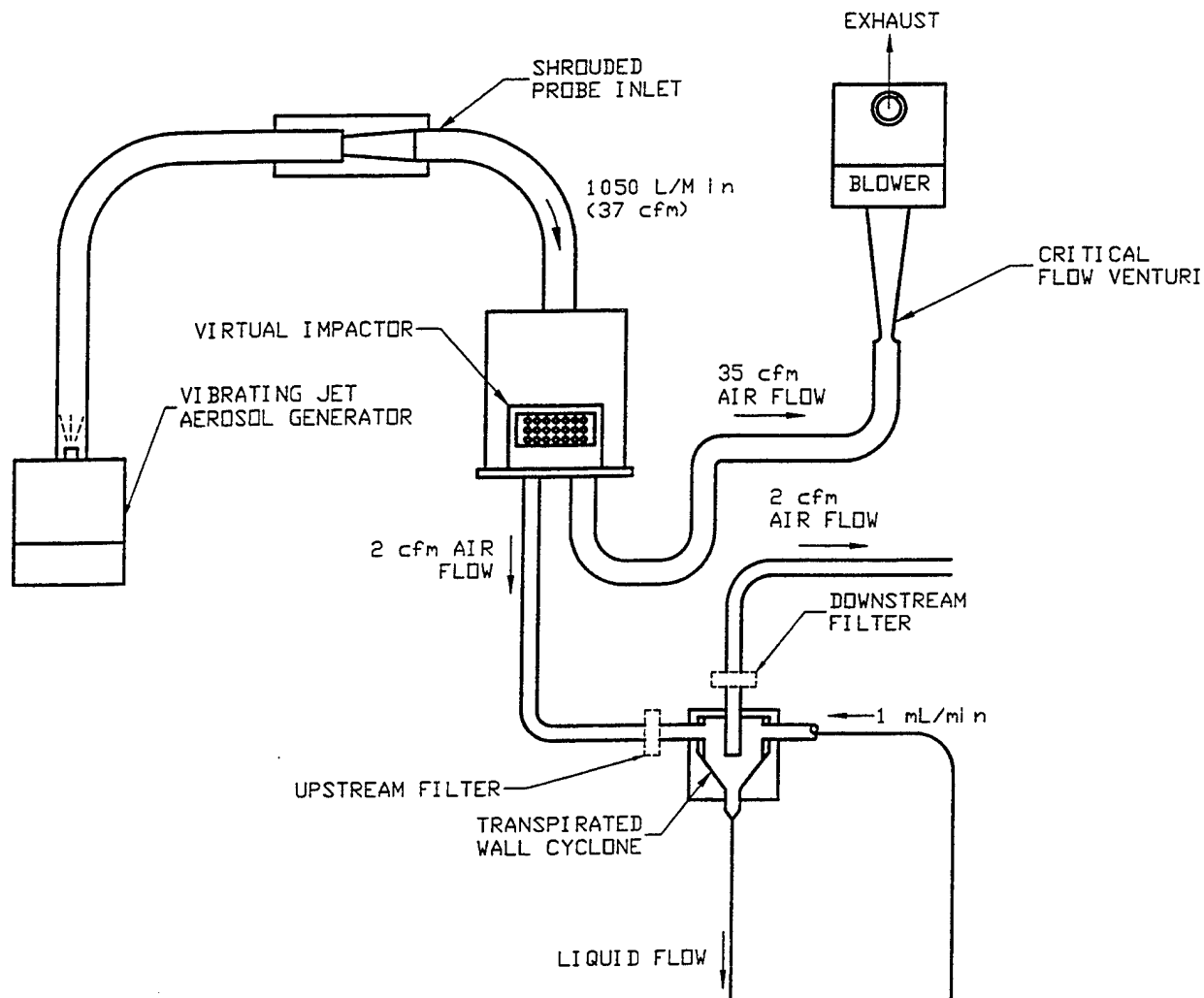
Figure 5. Setup used to test the Model 2 biological aerosol sampler.
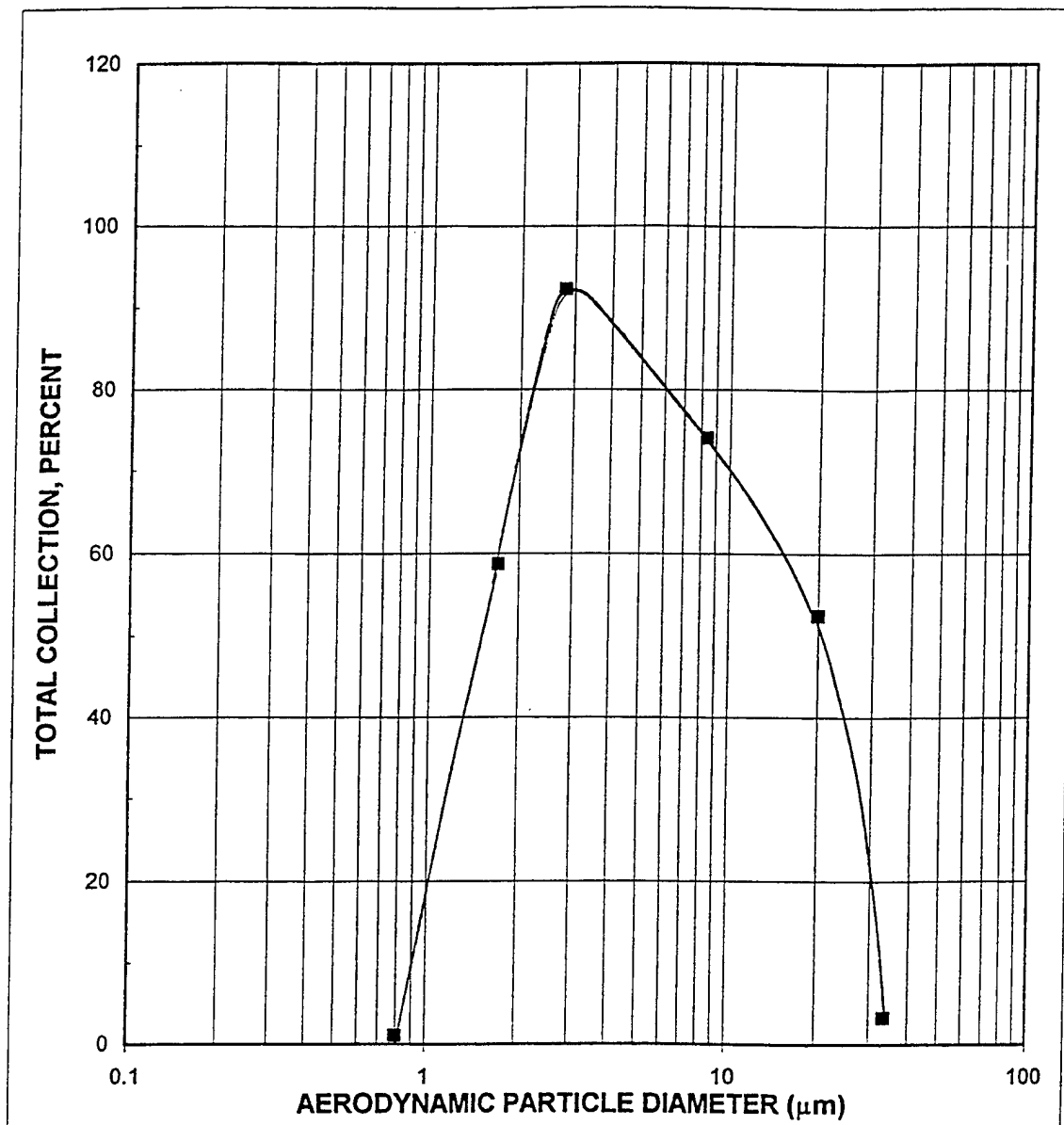
Figure 6. Total collection of aerosol particles by the Model 2 system.

THIS PAGE INTENTIONALLY LEFT BLANK

MICRO-MACHINED VIRTUAL IMPACTOR ARRAYS FOR THE COLLECTION OF AIRBORNE BACTERIA

Vanessa M. Kenning, Charles J. Call, Patrick T. Call, and Joseph G. Birmingham

MesoSystems Technology, Inc.
3200 George Washington Way
Richland, Washington 99352
Ph: 509-375-1111   FAX: 509-375-0115
Email: VKenning@MesoSystems.com

RECENT PUBLICATIONS, SUBMITTALS FOR PUBLICATION, AND PRESENTATIONS:

ABSTRACT

Collection of airborne bacteria (bioaerosols) is of interest for a variety of public health and national security concerns. A novel microfabricated virtual impactor device is being developed to concentrate bioaerosol particles in the 1 - 10 micron size range, which is typical of bacterial spores. The concentration is from a large to a small volume of air, with target concentration factors between 5 and 50. A virtual impactor uses the particle's inertia to separate it from the main flow stream. Our design approach represents a significant departure from existing virtual impactor technology: the particle laden flow is directed into planar rows of virtual impactor elements. This novel architecture is described in detail in this paper. The utilization of computational fluid dynamics has led to designs in which each impactor row is specialized. Polystyrene latex (PSL) spheres are used in experiments to simulate the bioaerosol particulates. The experimental results presented show trends that do not correlate with the simulations. The data support our hypothesis that surface roughness may result in turbulent mixing within the virtual impactor elements, thereby reducing the effectiveness of the concentrator. Additional study of the effect of surface roughness and turbulence within the virtual impactor is planned.

INTRODUCTION

The collection and measurement of bioaerosols are of interest to a wide community of public health and national security officials because they can cause infectious diseases or chemical damage to the respiratory system. Bioaerosols are defined as airborne particles, large molecules or volatile

35

compounds that are living, contain living organisms or were released from living organisms. The size of a bioaerosol particle may vary from 0.01 micron to 100 microns. The behavior of bioaerosols is governed by the principles of gravitation, electromagnetism, turbulence and diffusion.

The technology for an effective aerosol collection system for airborne biological material is a vital national concern to protect against:

- airborne pathogenic agents released by terrorist groups;
- biological warfare agents used in military applications;
- infectious organisms contaminating air in hospitals, research labs, public buildings, and confined spaces such as subway systems and commercial aircraft; and
- pollutant aerosols that damage the respiratory system.

Since pathogenic bioaerosols are usually present in low concentrations in the environment, systems used to determine the presence of various pathogens are more effective in terms of speed and accuracy when the aerosol has been pre-concentrated. Our objective is to develop aerosol collectors to concentrate particles of biological origin from hundreds of liters of air into a sample of several milliliters of water or into a concentrated air stream of approximately 10 liters per minute. This paper is an initial reporting of air-to-air concentration measurements and simulations based on a novel design approach for virtual impactors.

NOMENCLATURE

CF	Concentration factor
V_o	Air velocity
S	Particle stopping distance
d_p	Particle diameter
ρ_p	Particle density

VIRTUAL IMPACTOR CONCEPT

The inertial impactor has played a significant role in the classification of aerosols according to their aerodynamic size. An impactor or virtual impactor uses a particle's inertia to remove it from the bulk airflow. The laminar jet impactor has been used extensively because it is simple in design and its performance is predictable. However, issues of particle bounce, particle rupture and impaction plate overloading must be accommodated (see, for example: Marple and Lui, 1974 and Marple and Willeke, 1976). To detect airborne bacteria cells and spores at low concentrations and in real time, a degree of pre-concentration of the bioaerosol is needed to improve the system's sensitivity, regardless of the type of bio-sensor employed. Thus, an air to air pre-concentrator is useful, and virtual impaction technology, first introduced by Hounam and Sherwood (1965) and Conner (1966), is one of the few approaches which can be readily applied. Within a virtual impactor, the intake air flows from a nozzle directly at a second opposed nozzle, from which only a small "minor flow" is allowed to exhaust. As a result of the inertia, most of the particulate greater than a particular cut size are caught in this slow minor flow and exit the virtual impactor. Most of the inlet air and particulate of a size smaller than the virtual impactor cut size is exhausted as the "major flow". Early two-stage virtual impactor devices were developed by Loo and Jaklevic (1974) and Loo et al. (1976) to meet the need described above- the sampling and concentration of aerosols

36

from large volumes of ambient or atmospheric air. Loo and Cork (1988) review
the development of high efficiency virtual impactors based on these
established concepts. Chen and Yeh (1988) presented techniques to minimize
internal losses, an issue of great importance to the overall effectiveness of
the aerosol concentrator.

The aerosol collection device which is described in this paper is a virtual
impactor array which concentrates airborne aerosol particles 1 micron and
larger from a large to a small volume of air. The basic principal for our
virtual impactor is similar to the more conventional devices described in the
aforementioned references. The air is forced around a series of structures,
all fabricated in the same plane, and the particles tend to follow the air
streamlines. The air and the smallest particles go around the structures but
due to their higher inertia, the larger particles are not able to make the
turns, cross the flow streamlines and are collected into the minor flow
channels. Our planar virtual impactor concept is illustrated schematically in
Fig. 1. Not shown in the schematic (to achieve a higher degree of clarity)
is the minor flow channel. This channel is formed by drilling a hole into
the center of the leading edge of the virtual impactor element. The hole is
drilled at a shallow angle such that the collected particles do not have a
sharp bend at the inlet to the minor flow channels.

Early work on micro-milled impactor arrays has previously been presented by
Birmingham, et al. (1997) and Call et al.(1998). The prefix *micro* (e.g.,
micromachined, microfluidics, etc.) is generally applied to devices which
have sub-millimeter features and/or flow passages. Non-conventional and
specialized quasi-conventional machining techniques are employed to create
these structures. In our case, miniaturized CNC milling has been
implemented. Other techniques, such as deep ultraviolet (or x-ray)
photolithography or deep reactive ion etching of silicon may be required in
the future to in order to realize our designs.
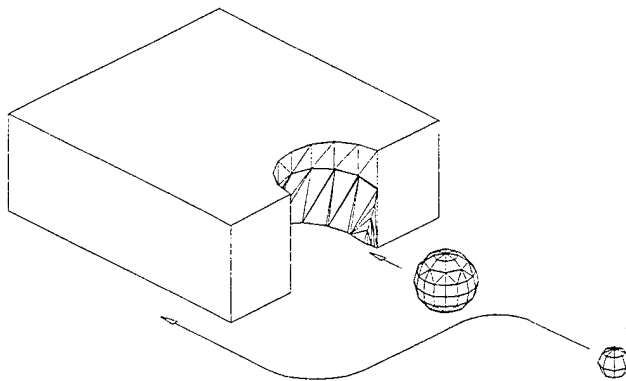
Figure 1. Illustration of impactor concept.

The structure depicted in Figure 1 is one in a planar array. Typically, the
array has three rows and twenty columns of these structures, with the middle
row offset by one-half of the structure width. Several of the impactor

geometries that have been studied to date are depicted in Figure 2. In the physical embodiments of these structures, each depiction is repeated laterally until each of the three rows has twenty columns of structures. These geometries have been analyzed by two-dimensional laminar flow CFD and the results are summarized in Figures 3 through 6 below.

COMPUTATIONAL FLUID DYNAMICS

Our present objective is to optimize the shape of the structure illustrated schematically in Fig. 1. The design of the impactor structure has modeled by computational fluid dynamics (CFD), and we are using the results to optimize the impactor geometry.
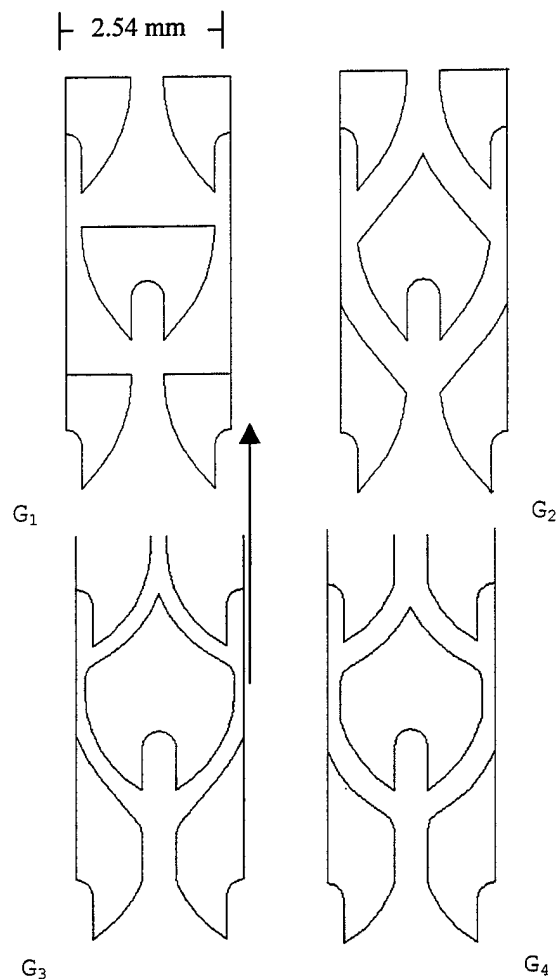
Figure 2. Geometries studied to date for the virtual impactor structures. Flow direction for each geometry is indicated by the arrow.

The desired qualities of the design are to be able to capture small particles (e.g., 1 micron) with at least 50% efficiency while attaining high flow rate and low pressure drop system-level functional design criteria. The computational fluid dynamics simulations were conducted using CFD-ACE

software developed by CFD Research Company. This software allows structured meshes and uses a Lagrangian method for tracking particles within the flow. Two-dimensional simulations were used for the results presented here. The boundary conditions provided for uniform inlet velocity and specified the volume flow rate through the structures. Advantage was taken of symmetry so that simulations were only performed on a small part of the total impactor array. Edge effects on the impactor array were neglected. This assumption was reasonable since the arrays tested experimentally had 20 elements per array, and thus, edge effects should account for 5% or less deviation. A more significant assumption regarding the modeling was that it was two-dimensional and non-turbulent. The characteristics of turbulence in microfluidic devices have not been studied extensively, and we have not attempted to incorporate turbulence models into the predictions. We note that this is an active area of research.

The evolution of designs G_1 through G_4 refer to changes in the shape and aspect ratio of the structure. The variation in the designs from a pressure drop and collection efficiency standpoint can be seen in Fig. 3. For each of the four geometries, the mass flux at the upstream boundary is determined by dividing an assumed flow rate by the height of the structures. The height is assumed to be 0.787 mm, consistent with the devices that have been fabricated, and the total flow was 0.5 liters per minute per column of structures. As the figure illustrates, the 1 and 2 micron particles were being captured more efficiently in most of the successive designs but with a significant increase in pressure drop across the device according to the CFD simulations. For each case, 90% of the flow exists as the major flow and the remaining 10% is distributed evenly between each of the three minor flows. Design G_4 combined a high efficiency with a lower pressure drop.

We have quantified the collection efficiency via the concentration factor that is defined as:

$$CF = \frac{\text{concentration of particles in minor flow}}{\text{concnetration of particles in inlet flow}}$$
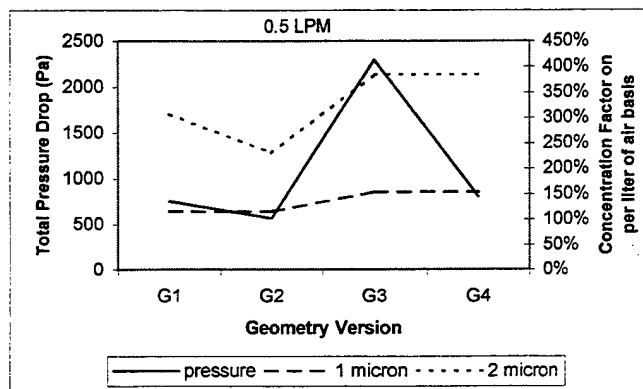

Figure 3. Concentration of 2 and 3 micron particles and total pressure drop for various designs modeled by CFD.

39

The predicted pressure drop for two of the designs is shown in Figure 4. Corresponding experimental measurements indicate that the predicted pressure drop is close to that obtained experimentally. Agreement is acceptable considering that the CFD simulations were two- dimensional and therefore do not include the effects of the top and bottom walls, which also contribute to the pressure drop. Also, the softwares turbulence models have not been used, forcing the simulation to remain laminar. Perfectly smooth walls are assumed for the simulation.
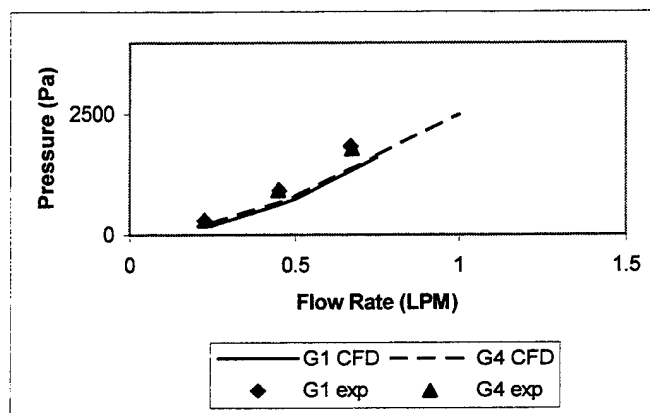
Figure 4. Pressure Drop from CFD with reference data points.

Pressure drop is an important system design parameter since it is envisioned that the aerosol sampler will be used in the field, and may require batteries as a power source.

Figure 5 shows the predicted concentration of various particle sizes for different designs, expressed as a percent concentration relative to the inlet flow. As the figure indicates, larger particles are much easier to collect than smaller particles. This is expected since the stopping distance of a particle is proportional to the diameter squared (Willeke and Baron):

$$S \propto V_o \rho_p d_p^2 \qquad (1)$$

Where V_o is the air velocity, ρ_p is the particle density and d_p is the particle aerodynamic diameter. Thus, a 3 micron particle has 9 times the stopping distance of a 1 micron particle of similar density. Figure 6 shows that, in general higher collection efficiency is predicted by the CFD with higher flow rate through a given device. In practice, however, it can be difficult to achieve these higher flow rates as they are also associated with higher pressure drop across the device. The optimum design is thus a compromise between high flow rates and minimum pressure drops. Higher flow rates would also bring turbulence effects which would tend to reduce collection efficiency.
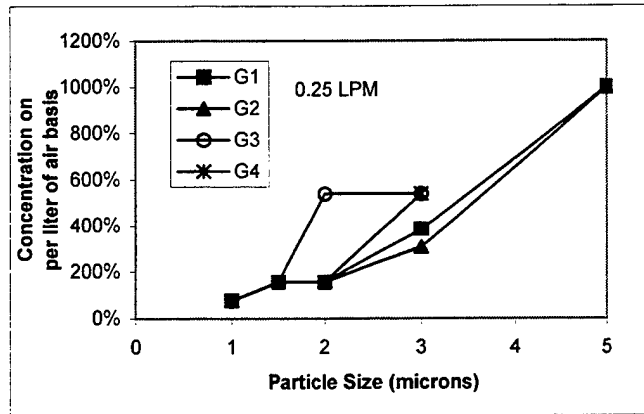
Figure 5. Concentration of a variety of particle
sizes predicted by CFD with different impactor designs.

WIND TUNNEL MEASURMENTS

A wind tunnel, seeded with polystyrene latex spheres (PSL), was used to
evaluate the virtual impactor structure plates. Each plate had 3 rows of
twenty structures. As observed in Figure 2, each of the rows are not
necessarily identical. The tests were conducted at a wind speed in the
tunnel of about 1 m/s with the virtual impactor device facing upwind. An
aerodynamic particle sizer (TSI model APS 3300) was used to normalize the
data. PSL spheres of nominally 1 and 2 microns in diameter were used for the
testing.

The flow coming into the device is divided into two outlet flows: a major
flow and a minor flow. The major flow comprises about 90% of the air flow
while the minor flow is designed to have 10% of the air flow and most of the
particle flow, thus concentrating particles from a large volume of air into a
small volume which can then be collected into a fluid or onto a solid surface
(e.g. filter paper or impaction plate) if desired. The data was collected
using the APS to alternately count particles at the inlet of the device and
at the minor flow outlet. The same tubing was used for both cases to
minimize the variation in particle count due to tubing losses. The count
rates for the inlet and minor flows were compared to obtain concentration
factor data shown in Figure 6.

Initial experimental results using 1 and 2 micron PSL particles are included
in Figure 6. The results of initial experimental testing do not show the
same trends as the CFD. Rather than increasing concentration with increasing
flow rate predicted by the CFD, a decrease is in concentration is seen. This
may be attributed to two factors: turbulence effects and wall losses.

Although the Reynolds numbers are less than 2000 for all the cases shown
here, recent work at Pacific Northwest National Lab (Shekkariz, 1998)
indicates that on these small scales, microscale turbulence can occur at
considerably lower Reynolds numbers. The mixing caused by turbulence would
tend to redistribute the particles resulting in a concentration factor of 1.0
neglecting wall losses. The CFD modeling did not account for turbulent
diffusion of particles because the Reynolds numbers were less than 2000 and

41

also because there are no validated models to simulate that behavior in devices of this class.

Wall losses may also increase with increased flow rate lowering the number of particles collected out both the major and minor air streams of the device. Visual inspection of the device after repeated PSL testing indicates that most of the particles lost on the walls are impacting on the walls of the minor flow channels indicating that the impactors are separating particles but losses are too high inside the device.

FUTURE WORK

An experimental plan will be developed to investigate the existence of turbulence, transition to turbulence and the extent of turbulent mixing within the virtual impactor structures.

Reduction of wall losses will likely involve investigation of other machining techniques to provide a smoother finish to the internal surfaces of the device. Coatings and other post-machining options will also be explored to prevent losses of particles in the device, and also to support a laminar flow. We recently identified burrs in the virtual impaction section of the device that are a result of the fabrication process. Burrs have the effect of filtering particulates as well as promoting turbulence. A new fabrication process has been identified that will solve this issue.

SUMMARY

The computational fluid dynamics simulations indicate that the effectiveness of the device in capturing particles (particularly those smaller than 3 microns) is strongly dependent on the shape of the impactor structures. The optimum design is one that minimizes pressure drop so that a high flow rate through the device is possible. This optimal design allows concentration of particles into an order of magnitude smaller volume of air.

Measured concentration factors are significantly lower than predicted by the simulations. Although the experimental data show some particle concentration into the minor flow, it is not as significant as that predicted by the CFD and does not follow the same general trends as the CFD predictions. We hypothesize that this is due to flaws in the fabrication process that result in turbulents mixing and reduced separation efficiency as well as wall losses within the device, and in particular within the minor flow tubes, due to particle impaction.
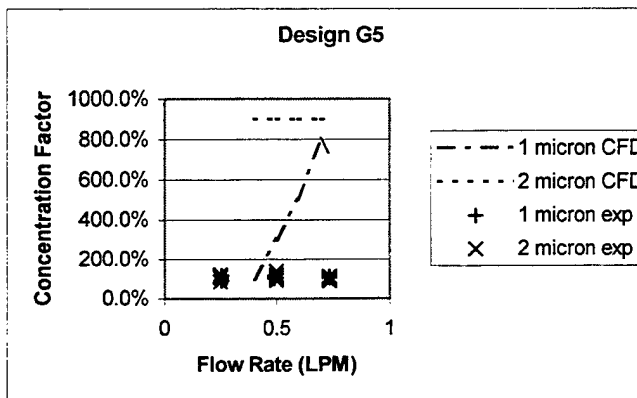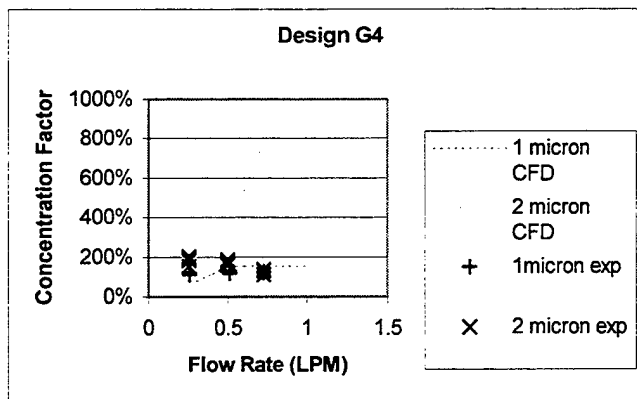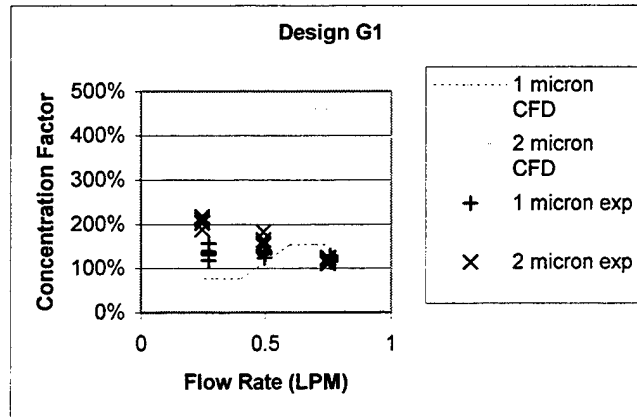
Figure 6. Comparison of CFD and experimental data for flow rate
dependence of concentration of particles for three designs.

REFERENCES

J.G. Birmingham, C.J. Call, D. Hammerstrom, Y.F. Su and Irving, P.M.; "Micro-machined Aerosol Collectors: Cyclone, Electrostatic Precipitator, and Virtual Impactor" presented at the 1997 Scientific Conference on Obscuration and Aerosol Research, Aberdeen Proving Ground, MD June, 1997.

P.M. Irving, J.G. Birmingham, and C.J. Call; "Use of Microtechnology in the Design and Fabrication of Lightweight, Low Power Aerosol Collectors" presented at the AAAR 1997 Annual Conference, Denver, CO, October 1997.

Willeke, K. and Baron, P.A. "Aerosol Measurement Principles Techniques and Applications" Van Nostrand Reinhold, 1993

ACKNOWLEDGEMENTS

Workshop: Preparing, Aerosolizing and Characterizing Erwinia herbicola

THIS PAGE INTENTIONALLY LEFT BLANK

ABSTRACT

Erwinia herbicola **: A Vegetative Bacterial Simulant.** Douglas R. Winters, Daniel D. Martin, Arthur K. Schwedler, and Bruce G. Harper. Division of Life Sciences, U.S. Army Dugway Proving Ground, Dugway, UT 84022.

Simulants are widely used in biological testing. Their use is advantageous from political, economic, and safety standpoints. Currently, there are four biological simulants which are routinely used for testing at U.S. Army Dugway Proving Ground (DPG). These are *Bacillus subtilis* var. *niger*, a spore forming rod, which is used to simulate *Bacillus anthracis*; MS2 coliphage, a viral simulant; ovalbumin, a toxin simulant; and *Erwinia herbicola*, a vegetative bacterial simulant. Twelve years ago, a program was initiated to investigate and to develop simulants for use in the U.S. Army's biological defense testing program. A set of guidelines was established to aid in the identification and selection of new potential bio-simulants. Based on these guidelines, ovalbumin and *Erwinia herbicola* were selected to be developed as biological simulants.

Certain parameters and characteristics of *Erwinia herbicola* were studied, prior to its use as a simulant in testing. Growth characteristics were examined including inoculum preparation, culture methods, growth curve study, and fermentation procedures. Short and long term storage of *Erwinia* was investigated. Dissemination of aerosolized *Erwinia* was studied in a Toroid chamber at controlled humidities and temperatures . Once it was determined that this organism was suitable as a simulant, appropriate environmental documentation was prepared, and proper state and federal permits were obtained. *Erwinia herbicola* was then included in testing protocols used at Life Sciences Division, DPG. In the fall of 1997, *Erwinia herbicola* was used in the outdoor testing, the Aerosolized Simulant Environmental Chamber (ASEC), and laboratory testing portions of Joint Field Trials (JFT) IV.

Erwinia herbicola: A Vegetative Bacterial Simulant

Douglas R. Winters, Daniel D. Martin, Arthur K. Schwedler, and Bruce G. Harper
U.S. Army Dugway Proving Ground, Dugway, UT 84022

Introduction to Simulants

Simulants are widely used in biological defense testing. Their use is advantageous from political, economic, and safety standpoints (1). Currently, there are four biological simulants which are used for testing at U.S. Army Dugway Proving Ground (DPG). These include *Bacillus subtilis* var *niger* (*Bacillus globigii* (BG)), which has been used to simulate *Bacillus anthracis*, the causative agent for anthrax. BG is a Gram negative, spore-forming, rod-shaped bacterium which is ubiquitous in nature. The MS2 coliphage, the viral simulant, is a small RNA virus which utilizes the bacterium, *Escherichia coli* as its host. The protein toxin simulant is ovalbumin. Ovalbumin is an egg white protein with molecular mass of approximately 45,000 daltons and falls within the mass range of several small molecular-weight toxins. *Erwinia herbicola* (EH) is used as a vegetative bacterial simulant. It is a Gram negative, non-spore forming, rod-shaped bacterium. This organism is also known as *Pantoea agglomerans* (2). Included in this group is *Enterobacter agglomerans*. Historically, taxonomy for this group has been confusing and unclear. Because of this, DPG uses a strain of EH which has been characterized and readily obtainable: American Type Culture Collection (ATCC, Manassas, VA) strain # 33243.

A simulant can be defined as a substance having some of the characteristics of an agent of biological origin (ABO) but is non-toxic or non-pathogenic. Some of the problematic issues in using an actual ABO as opposed to a simulant in testing are:
1. Safety
2. Environmental considerations
3. Difficulty in obtaining large quantities of materials
4. Expense
5. Public perception

Before a material can be selected as a simulant, it must meet certain criteria. Properties of an ideal simulant are as follows:

1. Safe to humans. The selected simulant must be shown to be nonpathogenic, nontoxic, and hypoallergenic to human beings.
2. Environmentally safe. The simulant must be nonpathogenic and nontoxic to plants and animals. Ideally it should not persist for a long period of time in the environment. One application of simulant use is outdoor testing. Appropriate permission must be obtained from Local, State, and Federal authorities for outdoor release of the simulant. This may be granted in the form of a permit. Prior to environmental aerosol release of EH at DPG, permits needed to be obtained.
3. Obtainable in large quantities. The simulant should be easily cultured or should be readily commercially obtainable.
4. Inexpensive. Cost should not preclude its use in testing where large amounts are

48

required.

5. Hardy. The simulant should at least be as hardy as the ABO which it is simulating. It should be able to withstand the effects of environmental factors such as UV light, freezing, heat, etc. The simulant should be able to withstand storage procedures, both long term and short term, and various forms, i.e., dry or wet. The simulant should also be able to withstand dissemination forces. It also needs to be recoverable after dissemination so as to be readily assayed.

6. Mimic the ABO. The simulant must be able to mimic at least some properties of the ABO for which it is a simulant. These may include but are not limited to aerodynamics, size, molecular weight, antigenicity, etc.

7. Reduces manpower requirements. In some instances, testing with an ABO might require the use of more than one individual. For safety reasons , it may require the use of the "buddy system". Since simulants are deemed to be innocuous, the "buddy system" would not be necessary.

8. Lower test costs. Simulants are generally less expensive than ABOs. Fewer people are required for working with simulants and less personal protective equipment is required.

9. Decrease in testing time. Fewer safety precautions mean less time required in testing.

10. Allows for open air testing. Ultimately, biological defense testing needs to be done out-of-doors.

11. Positive public perception.

Erwinia herbicola: Culture, Growth, Storage, and Aerosol Characterization

Growth and Culture:

During the early stages of development, several "strains" of EH were investigated. Biochemical analyses were performed and compared with published biochemical profiles (3). Based on those comparisons, ATCC strain #33243 was selected as the EH that was to be developed as a simulant.

Erwinia herbicola is shipped lyophilized to the customer. One ml of tryptic soy broth (TSB) is added to the ampule of lyophilized organism. Approximately 100 μl of organism is streaked on several tryptic soy agar (TSA) plates which are then incubated at 28° C overnight. Several single colonies of EH are harvested with a bacteriological loop, placed in plastic cryogenic tubes containing storage beads and cryogenic preservation media (Pro Labs Diagnostic Bead Storage System, Pro-Lab, Inc., Ontario, Canada), mixed, and stored frozen until needed.

During the initial growth studies (4), EH was incubated at 28° C, however it took ~ 30 hours to obtain colonies that were large enough to be counted. Later it was found that the growth time could be reduced by increasing the incubation temperature to 34° C without any negative effect on the EH. *Erwinia herbicola* can be grown using basic bacteriological techniques and media. For liquid growth, TSB is used. For solid media, TSA can be used. Figure 1 shows a growth curve of EH grown at 34° C. A one ml inoculum of actively growing EH was added to a slide-arm culture flask containing 250 ml of TSB. The flask was shaken at 150 rpm on a rotating platform in a 34° C incubator. Samples were withdrawn periodically for colony forming unit

49

enumeration and the optical density of the culture was monitored hourly with a Klett-Summerson photoelectric colorimeter (Klett Mfg., Inc., New York). The doubling time during the logarithmic phase was calculated to be 45 minutes.
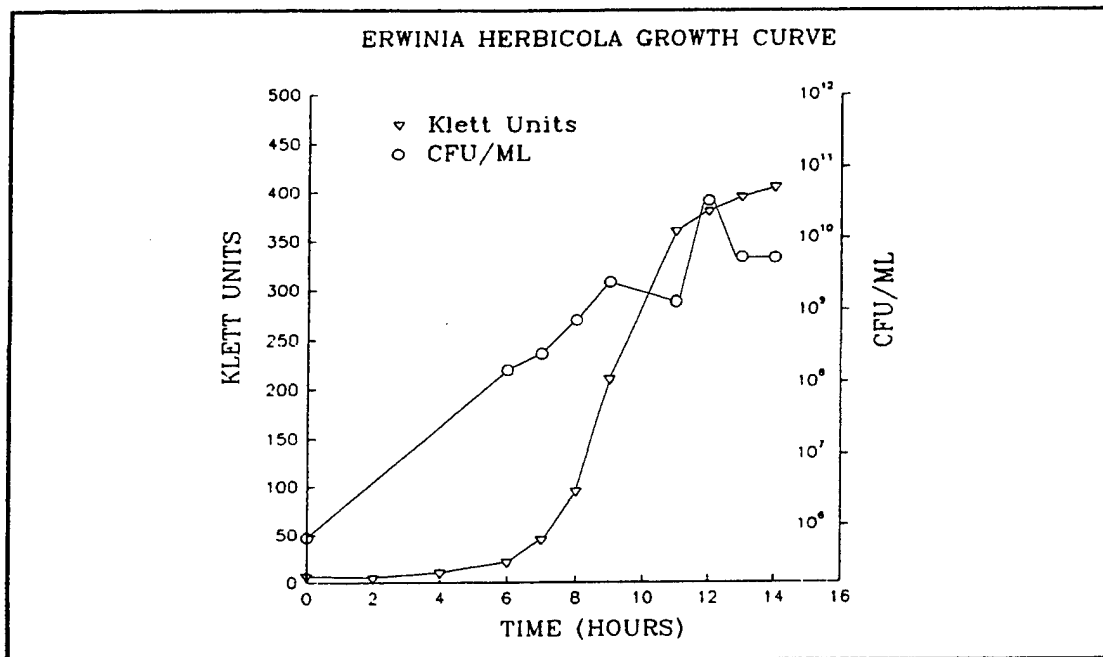
Figure 1. Growth of *Erwinia herbicola* - Colorimetric Readings and Concentration of Viable Organisms.

For small volumes of EH, growth in liquid media (TSB) in a small (250 or 500 ml) Ehrlenmeyer flask is preferred. One or two of previously frozen EH beads (see above) are placed into flasks and incubated at 34° C overnight. Larger quantities of EH may be done in fermentation vessels. Ten liter and eighty liter fermentors are routinely used at DPG. An inoculum usually consists of an actively growing culture which is 10% of the volume of the fermentation vessel. For example, an eighty liter fermentor is inoculated with approximately 8-9 liters of an actively growing culture from a ten liter fermentor run. A typical eighty liter fermentation batch of EH is run under the following conditions:

1. Temperature: initial setting: 28.5° - 29° C.
2. pH: start: 7.0 - finish: 8.6. The pH is not controlled during the fermentation process.
3. Anti-foam 289: 16 ml (Sigma Chemical Co., St. Louis, MO). .
4. Aeration: 10 l/min.
5. Inoculum: 8-9 liters EH
6. Fermentation period: 24 hours.
7. Yield: 1 x 10^9+ cfu/ml or 600-700 grams of paste.
8. Media: TSB.

A number of quality control measures are taken during the growth procedures of EH. Colony morphology and color are examined on cultures grown on solid media. The colonies

50

should be round, smooth, glistening, raised, and lemon yellow in color. Gram staining of liquid media shows small, short, plump, red-colored (Gram negative) rods. They occur singly and quite frequently in pairs. Scanning electron micrographs show the short, plump, rods with flagella. During initial studies with EH, biochemical profiles using either individual tests or kits (e.g., API diagnostic kits; bioMérieux Vitek, Inc., Hazelwood, MO), were performed on each individual strain being examined. Polyclonal antibodies have been produced in goats and rabbits against EH (ATCC #33243). These antibodies are used in immune-based assay procedures such as Enzyme Linked Immunosorbent Assay (ELISA), the Threshold® Device (Molecular Devices Corp., Sunnyvale, CA), the Origen™ Analyzer (Igen, Gaitherburg, MD). Polymerase Chain Reaction (PCR), and bacteriological plate counts are also used to detect, identify, and quantify EH.

Storage:

Other early work with EH included both short-term and long-term storage studies. Initial short-term storage studies showed a 36% reduction in bacterial counts over a 12 day period (Table 1.). Long-term studies showed a drop from 4×10^9 cfu/ml at day 0 to 3×10^8 cfu/ml at day 63. Both studies were performed with triple-washed EH, stored in distilled-deionized (dd) H_2O at 4° C. Ho's group at Defence Research Establishment Suffield, Alberta showed a 65.5% reduction in bacterial counts over a 17 day period with an *Erwinia herbicola* strain isolated from a chrysanthemum plant (5). Over a 71 day period, the counts were only 51% of the initial value in the Ho study (5).

Table 1. Viability of Stored *Erwinia herbicola* in ddH_2O at 4°C Over Time.

Time (days)	Titer (cfu/ml)	% of Initial
0	6.0×10^9	100
1	5.4×10^9	90
6	4.3×10^9	71
8	3.4×10^9	57
12	3.9×10^9	64

Aerosol Studies:

The effect of aerosolization on the survivability EH was studied. Initial investigations examined the effect of aerosolizers on the recovery of EH. Results from the comparison of near versus downstream sampling after aerosol generation in a mixing tube are shown in Table 2. The Chicago atomizer caused a greater loss of viable particles than the Collison nebulizer. The results from this comparison prompted the use of the Collison nebulizer for aerosol generation in the stability trials.

Table 2. Viability of *Erwinia herbicola* at Two Sampling Points, After Aerosol Generation with the Chicago Atomizer and Collison Nebulizer.

Generator	Near Sampling (cfu/ml in AGI)	Downstream Sampling (cfu/ml in AGI)	Average Net Loss (%)
Chicago Atomizer (two trials)	8.5×10^4	1.3×10^4	85
	7.8×10^4	1.1×10^4	
Collison Nebulizer (two trials)	4.8×10^5	4.7×10^5	20
	7.5×10^5	4.8×10^5	

In another study, the effect of relative humidity, temperature, and length of time of recovery was investigated. The Aerosol Particle Sizer® (APS®, TSI, St. Paul, MN) monitored number median aerodynamic diameter (NMAD) and mass median aerodynamic diameter (MMAD) during aerosol suspension trials with EH. The APS® data for EH are shown in Figure 2. A linear regression preformed on the NMAD and MMAD showed no significant change in either over time ($p > 0.05$). Initial aerosol viability data showed that EH could be recovered in a viable form after 2 hours at ambient temperature and relative humidity.
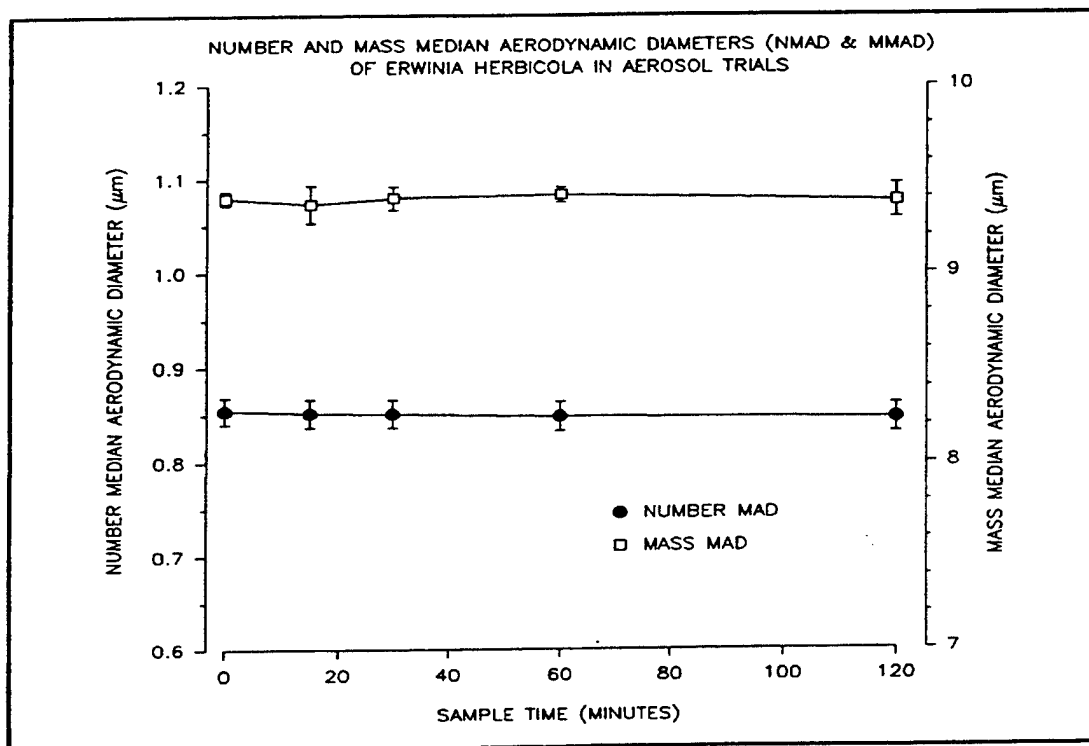

Figure 2. Particle Size and Mass Variation of *Erwinia herbicola* in Aerosol Over Time.

The Chemical-Biological Mass Spectrometer is used to analyze the daughter products of EH pyrolysis. The mass fingerprint of the pyrogram representing EH is shown in Figure 3. Peak 91 represents a unique area compared to other simulants and biological agents, which can be further analyzed by the second stage mass spectrometry.
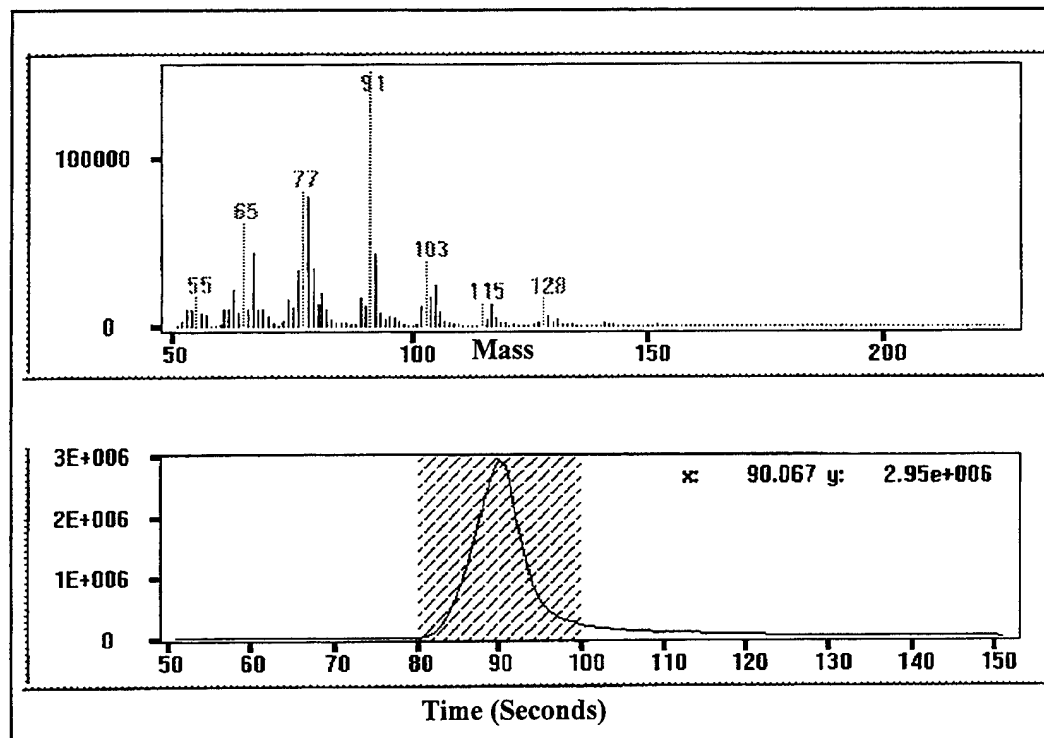

Figure 3. Mass Spectral Analysis of *Erwinia herbicola* Liquid Injection into the CBMS (upper graph-mass spectral signature of pyrogram in lower figure).

Erwinia herbicola: **Use in Laboratory Testing**

During January 1998, the laboratory phase of Joint Field Trials (JFT) IV was conducted at the Life Sciences Test Facility. The four biological simulants were used the test. Each simulant was monitored daily for concentration. MS2, BG, and ovalbumin stocks were prepared before the trial began and used throughout the testing. Because of potential loss of viability, EH stocks were made up on a weekly basis. New stocks were provided for use on days 1 and 6. Primary EH cultures or "bombs" were grown prior to the start of each test week. The bacterial counts for week one were 8.5×10^8 cfu/ml and 2.7×10^9 cfu/ml for the second week. The weekly stocks were made by diluting the "bomb" cultures in phosphate buffered saline (PBS, Boehringer Mannheim, Indianapolis, IN) prepared with sterile commercially purchased water (Baxter Healthcare Corporation, Deerfield, IL). Week one's stock was 2.4×10^6 cfu/ml and week two was 2.1×10^6 cfu/ml. Daily test samples were prepared by making dilutions with PBS + 0.5% Tween® 20 (Sigma Chemical Co., St. Louis, MO) or PBS + 0.5% Triton® X-100 (Sigma Chemical Co., St. Louis, MO) to achieve 10^5, 10^4, 10^3, $10^{2.5}$, and 10^2 cfu/ml. Figures 4 and 5 show the daily record of EH concentrations in the samples distributed to the JFT IV laboratory participants. As shown, daily fluctuations of the sample counts were negligible.
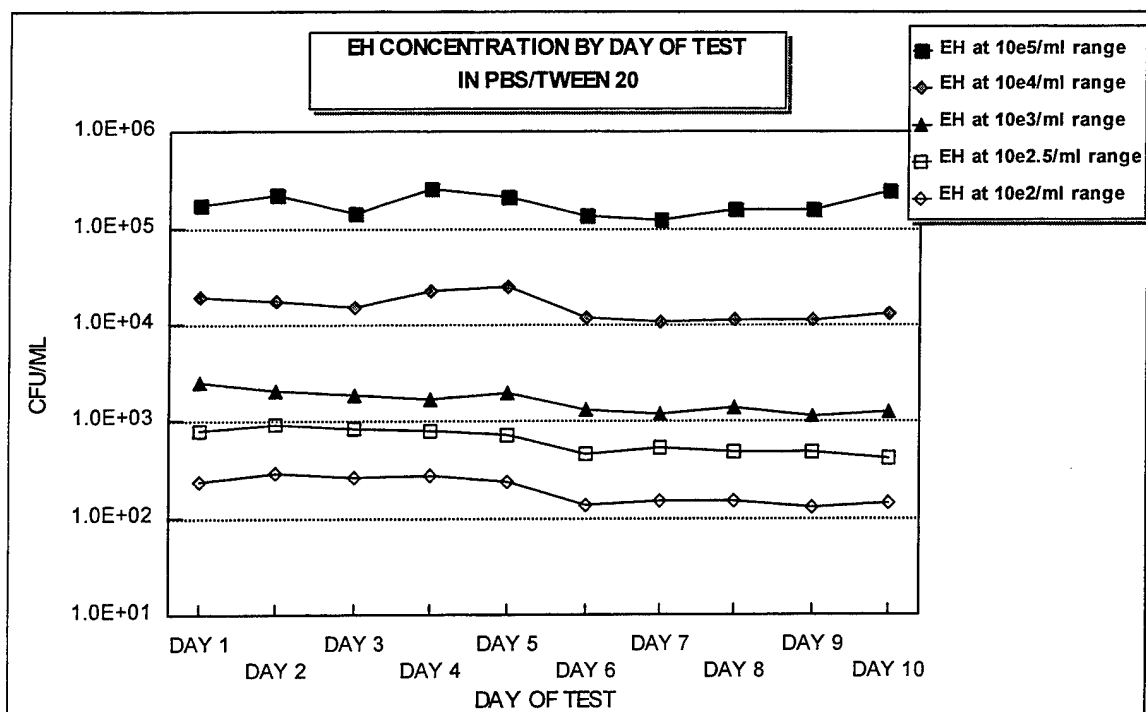
53

Figure 4. Daily record of EH concentration in samples with PBS/Tween 20; JFT IV - Laboratory.
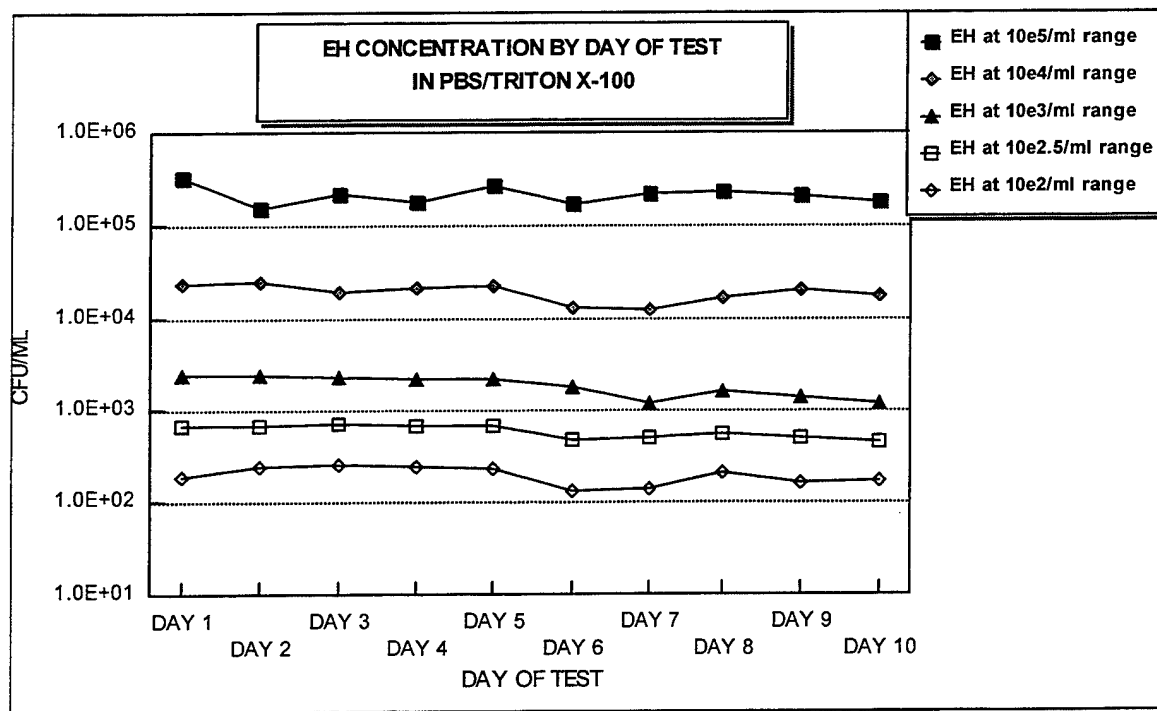
Figure 5. Daily record of EH concentration in samples with PBS/Triton X-100; JFT IV - Laboratory.

Postscript

Work with EH continues at DPG. Currently several additives are being investigated for their inclusion with EH used in aerosol trials to prevent effects from desiccation and increase viability of EH during aerosolization. Candidates include betaine, 3% trehalose, 3% raffinose, 6% sucrose, the most promising being raffinose.

References

1. **Winters, D.R., D.D. Martin, A.J. Mohr, S.M. Luo, and B.G. Harper.** " The Use of Ovalbumin as a Toxin Simulant" in *Proceedings of the Eighth International Simulant Workshop*, ERDEC-SP-038, J.E. Rhodes, H.L. Cowan, and G.R. Famini (eds.). April 1996.

2. **Gavini, F., J. Mergaert, A. Beji, C. Mielcarek, D. Izard, K. Kersters, and J. De Ley.** 1989. Transfer of *Enterobacter agglomerans* (Beijerinck 1888) Ewing and Fife 1972 to *Pantoea agglomerans* comb. nov. and Description of *Pantoea dispersa* sp. nov. Int. J. Syst. Bacteriol. 39:337-345.

3. **Krieg, N.R. and J.G. Holt.** 1984. Bergey's Manual of Systemic Bacteriology, Vol. 1. The Williams and Wilkins Co., Baltimore, pp. 469-476.

4. **Winters, D.R., D.D. Martin, J.S. Allen, B. Johnson, A.J. Mohr, S.M. Luo, and B.G. Harper.** 1994. Methodology Investigation, Final Report of Initial Evaluation of *Erwinia herbicola* as a Vegetative Bacterial Simulant. Dugway Proving Ground, Utah. DPG No.: DPG-FR-94-704. AD No.: B196811.

5. **Ho, J., R. Munro, and A.R. Bhatti.** May 1989. Characterization of a Common Herbaceous Bacterial Isolate Suitable for a BW Vegetative Simulant. Suffield Report No. 518. Defence Research Establishment Suffield, Ralston, Alberta.

THIS PAGE INTENTIONALLY LEFT BLANK

Poster Program

THIS PAGE INTENTIONALLY LEFT BLANK

Microbial Light Scattering to Detect Metallic Toxins

B. V. Bronk, U.S.Air Force Armstrong Lab. At Army ERDEC

SCBRD-RT, Aberdeen Proving Ground, Aberdeen, MD 21010

Z. Z. Li, Biomedical Instrumentation Center, Uniformed Services

University of the Health Science, Bethesda, Maryland 20814

BACKGROUND AND RESULTS

1. Mathematical interpretation of polarized light scattering (PLS):

$$\begin{bmatrix} I_s \\ Q_s \\ U_s \\ V_s \end{bmatrix} = \begin{bmatrix} S_{11} & S_{12} & S_{13} & S_{14} \\ S_{21} & S_{22} & S_{23} & S_{24} \\ S_{31} & S_{32} & S_{33} & S_{34} \\ S_{41} & S_{42} & S_{43} & S_{44} \end{bmatrix} \begin{bmatrix} I_0 \\ Q_0 \\ U_0 \\ V_0 \end{bmatrix}$$

2. The angular function associated with the Mueller matrix ratio , S34/S11 is sensitive measure for scattering of polarized light from bacterial suspension, especially a rod-shape cells.[1]

3. The PLS technique demonstrated that rapid changes in cell diameter after nutritional shift in bacterial medium are directly observable on a computer screen[2]. The particular peak location in a graph is an important indicator to detect the cell environmental changes. For instance, enriched medium causes cell immediate growth, which is able to be seen in PLS curve (Figure 2) in 5-10 minutes. This study shows that PLS also is available to be used to measure the metallic toxicity in vivo[3]. The cell growth inhibited by toxins is displayed in PLS curve with slow or cease of nutritional upshift (Figure 3).

4. The ratio of angular shift rate (degree per minute) of cells treated with toxin to that treated with no toxin is difined as "relative activity, shown in Figure 4 to 7 and Table 1.

MATERIAL AND METHODS

1. Bacterial strains of *Escherichia coli k12* (ATCC 49539) is used in the study.

2. Bacterial culture was grown in LB broth overnight (18-20 hrs) at 30 C.

3. The cells are spun down, wash once with sterile distilled water, and resuspended in water at optical density (~0.3)

4. Bacterial sample (5 ml) is incubated with/without a toxicant for 15 min at room temperature.

5. Samples are centrifuged at 9,000 rpm for 10 min, the pellets are washed twice with sterile water and resuspended to PBS (pH~7.4).

6. 5 ml of each resuspended sample at OD ~0.1 is used for polarized light scattering test.

7. Nutrition up-shift experiment is performed in cuvette in a series of time after adding 2xLB (final concentration is 1x) into a test sample .

8. Scattering curves from 20 degree to 120 degree are automatically recorded by a computer system.

9. Colony Forming Unit assay is performed with all of samples detected by polarized light scattering method.
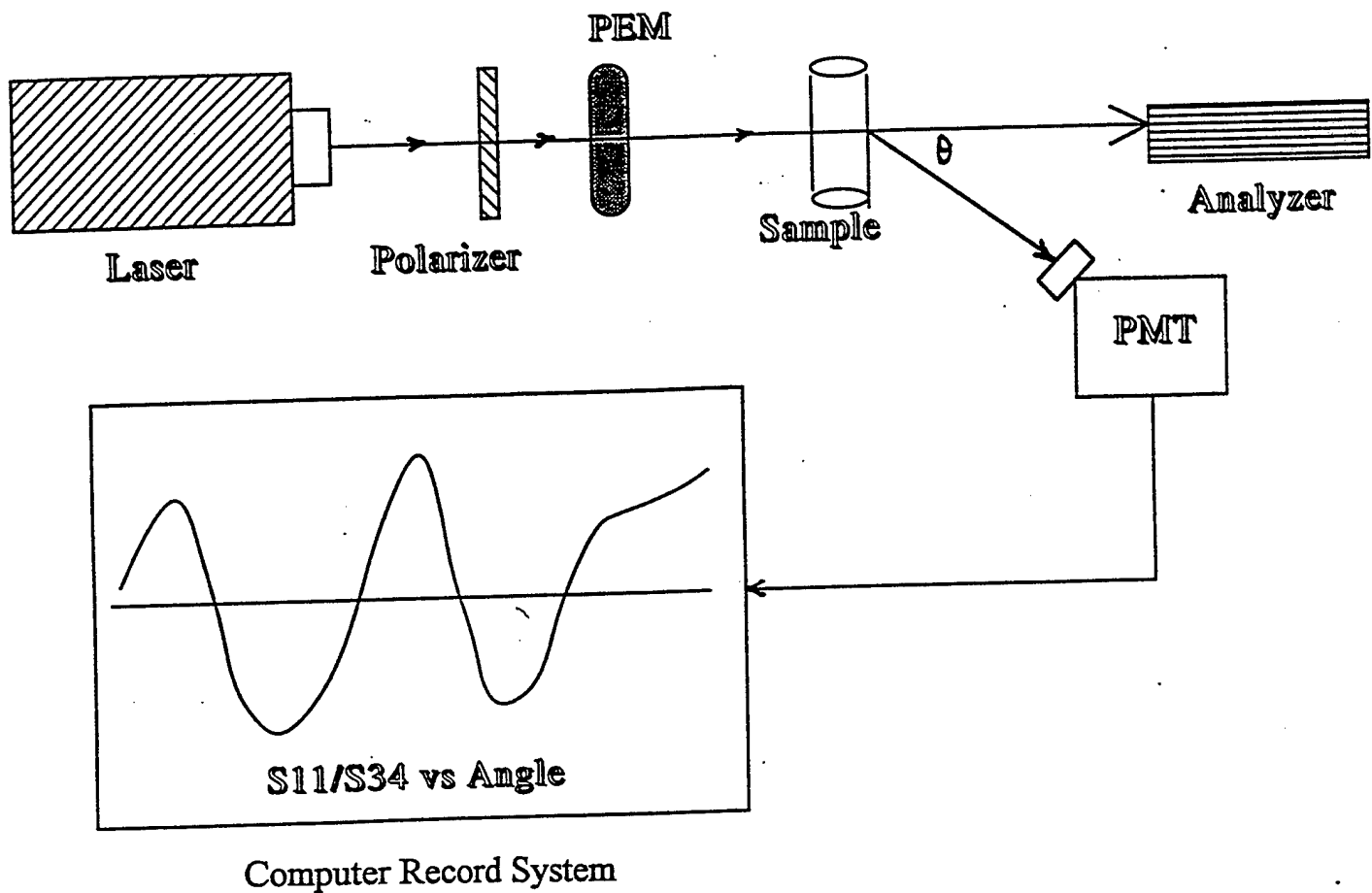
Figure 1   Simplified Diagram of Polarized Light Scattering Experimental Set-up:

The laser light is linearly polarized before traversing a photoelastic

modulator (PEM). The lighst is scattered from the bacteria in cuvette ,

and is observed at an angle θ through an analyzer by a photomultiplier

(PMT).

Shift of Peak of Polarized Light Scattering Curve at Various Times Following Medium Upshift with no Toxicant Presence

Figure 2

63
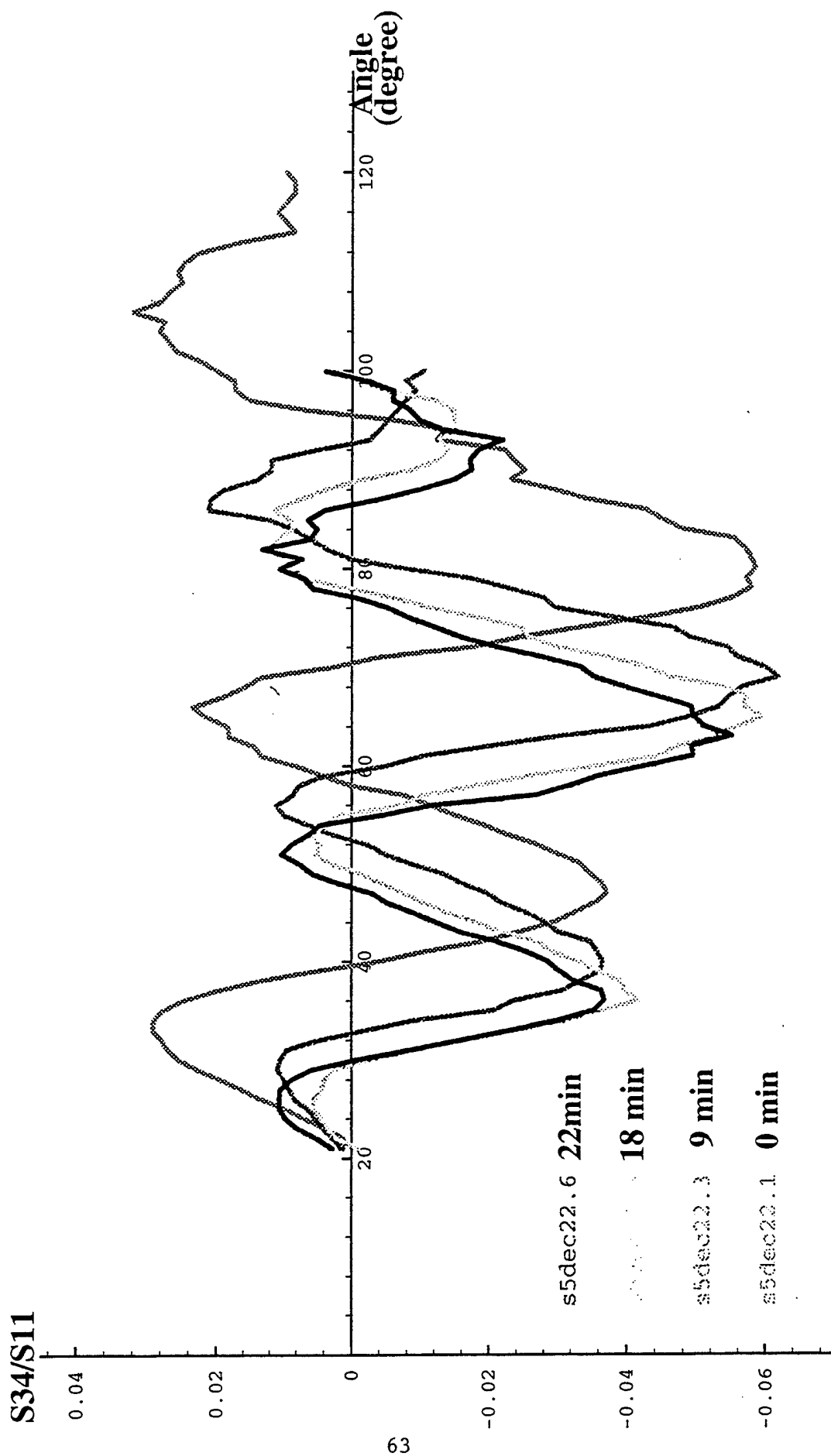
Nutrution Up-Shift Study on *E coli K12* Treated with/without Hg^{++}

Figure 3

64
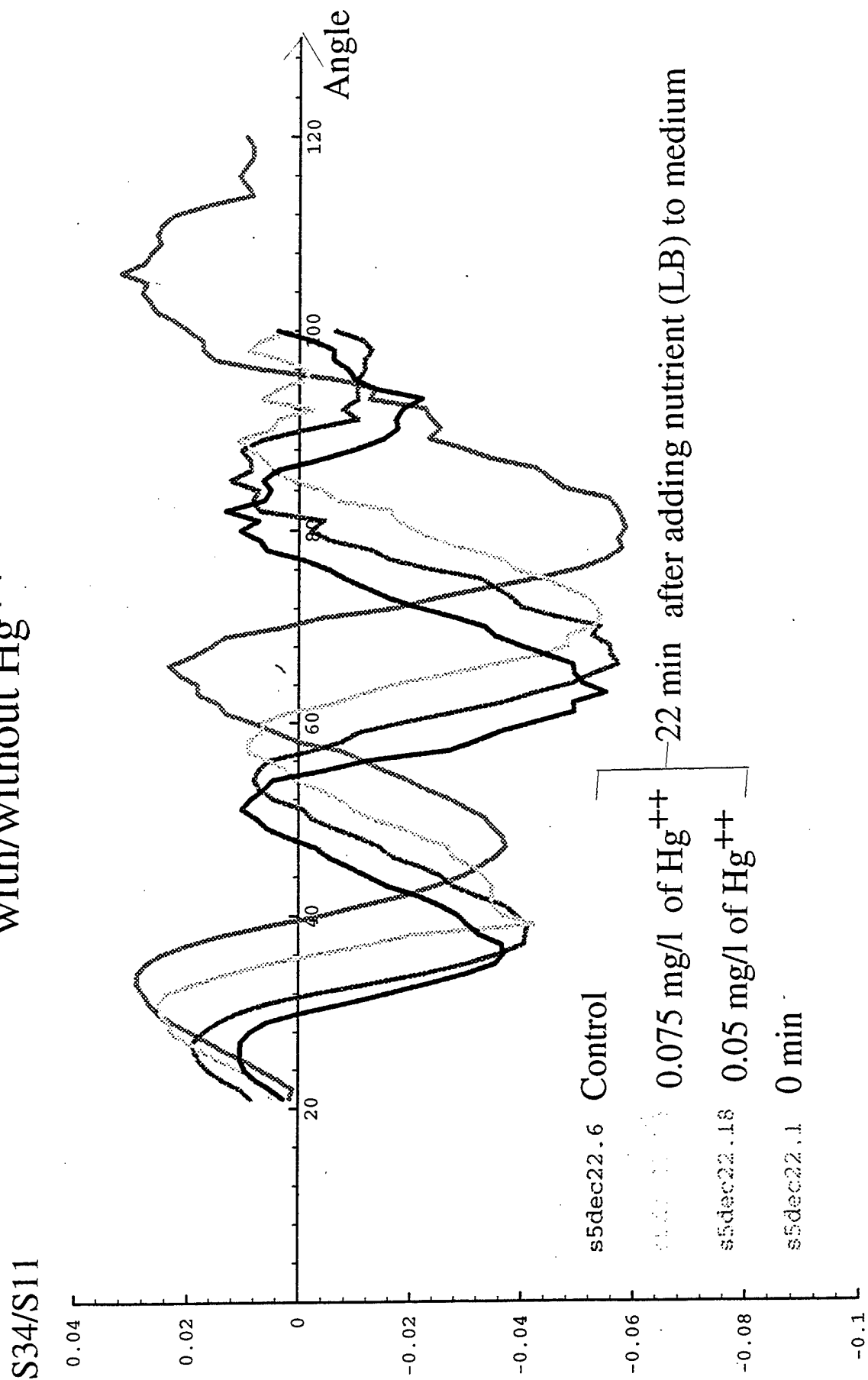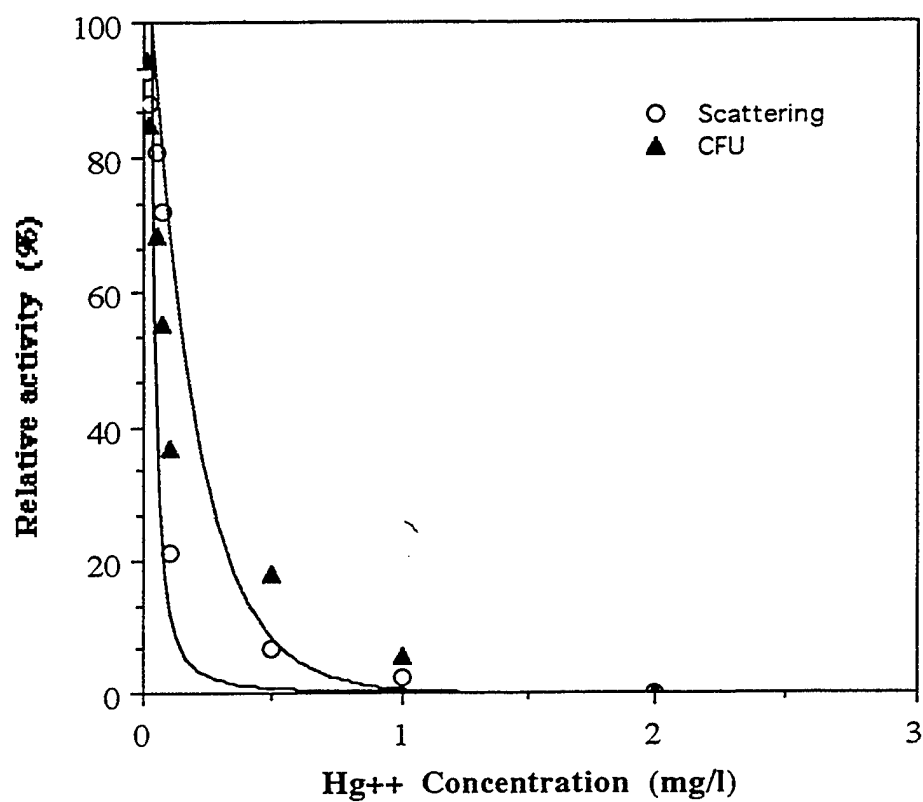
Figure 4 Relative activity of PLS and CFU vs Hg++ concentration
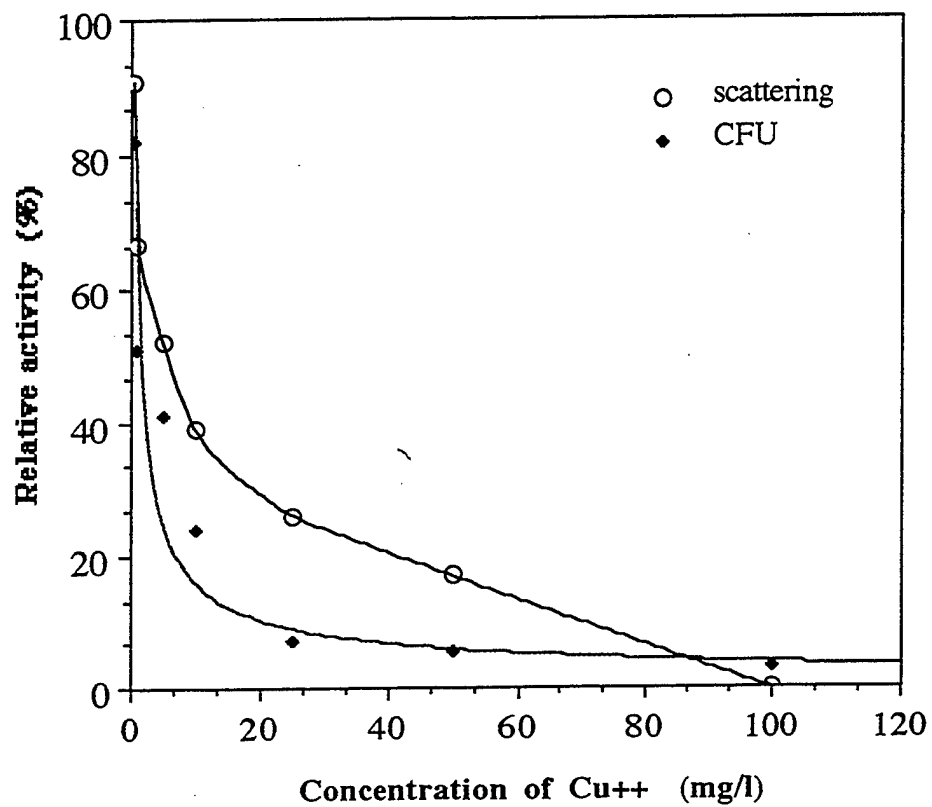
Figure 5   Relative activity of PLS and CFU vs Cu++ concentration   (mg/l)
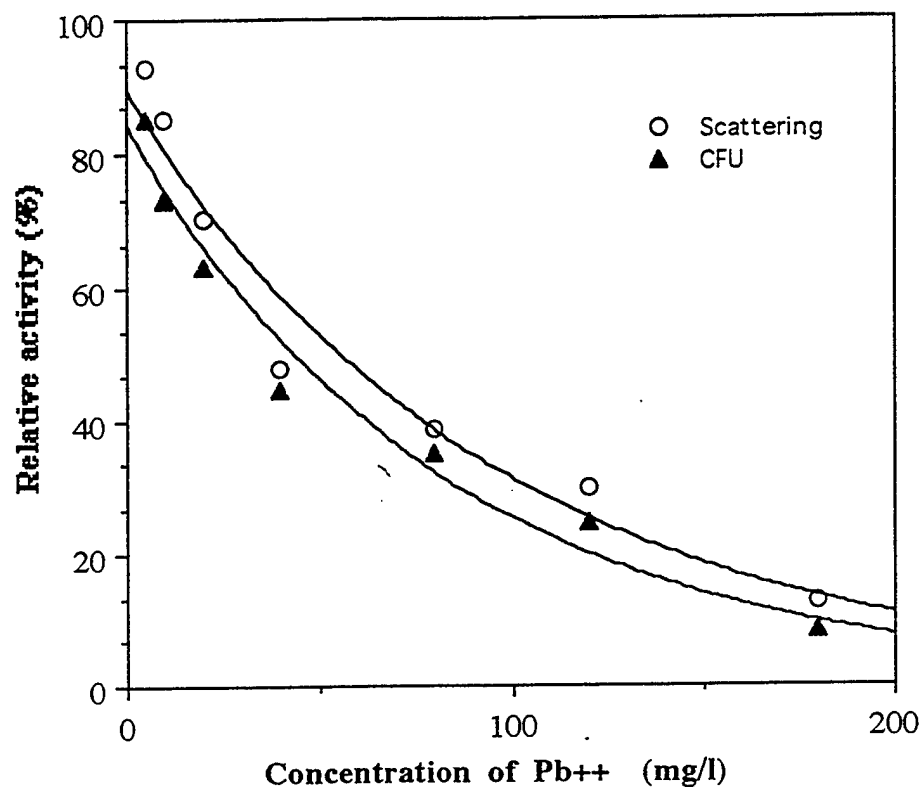
Figure 6 Relative activity of PLS and CFU vs Pb++ concentration
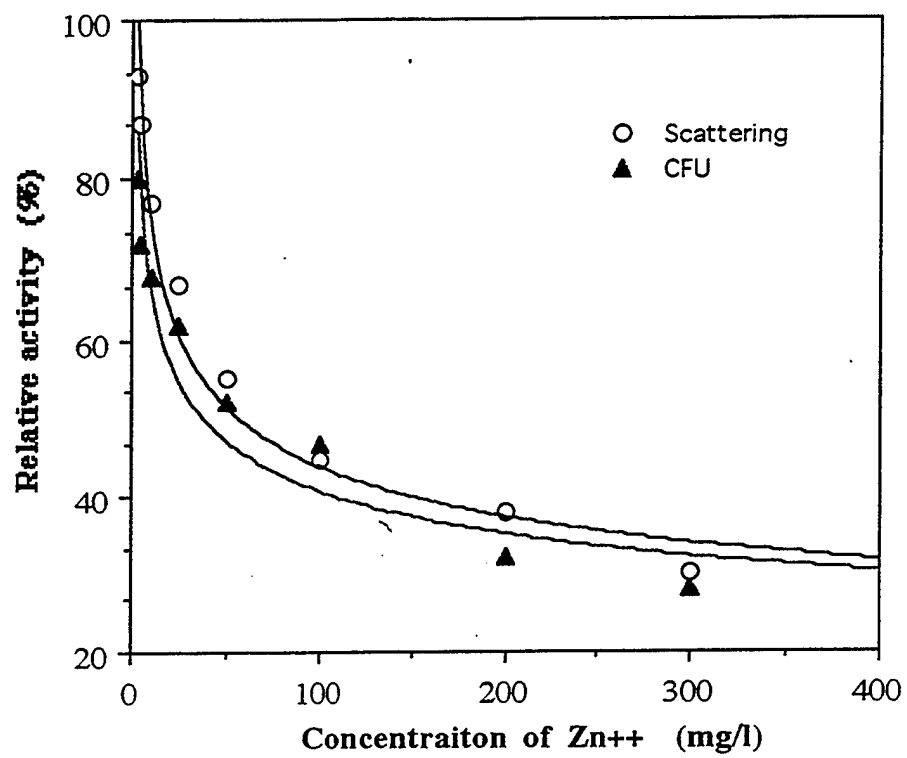
Figure 7   Relative activity of PLS and CFU vs Zn++ concentration

Table 1 Scattering Up-Shift Rate of Heavy Metals at Varied Concentrations

Group	Number of Experiment	Up-shift Rate + S.D Degree per minute
Control	14	0.64+0.02
Hg^{2+}(mg/l)	8	
0.01		0.60+0.02
0.05		0.52+0.02
0.1		0.07+0.01
Ag^{+}(mg/l)	6	
0.017		0.59+0.05
0.17		0.43+0.03
0.51		0.13+0.02
Cu^{2+}(mg/l)	6	
0.5		0.58+0.05
5.0		0.33+0.02
50.0		0.11+0.01
Pb^{2+}(mg/l)	5	
5.0		0.60+0.03
20.0		0.45+0.05
120		0.16+0.02
Zn^{2+}	5	
2.5		0.60+0.05
25.0		0.43+0.04
200		0.24+0.02

Note: At least three experiments were performed for each concentration of any metal.

Table 2   The Toxicity (EC50) of Five Toxicants Obtained by PLS and CFU Assay.

Chemical	EC50 (Toxicant Concentration) (mg/l / µM/l)			
	PLS Method	CFU Assay	Other Method*	Refs**.
Hg^{++}	0.07/0.26	0.09/0.33	0.05 - 1.6	Dutka, BJ 1984 Beaubien,A 1984
Ag^+	0.31/1.8	0.26/1.5	2.0	Schreurs,WJA 1992
Cu^{++}	5.3/21.2	2.9/11.6	3.2 - 3.8	King,EF 1984 Dutka,BJ 1984
Pb^{++}	36/129	31/112	1.7 - 30.2	Bitton, 1994 [4]
Zn^{++}	71/247	67/233	3.5 - 238	Beaubien,A 1984 Dutka, BJ 1984

* The concentration of other methods use mg per liter as the unit for the metallic salts.

** Most of them are from Liu, D., and Dutka, BJ., Eds: "Toxicity screening procesure using bacterial systems", Marcel Dekker, N.Y. 1984.

SUMMARY

We introduced a rapid new technique which can be used for detecting small concentrations of environmental toxicants by means of changes in the scattering of polarized light from a suspension of bacteria. We measure the angular scattering pattern of the ratio, S34/S11 of two Mueller matrix elements. Our previous studies indicated that the peak locations in this oscillating graph of S34/S11 vs scattering angle are correlated with the diameters of the rod shaped bacteria in suspension from which the light is scattered. We further found that a rapid upshift from poor (small bacteria) to rich media (bacteria became large) led to a rapid shift of the peaks toward smaller angles when this experiment was done with *E coli K12*.

The rationale for using this procedure to test toxicants is that if the most of bacteria do not survive a certain level of toxicity as measured by Colony Forming Units (CFU) then we might observe that a halt to their growth to large size might occur very rapidly. This indeed occurs, and a toxicity response measured by S34/S11 vs angle is close correlated to the response measured by CFU. To measure the former we calculate the angular shift-rate of the second peak (~70 degrees) occurring during the first ~25 minutes after upshift. We calculate the ratio of this rate with toxicant compared to that for the control (no toxicant). This shift-rate or relative activity is plotted against toxicant dose in the graph shown. Relative activity for CFU is simply the survival ratio.

The effective concentration for 50% relative activity (EC50) is obtained from these graphs and from similar graphs for CFU. We show results for five different ions and tabulate the EC50 in each case and compare results with values for other methods available in the literature. The present methods is quite rapid and could probably be accomplished in 15 minutes with improved instrumentation.

REFERENCES

1. B. V. Bronk, W. P. Van De Merwe and M. Stanley, 1992.

   An vivo measure of average bacterial cell size from a polarized light scattering function, Cytometry 13 p.155-162.

2. W. P. Van De Merwe, Z.Z. Li, B.V. Bronk and J. Czege, 1997.

   Polarized light scattering from bacteria for rapid observation of size changes following nutritional upshift, Biophysical J. Vol.73 500-506.

3. B. V. Bronk, Z. Z. Li, W.P. Van De Merwe and J. Czege, 1997

   In vitro method for detecting toxicants by changing in pattern of polarized light scattering, Chapter 45 in "Advances in animal alternatives for safety and efficacy Testing" pp.427-43, editiors Salem and Katz, Taylor and Francis, Publ., Wash. D.C. .

4. G. Bitton, K. Jung, B. Koopman, 1994. Evaluation of a microplate assay specific for heavy metal toxicity, Arch. Environ. Contam. Toxicol., 27, 25-28.

Optical Properties of Aerosols

THIS PAGE INTENTIONALLY LEFT BLANK

THEORETICAL DEMONSTRATION OF THE LOCALIZATION PRINCIPLE FOR A FOCUSED LIGHT SHEET INCIDENT UPON AN INFINITE CYLINDER

John P. Barton

Department of Mechanical Engineering
College of Engineering & Technology
University of Nebraska-Lincoln
Lincoln, NE 68588-0656

RECENT PUBLICATIONS, SUBMITTALS FOR PUBLICATION, AND PRESENTATIONS

A.) J.P. Barton, "Electromagnetic field calculations for an arbitrary focused beam incident upon an infinite circular cylinder," presentation at the 1998 Scientific Conference on Obscuration and Aerosol Research, U.S. Army Edgewood Research Development and Engineering Center, Aberdeen Proving Ground, Maryland, 1998.

B.) J.P. Barton, "Calculated forward and backward light scattering patterns for irregularly-shaped particles," Proceedings of the 1997 Scientific Conference on Obscuration and Aerosol Research, U.S. Army Edgewood Research Development and Engineering Center, Aberdeen Proving Ground, Maryland, 1997.

C.) J.P. Barton, "Electromagnetic field calculations for a sphere illuminated by a higher-order Gaussian beam. II. Farfield scattering," Applied Optics, Vol. 37, No. 15, pp. 3339-3344, 1998.

D.) J.P. Barton, "Systematic far-field scattering calculations for prolate and oblate spheroids with axis ratios from 1.3 to 4.0," Proceedings of the 5th International Congress on Optical Particle Sizing, August 10-14, 1998, Minneapolis, Minnesota, pp. 45-48, 1998.

E.) J.P. Barton, "Theoretical calculations of the effects of beam shape and particle geometry on far-field scattering," presentation at the 1997 Scientific Conference on Obscuration and Aerosol Research, U.S. Army Edgewood Research Development and Engineering Center, Aberdeen Proving Ground, Maryland, 1997.

F.) J.P. Barton, "Light scattering calculations for irregularly-shaped axisymmetric particles of homogeneous and layered composition," Measurement Science and Technology, Vol. 9, pp. 151-160, 1998.

G.) J.P. Barton, "Internal and near-surface electromagnetic fields for an infinite cylinder illuminated by an arbitrary focused beam," submitted to the Journal of the Optical Society of America A, May, 1998.

H.) H-B. Lin, J.D. Eversole, A.J. Campillo, and J.P. Barton, "Excitation localization principle for spherical microcavities," submitted to Optics Letters, August, 1998.

ABSTRACT

A separation of variables solution is used to demonstrate the validity of the localization principle for the two dimensional arrangement of a focused light sheet incident upon an infinite circular cylinder at resonance. For the conditions considered (complex index of refraction = (1.50,0.00); particle size parameters of the order of 40; 1st, 2nd, and 3rd order resonances; electric field polarization in both the parallel and perpendicular directions), it was found, consistent with the localization principle,

that the most efficient resonance excitation could be obtained by focusing the light sheet slightly outside the surface of the cylinder. Future work will include conducting a similar investigation of the validity of the localization principle for the three dimensional arrangement of a focused laser beam incident upon an infinite circular cylinder.

I. INTRODUCTION

In Ref. 1 it was shown that morphology dependent resonances (MDR's) that occur in spherical particles can be most efficiently excited using a focused laser beam oriented so that the focal point of the laser beam strikes just outside the surface of the particle. This effect, sometimes referred to as the "localization principle" is related to the original work of van de Hulst[1,2] who observed, for radii much greater than a wavelength, that the lth partial wave may be associated with a ray passing through a radial position given by

$$\tilde{r} = (l + 1/2)/\alpha \tag{1}$$

where l is the spherical coordinate radial index, $\tilde{r} = r/a$ where a is the radius of the sphere, and $\alpha = 2\pi a/\lambda_{ext}$ is the particle size parameter. Since in general, for an MDR, $l > \alpha$, Eq. (1) implies that for the optimum excitation of the lth radial index resonance, the radial position of the focal point of the laser should be at $r > a$.

Recently there has been interest in the geometry of a focused laser beam incident upon an infinite cylinder (e.g., a laser beam incident upon an optical fiber or upon a stream of liquid). In the following, calculations are presented investigating the validity of the localization principle for the two dimensional arrangement of the a focused laser light sheet incident upon an infinite circular cylinder.

II. THEORETICAL DEVELOPMENT

A homogeneous, circular cross section (radius $= a$), infinitely long cylinder within an infinite, homogeneous, nonabsorbing medium is considered. Both the cylinder and the surrounding medium are assumed to be isotropic and nonmagnetic ($\mu = 1$). The incident field (in this case a focused light sheet) is monochromatic (an implicit time dependence of $\exp(-i\omega t)$ is assumed) and plane two dimensional (i.e., nonvarying along the length of the cylinder). All electromagnetic quantities are nondimensionalized relative to a characteristic electric field amplitude associated with the incident field and all spatial quantities are nondimensionalized relative to the cylinder radius (a). The incident field (designated by the superscript i) is assumed to be known, and the internal electromagnetic field (designated by the superscript w) and the scattered electromagnetic field (designated by the superscript s) of the cylinder are to be determined.

The solution is formulated in cylindrical coordinates (r, θ, z) with the z axis oriented along the length of the cylinder (see Fig. 1). Following the development of Ref. 3 (solution for an irregularly-shaped, layered cylindrical particle with arbitrary illumination), the incident, internal, and scattered electromagnetic fields are each expressed as general series expansions and then the series coefficients of the internal and scattered fields are related to the series coefficients of the incident field by application of the boundary conditions associated with the continuity of the tangential components of the electromagnetic field at the surface of the cylinder. Also as discussed in Ref. 3, the electric wave case ($H_z = 0$, incident electric field polarization parallel to the length of the cylinder) and the magnetic wave case ($E_z = 0$, incident electric field polarization perpendicular to the length of the cylinder) are considered separately. However, because of the linearity of the controlling equations, the two solutions could be summed together to form a more general solution.

A. Electric Wave Case

For the electric wave case, $H_z = 0$, $E_r = 0$, and $E_\theta = 0$.[3] Otherwise, the nonzero electromagnetic field components can be expressed as follows.

$$E_z^{(w)} = \sum_{l=-\infty}^{\infty} c_l J_l(\bar{n}\alpha\tilde{r})exp(il\theta) \, , \tag{2}$$

$$H_r^{(w)} = \frac{\sqrt{\epsilon_{ext}}}{\alpha\tilde{r}} \sum_{l=-\infty}^{\infty} l c_l J_l(\bar{n}\alpha\tilde{r})exp(il\theta) \, , \tag{3}$$

$$H_\theta^{(w)} = i\sqrt{\epsilon_{ext}}\bar{n} \sum_{l=-\infty}^{\infty} c_l J_l'(\bar{n}\alpha\tilde{r})exp(il\theta) \, , \tag{4}$$

$$E_z^{(s)} = \sum_{l=-\infty}^{\infty} a_l H_l^{(1)}(\alpha\tilde{r})exp(il\theta) \, , \tag{5}$$

$$H_r^{(s)} = \frac{\sqrt{\epsilon_{ext}}}{\alpha\tilde{r}} \sum_{l=-\infty}^{\infty} l a_l H_l^{(1)}(\alpha\tilde{r})exp(il\theta) \, , \tag{6}$$

$$H_\theta^{(s)} = i\sqrt{\epsilon_{ext}} \sum_{l=-\infty}^{\infty} a_l H_l^{(1)\prime}(\alpha\tilde{r})exp(il\theta) \, , \tag{7}$$

$$E_z^{(i)} = \sum_{l=-\infty}^{\infty} A_l J_l(\alpha\tilde{r})exp(il\theta) \, , \tag{8}$$

$$H_r^{(i)} = \frac{\sqrt{\epsilon_{ext}}}{\alpha\tilde{r}} \sum_{l=-\infty}^{\infty} l A_l J_l(\alpha\tilde{r})exp(il\theta) \, , \tag{9}$$

and

$$H_\theta^{(i)} = i\sqrt{\epsilon_{ext}} \sum_{l=-\infty}^{\infty} A_l J_l'(\alpha\tilde{r})exp(il\theta) \, , \tag{10}$$

where $\bar{n} = \sqrt{\epsilon_{int}/\epsilon_{ext}}$ is the complex relative index of refraction of the cylinder and $H_l^{(1)} = J_l + iN_l$ is the cylindrical Hankel function of the first kind. An application of boundary conditions (continuity of E_z and H_θ at the surface of the cylinder) leads to the following expressions for the series coefficients.

$$a_l = \frac{\bar{n} J_l(\alpha) J_l'(\bar{n}\alpha) - J_l(\bar{n}\alpha) J_l'(\alpha)}{J_l(\bar{n}\alpha) H_l^{(1)\prime}(\alpha) - \bar{n} J_l'(\bar{n}\alpha) H_l^{(1)}(\alpha)} A_l \tag{11}$$

and

$$c_l = \frac{2i/\pi\alpha}{J_l(\bar{n}\alpha) H_l^{(1)\prime}(\alpha) - \bar{n} J_l'(\bar{n}\alpha) H_l^{(1)}(\alpha)} A_l \tag{12}$$

where

$$A_l = \frac{1}{2\pi J_l(\alpha)} \int_0^{2\pi} E_z^{(i)}(a,\theta)exp(-il\theta) \, d\theta \, . \tag{13}$$

B. Magnetic Wave Case

The development for the magnetic wave case is similar to that of the electric wave case except now, $E_z = 0$, $H_r = 0$, and $H_\theta = 0$,[3] and the appropriate expressions for the nonzero electromagnetic field components are as follows.

$$E_r^{(w)} = -\frac{1}{\sqrt{\epsilon_{ext}}\bar{n}^2\alpha\tilde{r}} \sum_{l=-\infty}^{\infty} l d_l J_l(\bar{n}\alpha\tilde{r}) exp(il\theta) \ , \tag{14}$$

$$E_\theta^{(w)} = -\frac{i}{\sqrt{\epsilon_{ext}}\bar{n}} \sum_{l=-\infty}^{\infty} d_l J_l'(\bar{n}\alpha\tilde{r}) exp(il\theta) \ , \tag{15}$$

$$H_z^{(w)} = \sum_{l=-\infty}^{\infty} d_l J_l(\bar{n}\alpha\tilde{r}) exp(il\theta) \ , \tag{16}$$

$$E_r^{(s)} = -\frac{1}{\sqrt{\epsilon_{ext}}\alpha\tilde{r}} \sum_{l=-\infty}^{\infty} l b_l H_l^{(1)}(\alpha\tilde{r}) exp(il\theta) \ , \tag{17}$$

$$E_\theta^{(s)} = -\frac{i}{\sqrt{\epsilon_{ext}}} \sum_{l=-\infty}^{\infty} b_l H_l^{(1)\prime}(\alpha\tilde{r}) exp(il\theta) \ , \tag{18}$$

$$H_z^{(s)} = \sum_{l=-\infty}^{\infty} b_l H_l^{(1)}(\alpha\tilde{r}) exp(il\theta) \ , \tag{19}$$

$$E_r^{(i)} = -\frac{1}{\sqrt{\epsilon_{ext}}\alpha\tilde{r}} \sum_{l=-\infty}^{\infty} l B_l J_l(\alpha\tilde{r}) exp(il\theta) \ , \tag{20}$$

$$E_\theta^{(i)} = -\frac{i}{\sqrt{\epsilon_{ext}}} \sum_{l=-\infty}^{\infty} B_l J_l'(\alpha\tilde{r}) exp(il\theta) \ , \tag{21}$$

and

$$H_z^{(i)} = \sum_{l=-\infty}^{\infty} B_l J_l(\alpha\tilde{r}) exp(il\theta) \ . \tag{22}$$

From the application of boundary conditions (continuity of H_z and E_θ at the surface of the cylinder) the following expressions for the series coefficients are then derived.

$$b_l = \frac{J_l(\alpha)J_l'(\bar{n}\alpha) - \bar{n}J_l(\bar{n}\alpha)J_l'(\alpha)}{\bar{n}J_l(\bar{n}\alpha)H_l^{(1)\prime}(\alpha) - J_l'(\bar{n}\alpha)H_l^{(1)}(\alpha)} B_l \tag{23}$$

and

$$d_l = \frac{2i/\pi\alpha}{\bar{n}J_l(\bar{n}\alpha)H_l^{(1)\prime}(\alpha) - J_l'(\bar{n}\alpha)H_l^{(1)}(\alpha)} B_l \tag{24}$$

where

$$B_l = \frac{1}{2\pi J_l(\alpha)} \int_0^{2\pi} H_z^{(i)}(a,\theta) exp(-il\theta) \, d\theta \ . \tag{25}$$

III. CALCULATIONS

In order to investigate the validity of the localization principle for a circular cylinder, a set of systematic calculations were performed. An external dielectric constant of $\epsilon_{ext} = 1$ and a complex relative index of refraction of $\bar{n} = (1.50,0.00)$ were assumed. The MDR's were located and identified

78

by determining the total electromagnetic energy (per unit length) within the cylinder, as a function of particle size parameter (α), using

$$U' = \frac{1}{16\pi} \int_0^1 \int_0^{2\pi} \left[Real(\tilde{\epsilon}_{int}) |\vec{E}|^2 + |\vec{H}|^2 \right] \tilde{r} d\theta d\tilde{r} \ . \tag{26}$$

Assuming plane wave illumination, the results for the electric wave case ($36 < \alpha < 40$) are shown in Fig. 2. The regions of increased U' are associated with MDR's. The smaller peaks are third order resonances, the next higher peaks are second order resonances, and the "hyperfine" peaks that extend off the top of the graph are first order resonances. The corresponding results for the magnetic wave case are shown in Fig. 3.

For the electric wave case, the $l = 53$, 1st order resonance (c_{53}^1, $\alpha = 39.19199826$) the $l = 48$, 2nd order resonance (c_{48}^2, $\alpha = 39.38244$), and the $l = 44$, 3rd order resonance (c_{44}^3, $\alpha = 39.550$) were chosen to investigate resonance excitation using a focused light sheet. The light sheet is assumed to propagate in the x-axis direction with the focal point on the y-axis (focal point positioning, $\tilde{x}_0 = 0$, $\tilde{y}_0 =$ variable). The electromagnetic field components of the focused light sheet were determined by applying the analytical expressions given in Appendix A of Ref. 3. The beam waist radius ($\tilde{w}_0 = w_0/a$) was assumed to be 0.25. The effects of focal point positioning on resonance excitation for each of the three resonances (a nonresonance case is also included) are shown in Fig. 4. As can be seen in Fig. 4, consistent with the localization principle, each of the three resonances are most strongly excited for focal point positioning outside the surface of the particle. A comparison of the calculated focal point location for maximum resonance excitation with that predicted by Eq. (1) is given in Table I. As can be observed in Table I., the theoretical calculations agree almost identically for the 1st and 2nd order resonances, and approximately agree for the 3rd order resonance. The results for the corresponding magnetic wave resonances (d_{53}^1, d_{48}^2, and d_{44}^3), as given in Fig. 5 and Table I, show similar agreement.

IV. SUMMARY

A separation of variables solution has been used to demonstrate the validity of the localization principle for the two dimensional arrangement of an infinite circular cylinder illuminated by a focused light sheet. Future efforts will include an investigation of the validity of the localization principle for the three dimensional arrangement of a focused laser beam incident upon an infinite circular cylinder.[4]

V. REFERENCES

1.) J.P. Barton, D.R. Alexander, and S.A. Schaub, "Internal fields of a spherical particle illuminated by a tightly focused laser beam: Focal point positioning effects at resonance," Journal of Applied Physics, Vol. 65, pp. 2900-2906, 1989.

2.) H.C. van de Hulst, *Light Scattering by Small Particles*, Dover Publishing, New York, 1981.

3.) J.P. Barton, "Electromagnetic field calculations for irregularly shaped, layered cylindrical particles with focused illumination," Applied Optics, Vol. 36, pp. 1312-1319, 1997.

4.) J.P. Barton, "Internal and near-surface electromagnetic fields for an infinite cylinder illuminated by an arbitrary focused beam," submitted to the Journal of the Optical Society of America A, May, 1998.
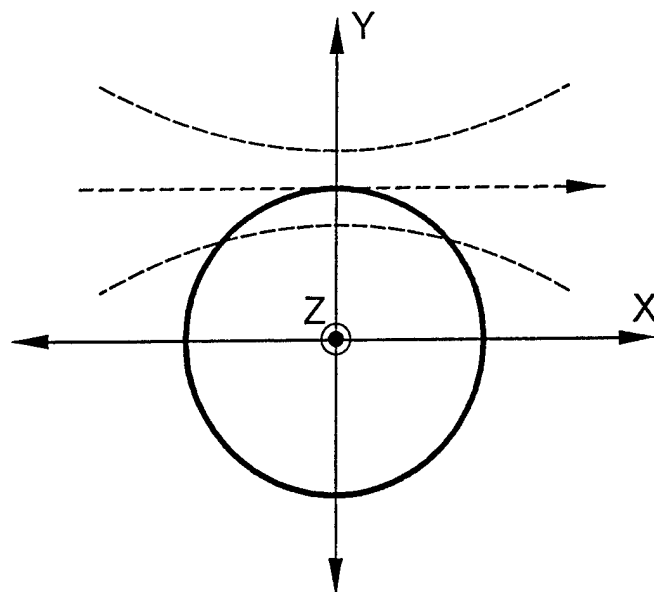
FIG 1. Geometrical arrangement for the focused light sheet incident upon an infinite circular cylinder problem.
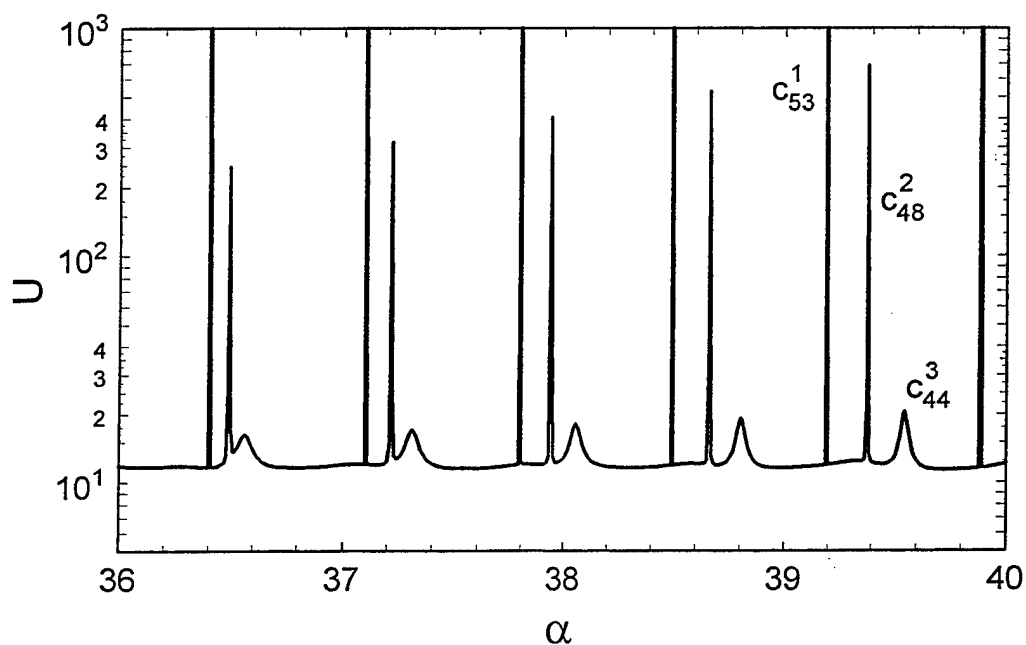
FIG 2. Electric wave case total electromagnetic energy within the cylindrical particle (per unit length) as a function of size parameter. Plane wave illumination, $\bar{n} = (1.50, 0.00)$.
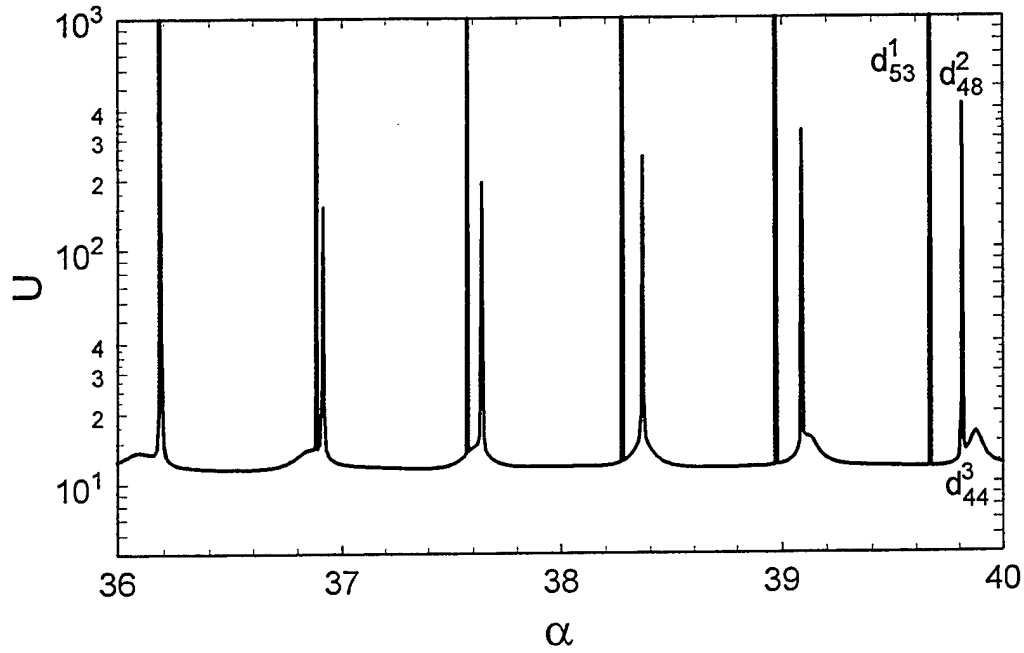
FIG 3. Magnetic wave case total electromagnetic energy within the cylindrical particle (per unit length) as a function of size parameter. Plane wave illumination, $\tilde{n} = (1.50, 0.00)$.

FIG 4. Electric wave case total electromagnetic energy within the cylindrical particle (per unit length) for the c_{53}^1, c_{48}^2, and c_{44}^3 resonances as a function of focal point positioning ($\tilde{x}_0 = 0$). The dotted line represents a nonresonance case ($\alpha = 39.0$). Focused light sheet illumination with $\tilde{w}_0 = 0.25$.
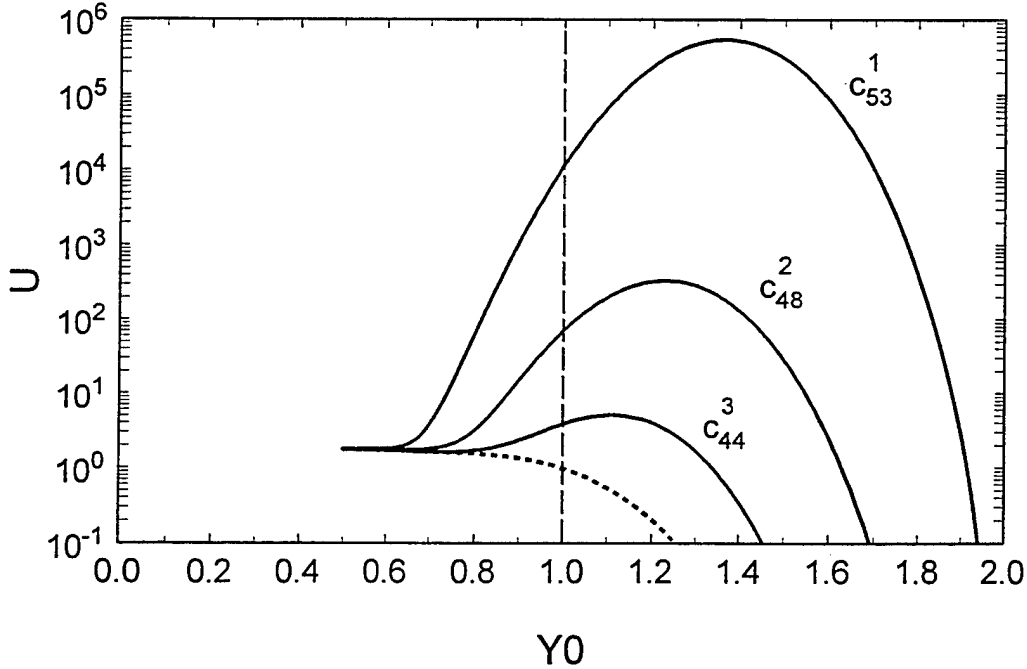
81
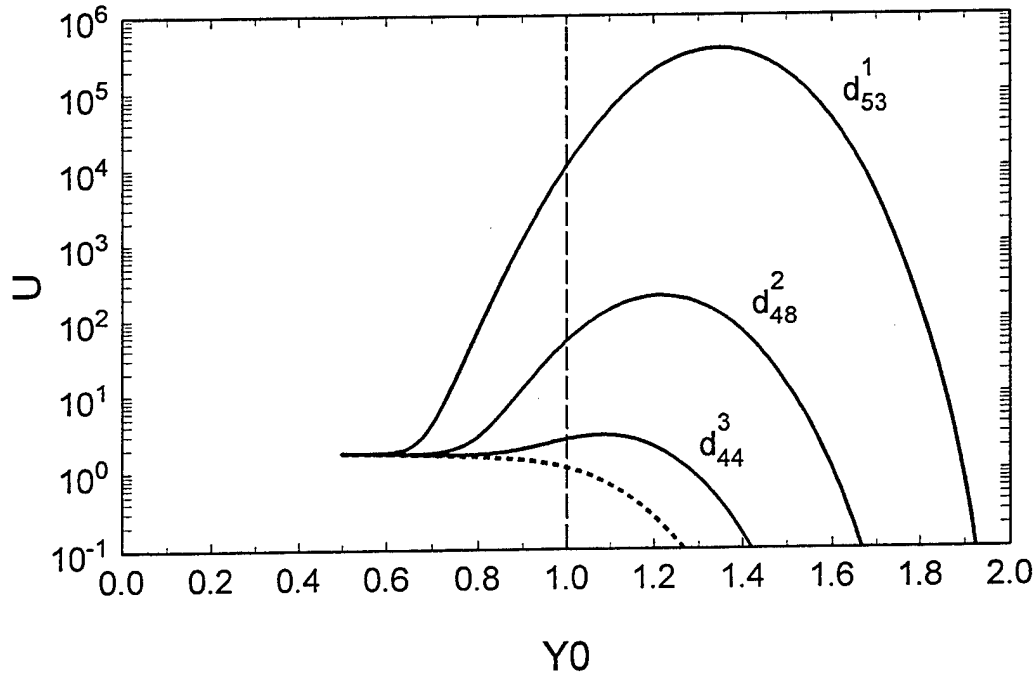
FIG 5. Magnetic wave case total electromagnetic energy within the cylindrical particle (per unit length) for the d_{53}^1, d_{48}^2, and d_{44}^3 resonances as a function of focal point positioning ($\tilde{x}_0 = 0$). The dotted line represents a nonresonance case ($\alpha = 39.5$). Focused light sheet illumination with $\tilde{w}_0 = 0.25$.

TABLE I. Comparison of the calculated focal point location for maximum resonance excitation (y_0/a) with the corresponding localization principle prediction (y0_lp/a) for first, second, and third order electric wave and magnetic wave resonances

res	α	U	y0/a	y0_lp/a
c53(1)	39.19199826	1,091,177	1.366	1.365
c48(2)	39.38244	682.67	1.231	1.232
c44(3)	39.550	20.446	1.109	1.125
d53(1)	39.668899131	739,718	1.350	1.349
d48(2)	39.81304	416.78	1.217	1.218
d44(3)	39.875	16.262	1.083	1.116

82

Recovery of the Properties of Layered Spheres Using Laser Pulses or a Series of Plane Wave Exposures at Different Wavelengths

O.I. Sindoni and D.K. Cohoon

U.S. Army Edgewood Research, Development and Engineering Center
Aberdeen Proving Ground, MD 21010-5423

Contents

Sizing of aerosol particles is important in motor and heating unit design and other industrial applications as well as the study of clouds and effluents from smoke stacks. Discrimination between layered and nonlayered spheres can help us tell the difference between man made aerosols such as biowarfare agent clouds and naturally occuring aerosols. This could also give us another way to measure properties of materials used in coatings and could benchmark more general computer codes for electromagnetically imaging penetrable magnetic materials.

Novel aspects of our inversion include chain affine transforms for accurate, exact formula Jacobians in homotopy methods and a fast back projection algorithm for use in conjunction with a gradient search or Levenberg Marcquardt type methods. Another feature includes derivatives of spherical Bessel and Hankel functions with respect to their index.

Inversion methods using a single frequency or a small number of frequencies or wavelengths are not as efficient. You need to have enough frequencies so that you can compute the derivative of the scattering coefficients with respect to frequency so that you can pull layer locations outside the arguments of transcendental functions.

1   Functions on Surfaces of Spheres

To solve the forward and inverse electromagnetic scattering problems for layered spheres requires a deeper understanding of special functions such as associated Legendre functions. Associated Legendre functions with complex indices were used by Hovhannessian ([3]) to describe scattering by spherical stuctures whose anisotropic permittivity tensor is given in Cartesian coordinates by

$$\bar{\bar{\epsilon}} = \begin{pmatrix} \epsilon & 0 & 0 \\ 0 & \epsilon & 0 \\ 0 & 0 & \epsilon_z \end{pmatrix}$$

We also need these functions to detail the interaction of sharply focused laser beams with spheres by carrying out expansions of spheres and to describe the interaction of mutually interacting spherical particles with electromagnetic fields.

1.1 Singular Differential Equations and Spheres

The Legendre function $P_n(z)$ is a regular solution of the ordinary differential equation,

$$\frac{d}{dz}\left((1-z^2)\frac{dP_n}{dz}\right) + n(n+1)P_n(z) = 0 \tag{1.1.1}$$

where n may be a complex number.

Several other representations of Legendre functions will help us calculate associated Legendre functions. The most useful representations are given by the following.

Proposition 1.1 *When n is a nonnegative integer, the Legendre function $P_n(z)$ is given by the Rodrigues's formula*

$$P_n(z) = \frac{1}{2^n n!}\left(\frac{d}{dz}\right)^n (z^2 - 1)^n \tag{1.1.2}$$

and by the Schläfli contour integral given by

$$P_n(z) = \frac{1}{2\pi i}\int_C \left(\frac{(\zeta^2 - 1)^n}{2^n)(\zeta - z)^{n+1}}\right) d\zeta \tag{1.1.3}$$

where C is any simple closed contour surrounding z and both are equal to each other and satisfy the Legendre differential equation (1.1.1).

Proof of the proposition. If $f(\zeta)$ is analytic in a neighborhood U of z and if C is a simple closed curve surrounding z which is contained in U and whose interior is contained in U, then by the Cauchy integral theorem, we have

$$f(z) = \frac{1}{2\pi i}\int_C \frac{f(\zeta)}{(\zeta - z)}d\zeta \tag{1.1.4}$$

and if $\mathcal{Q}(n+1)$ is the assertion that

$$\left(\frac{d}{dz}\right)^n f(z) = \frac{n!}{2\pi i}\int_C \frac{f(\zeta)}{(\zeta - z)^{n+1}}d\zeta \tag{1.1.5}$$

84

then $\mathcal{Q}(1)$ is the Cauchy integral theorem and differentiating each side of equation (1.1.5) with respect to z gives

$$\left(\frac{d}{dz}\right)^{n+1} f(z) = \frac{n!}{2\pi i}(-(n+1)) \int_c \frac{f(\zeta)}{(\zeta - z)^{n+2}}(d/dz)(\zeta - z)d\zeta$$

$$\frac{(n+1)!}{2\pi i} \int_c \frac{f(\zeta)}{(\zeta - z)^{n+2}}d\zeta \tag{1.1.6}$$

which shows that $\mathcal{Q}(n+1)$ implies that $\mathcal{Q}(n+2)$ is true. Equation (1.1.4) implies that

$$(z^2 - 1)^n = \frac{1}{2\pi i} \int_c \left(\frac{(\zeta^2 - 1)^n}{\zeta - z}\right) d\zeta \tag{1.1.7}$$

and applying the *nth* deriviative operator $(d/d\zeta)^n$ to both sides of (1.1.7) implies that

$$\left(\frac{d}{dz}\right)^n (z^2 - 1)^n = \frac{1}{2\pi i} \left(\frac{d}{dz}\right)^n \int_c \left(\frac{(\zeta^2 - 1)^n}{\zeta - z}\right) d\zeta$$

$$= \left(\frac{n!}{2\pi i}\right) \int_c \left(\frac{(\zeta^2 - 1)^n}{(\zeta - z)^{n+1}}\right) d\zeta \tag{1.1.8}$$

Dividing both sides of (1.1.8) by $n!2^n$ tells us that

$$\frac{1}{2^n n!} \left(\frac{d}{dz}\right)^n (z^2 - 1)^n = \left(\frac{1}{2\pi i}\right) \int_c \left(\frac{(\zeta^2 - 1)^n}{2^n(\zeta - z)^{n+1}}\right) d\zeta \tag{1.1.9}$$

which proves that the Rodrigues's definition (1.1.2) and the Schlafli integral definition (1.1.3) of the Legendre function are equivalent.

It remains to show that the function $P_n(z)$ defined by equation (1.1.2) or equivalently by equation (1.1.3) satisfies the Legendre differential equation (1.1.1). This is accomplished via the following.

Proposition 1.2 *If $P_n(z)$ is defined by (1.1.3), then*

$$(1 - z^2) \left(\frac{d}{dz}\right)^2 P_n(z) - 2z \left(\frac{d}{dz}\right) P_n(z) + n(n+1)P_n(z)$$

$$\left(\frac{(n+1)(n+2)(1 - z^2)}{2\pi i}\right) \int_c \left(\frac{(\zeta^2 - 1)^n}{2^n(\zeta - z)^{n+3}}\right) d\zeta$$

$$- \left(\frac{(n+1)2z}{2\pi i}\right) \int_c \left(\frac{\zeta^2 - 1}{2^n(\zeta - z)^{n+2}}\right) d\zeta$$

$$+ \left(\frac{n(n+1)}{2\pi i}\right) \int_c \left(\frac{(\zeta^2 - 1)}{2^n(\zeta - z)^{n+1}}\right) d\zeta$$

$$= \frac{(n+1)}{2\pi i} \int_c \left\{\frac{d}{d\zeta}\left[\frac{(\zeta^2 - 1)^{n+1}}{(\zeta - z)^{n+2}}\right]\right\} d\zeta = 0 \tag{1.1.10}$$

85

Proof of Proposition. That the left side of (1.1.10) is the substitution into Legendre's differential equation (1.1.1) of the represention of the Legendre function by (1.1.3). To prove the validity of equation (1.1.10) we rewrite the left side of (1.1.10), giving all fractions the same denominator, as

$$(1 - z^2)\left(\frac{d}{dz}\right)^2 P_n(z) \; - \; 2z\left(\frac{d}{dz}\right)P_n(z) \; + \; n(n+1)P_n(z) \; =$$

$$\frac{1}{2\pi i}\int_C\left(\frac{(\zeta^2-1)^n}{2^n(\zeta-z)^{n+3}}\right)\Big[(n+2)(n+1)(1-z^2) \; - \; 2z(n+1)(\zeta-z)$$

$$+ \; n(n+1)(\zeta-z)^2\Big]\,d\zeta$$

$$= \; \left(\frac{1}{2\pi i}\right)\int_C\left(\frac{(\zeta^2-1)^n}{2^n(\zeta-z)^{n+3}}\right)\Big[-2z\zeta(n+1)^2 \; + \; n(n+1)\zeta^2\Big]\,d\zeta \qquad (1.1.11)$$

It is interesting that there is no z^2 term in the numerator of the left side of (1.1.11). We complete the proof of the proposition by showing that the integrand of (1.1.11) is actually a derivative with respect to ζ. We calculate

$$(n+1)\frac{d}{d\zeta}\left(\frac{(\zeta^2-1)^{n+1}}{(\zeta-z)^{n+2}}\right) \; = \; (n+1)\left[\frac{(n+1)(\zeta^2-1)^n\cdot 2\zeta}{(\zeta-z)^{n+2}}\right.$$

$$\left. - \; \frac{(\zeta^2-1)^{n+1}\cdot(n+2)}{(\zeta-z)^{n+3}}\right] \; =$$

$$(n+1)\left[\frac{(\zeta^2-1)^n}{(\zeta-z)^{n+3}}\right]\Big[2\zeta\cdot(n+1)(\zeta-z) \; - \; (\zeta^2-1)(n+2)\Big]$$

$$= \; (n+1)\left[\frac{(\zeta^2-1)^n}{(\zeta-z)^{n+3}}\right]\Big[2\zeta\cdot(n+1)(\zeta-z) \; - \; (\zeta^2-1)(n+2)\Big]$$

2   Inversion Problem for Spheres

First we consider the problem of the inversion and determination of the properties of a homogeneous sphere if we had a knowledge of the expansion coefficients of the scattered radiation. We give a simple means of telling the difference between layered and nonlayered spheres. We give an analysis of inversion by electromagnetic pulse interaction

2.1   Telling the Difference between Layered and Homogeneous Spheres

We want to develop a relationship between the expansion coefficients used to represent the interrogating radiation and the expansion coefficients used to In a Mie scattering solution there are coefficients of the vector spherical harmonics that define the scattered

electromagnetic radiation and the electric and magnetic vectors induced inside the spheres by the incoming electromagnetic radiation. These inside and outside expansion coefficients are related by simple transition matrices and even though there are an infinite number of these coefficients by orthogonality of the vector spherical harmonics over the surface of a sphere the relationship between fields inside and outside the sphere may be described by two by two matrices ([2]). One of these relationships is described by equation (3.7) of ([2]) and is given by

$$
\begin{pmatrix} Z^{(a,1)}_{(n,p)}(k_p R_p) & Z^{(a,3)}_{(n,p)}(k_p R_p) \\ W^{(a,1)}_{(n,p)}(k_p R_p) & W^{(a,3)}_{(n,p)}(k_p R_p) \end{pmatrix} \begin{pmatrix} a^{(p)}_{(m,n)} \\ \alpha^{(p)}_{(m,n)} \end{pmatrix} =
$$
$$
\begin{pmatrix} Z^{(a,1)}_{(n,p+1)}(k_{p+1} R_p) & Z^{(a,3)}_{(n,p+1)}(k_{p+1} R_p) \\ \rho_p W^{(a,1)}_{(n,p+1)}(k_{p+1} R_p) & \rho_p W^{(a,3)}_{(n,p+1)}(k_{p+1} R_p) \end{pmatrix} \begin{pmatrix} a^{(p+1)}_{(m,n)} \\ \alpha^{(p+1)}_{(m,n)} \end{pmatrix} \qquad (2.1.1)
$$

which in the paper ([2]) shows the relationship between the coefficients in layer p and the adjacent layer p+1 where

$$
\rho_p = \frac{\mu^{(p)} k_{p+1}}{\mu^{(p+1)} k_p} \qquad (2.1.2)
$$

We are interested in the special case where N =1, p =1, and of course where all of the $\alpha^{(p)}_{(m,n)}$ are equal to zero.

Solving this system we get a relationship between the known quantities $a^{(2)}_{(m,n)}$ and $\alpha^{(2)}_{(m,n)}$ that is given by

$$
a^{(2)}_{(m,n)} \left[\rho_1 W^{(a,1)}_{(n,2)}(k_0 R_1) Z^{(a,1)}_{(n,1)}(k_1 R_1) - W^{(a,1)}_{(n,1)}(k_1 R_1) Z^{(a,3)}_{(n,2)}(k_0 R_1) \right]
$$
$$
= \alpha^{(2)}_{(m,n)} \left[W^{(a,1)}_{(n,1)}(k_1 R_1) Z^{(a,3)}_{(n,2)}(k_0 R_1) - \rho_1 W^{(a,3)}_{(n,2)}(k_0 R_1) Z^{(a,1)}_{(n,1)}(k_1 R_1) \right] \qquad (2.1.3)
$$

Embodied in equation (2.1.3) is an infinite set of relationships which should, for a homogeneous sphere, all give the same value of radius and propagation constant k_1. If this is not true, then the sphere is layered.

The other expansion coefficients are related by similar matrix equations given by

$$
\begin{pmatrix} Z^{(b,1)}_{(n,p)}(k_p R_p) & Z^{(b,3)}_{(n,p)}(k_p R_p) \\ W^{(b,1)}_{(n,p)}(k_p R_p) & W^{(b,3)}_{(n,p)}(k_p R_p) \end{pmatrix} \begin{pmatrix} b^{(p)}_{(m,n)} \\ \beta^{(p)}_{(m,n)} \end{pmatrix} =
$$
$$
\begin{pmatrix} Z^{(b,1)}_{(n,p+1)}(k_{p+1} R_p) & Z^{(b,3)}_{(n,p+1)}(k_{p+1} R_p) \\ \rho_p W^{(b,1)}_{(n,p+1)}(k_{p+1} R_p) & \rho_p W^{(b,3)}_{(n,p+1)}(k_{p+1} R_p) \end{pmatrix} \begin{pmatrix} b^{(p+1)}_{(m,n)} \\ \beta^{(p+1)}_{(m,n)} \end{pmatrix} \qquad (2.1.4)
$$

We consider the case where $N = 1$, $p = 1$, and where all of the $\beta^{(p)}_{(m,n)}$ are equal to zero and get equations similar to (2.1.3).

2.2 Electromagnetic Pulse Inversion

In an inversion experiment a laser pulse is allowed to interact with a spherical structure and a grating is used to separate the scattered radiation by wavelength and the scattered power is measured at each wavelength. The inversion procedure is to

87

1. consider the frequencies at which the measurements are being made,

2. calculate the Fourier transform of the known incident laser pulse with respect to time and determine the amplitude of this Fourier transform at the frequencies at which measurements are being made,

3. solve the sphere scattering problem at the measured frequencies with a strength of the electric vector of the incoming radiation that corresponds to the amplitude of the Fourier transform of the electric vector of the incident pulse at that frequency assuming a known dispersion relationship for the classes of possible materials, and

4. compare these calculutions with experimental measurements and if all comparisions with measurements under the assumption that the sphere is homogeneous all give the same radius, then the sphere is homogeneous and if not the sphere is layered and assuming a shell thickness and running through the possible dispersion relationships determine the layer thickness.

We next give an exact formula for the interaction of a planar electromagnetic pulse with an N layered sphere where we assume that in the *pth* layer the propagation constant has the form

$$k_p^2 =$$

$$k_0^2 \left[1 + \sum_{j=1}^{M_p} \frac{\tilde{a}_{(j,p)}^2}{-\omega^2 + i\omega \cdot g_{(j,p)} + \omega_{(j,p)}^2} \right] \tag{2.2.1}$$

Equation (2.2.1) is known as a dispersion relationship. If we knew the form and the number of terms and we had enough data we could solve for the defining parameters in the Lorentzian equation (2.2.1). Writing k_p as an algebraic function we have that k_p will be analytic outside of branch cuts in the upper half plane. If we know the Fourier transform of the incoming laser pulse one can at any prescribed angular frequency ω determine the Fourier transform of electric vector in each region by an extension of the Mie theory. The pulse response can then be obtained by computing the inverse Fourier transform of this solution. To do this one makes the forward computation at the frequencies ω that will be used in a Gaussian quadrature Fourier inversion. Usually 8 points per sinusoidal hump will give about 12 to 16 places of accuracy in the inversion. There can be difficult subtraction problems associated with inversion around the branch cuts and great care has to be exercised.

References

[1] Colton, David and R. Kress. Inverse Acoustics and Electromagnetic Scattering. New York: Springer (1992)

[2] Cohoon, D. K. "An Exact Solution of Mie Type for Scattering by a Multilayer Anisotropic Sphere" JEWA. Volume 3, Number 5 (1989) pp 421 - 448

[3] Hovhannessian, S. S., and V. A. Baregamian. "The diffraction of a plane electromagnetic wave on an anisotropic sphere," Isdatelsva Akad. Nauk of Armenia. S. S. R. Physics Volume 16 (1981) pp 37-43

THIS PAGE INTENTIONALLY LEFT BLANK

Aerosol Backscattering Mueller Matrix Derived from Lidar: Theory and Experiment

Avishai Ben-David

Science and Technology Corporation
500 Edgewood Road, Suite 205, Edgewood, MD 21040 USA

Mueller matrices and the Stokes vector are important tools for describing the scattering properties of aerosols. Although the study of Mueller matrices and Stokes vectors was introduced in the 19th century, and since then has been addressed in classical text books many new studies concerning symmetry relationship and the properties and structure of Mueller matrices for aerosols continue to appear in the literature, adding much more needed insight to aerosol research with polarized light. Polarization diversity lidars are used to study the shape, orientation, composition, and properties of scatterers in clouds (e.g., water droplets and ice crystals) by analyzing the polarized backscattering lidar measurements, measurements that can be described by appropriate Mueller matrices and Stokes vectors.

In this paper we develop a Mueller matrix $\tilde{M}(\tilde{S}(\theta),\theta,\phi,F)$ such that the irradiance Stokes vector $\bar{G}(\theta,\phi)=\tilde{T}(\phi_a)\tilde{M}\tilde{T}(\phi_p)\bar{u}$ (W m^{-2}) is measured with a detector with a field of view F and a pair of real polarizer-analyzer (i.e. a polarizer with a finite extinction ratio and a transmission less than 100%) with transmission Mueller matrix $\tilde{T}(\phi_p)$ and $\tilde{T}(\phi_a)$ from single scattering at angle (θ,ϕ) by a scattering medium characterized with a Mueller matrix $\tilde{S}(\theta)$ and illuminated with an incident irradiance $\bar{u}$. The incident Stokes vector $\bar{u}$ is transmitted through a linear polarizer with transmission Mueller matrix $\tilde{T}(\phi_p)$ whose maximum transmission $t_\parallel^p$ is oriented at azimuthal angle ϕ_p. A detector placed in the xy plane behind a linear analyzer, with transmission Mueller matrix $\tilde{T}(\phi_a)$ whose maximum transmission $t_\parallel^a$ is oriented at azimuthal angle ϕ_a, measures the irradiance I which is the first component of the Stokes vector $\bar{G}=(I,Q,U,V)$.

The matrix $\tilde{M}(\tilde{S}(\theta),\theta,\phi,F)$ can be viewed as a Mueller matrix for the scattering process that contains the information about the scattering aerosols. The various elements of $\tilde{M}$ can be deduced from polarized measurements by conducting a set of polarized measurements with a suitable combination of polarizer and analyzer fore and aft the scattering medium. In this work we also show how **all the 3X3** elements of $\tilde{M}$ that affect linear polarization measurements can be deduced by combining three azimuthally integrated measurements (the commonly made lidar measurements from which **only 3** elements of $\tilde{M}$, m$_{11}$, m$_{22}$, and m$_{23}$ of the Mueller matrix $\tilde{M}$, and **only these three quantities can be deduced** from the linear polarization measurements. For a small field of view F, such that contributions to the measured irradiance $I(\phi_p,\phi_a)$ from terms of second order and higher in F are neglected, m$_{11}$, m$_{22}$, and m$_{23}$ are proportional to S$_{11}(\pi)$,

91

$S_{22}(\pi)-S_{33}(\pi)$, and $S_{23}(\pi)+S_{32}(\pi)$ for backscattering and are proportional to $S_{11}(0)$, $S_{22}(0)+S_{33}(0)$, and $S_{23}(0)-S_{32}(0)$ for forward scattering.

However, by combining three azimuthally integrated measurements (i.e., the commonly made lidar measurements) and eight azimuthally dependent measurements made through a spatial filter of angular half-width $\Delta\phi$ placed in the focal plane at azimuthal angle ϕ (measured in the xy plane counterclockwise from the x-axis) in front of the detector such that only scattered radiance within $\phi\pm\Delta\phi$ will strike the detector, and scattered radiance at any other azimuthal angle is blocked by the spatial filter, all nine Mueller matrix elements ($S_{11}(\pi)$, $S_{12}(\pi)$, $S_{13}(\pi)$, $S_{21}(\pi)$, $S_{22}(\pi)$, $S_{23}(\pi)$, $S_{31}(\pi)$, $S_{32}(\pi)$, and $S_{33}(\pi)$) which affect linear polarized radiation, may be deduced from the 11 polarized backscattering measurements.

An example of the Mueller matrix $\tilde{M}$ for atmospheric aerosol backscattering at Utah (a desert environment) derived from lidar polarized backscattering measurements at CO_2 wavelengths for horizontal path a few meters above the ground is presented. The lidar measurements are azimuthally integrated measurements and thus the Mueller matrix that can be derived from the polarized lidar measurements is expected to be a diagonal matrix. The Mueller matrix derived from our measurements is nearly a diagonal matrix with $m_{11}=S_{11}$, $m_{22}=(S_{22}-S_{33})/2$ and $m_{33}\cong-m_{22}$ as is expected for randomly oriented aerosols with axial symmetry. The ratio m_{22}/m_{11} is about 0.75 for which the linear depolarization ratio is about 0.15.
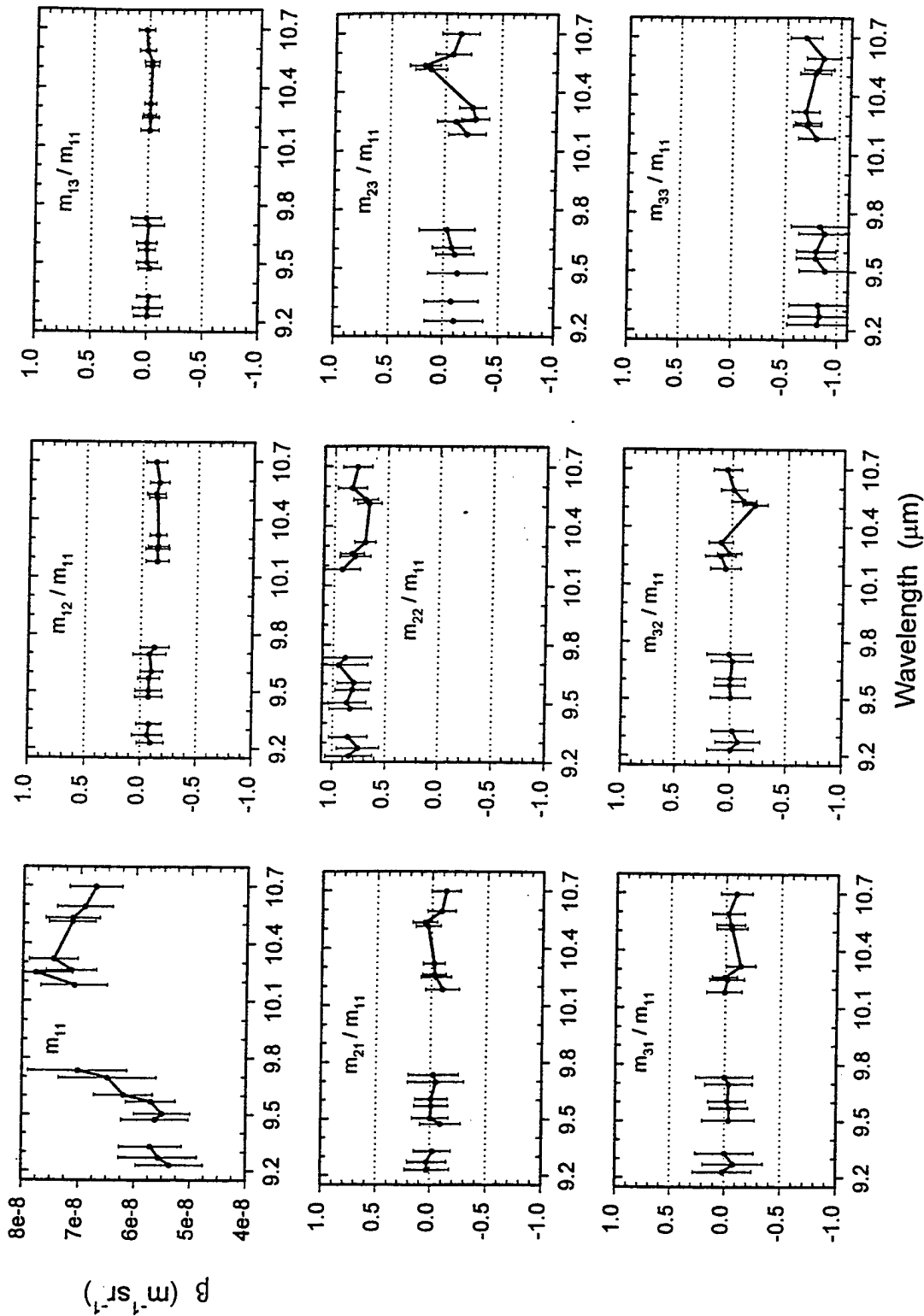
Figure 1 The Mueller matrix $\tilde{M}$ measured on June 25, 1995 between 11:08 and 11:45. At the time of the measurements the temperature, relative humidity, water vapor and ozone concentrations were 26.7±0.3 °C, 25.8±0.4%, 9 mb, and 33−37 ppb respectively.

THIS PAGE INTENTIONALLY LEFT BLANK

Index A
Index of Authors

INDEX A
INDEX OF AUTHORS

Index B
Index of Authors' Organizations

INDEX B
INDEX OF AUTHOR'S ORGANIZATIONS

Appendix A
Group Photo

GROUP PHOTO
June 17, 1998

First Row (L to R): John Barton, Jacques Van Bokhoven, Carl Peterson, Ivy Sindoni, Agnes Akinyemi, Roger Engles, Paul DeLuca, Jana Kesavanathan, Bob Doherty, Bishun Khare, David Rosen, Avi Ben-David, David Cohoon.

Second Row (L to R): Perry Gray, Mark Rholfs, Peter Hairston, Rachid Dahmani, Willem Van De Merwe, Jozsef Czege, Richard Chang, Ed Stuebing, Z.Z. Li, Burt Bronk.

Third Row (L to R): Virginia Stockwell, Abraham Grossman, Tony Janiuk, Gorden Videen, Jerry Bottiger, Joseph Birmingham, Paul Pellegrino, Nicholas Fell, Steve Holler, Dennis Garvey, Andrew Poon, Seongsik Chang.

Fourth Row (L to R): Mark Clark, The-Hsun Chen, Alan Snelson, Yongle Pan, Gerald Rainey, Gerard Jennings.

Fifth Row (L to R): Bill Whitten, Jeff Ives, Hank Mottl, Patrick Nolan, Dave Pendleton, Steve Hill, Ron Pinnick.

101

APPENDIX A

THIS PAGE INTENTIONALLY LEFT BLANK

Appendix B
Attendees

APPENDIX B
ATTENDEES

A
Mr. William Adams
Agnes Akinyemi
Mr. David Anderson

B
Prof. John Barton
Avi Ben David
Kelly Bennett
Mr. Joseph Birmingham
Dr. Jerold R. Bottiger
Mr. James Brock
Dr. Burt Bronk

C
Dr. Charles Call
Dr. John C. Carpin
Chee W. Chan
Mr. Richard Chang
Seongsik Chang
Dr. The-Hsun (Bean) Chen
Mr. Ronald Cionco
Mr. Mark Clark
Mr. David Cohoon
Dr. Jozsef Cze'ge'

D
Rachid Dahmani
Mr. Paul Deluca
Mr. Robert Doherty

E
Mr. Roger Engels
Dr. Jay D. Eversole

F
Dr. Nicholas Fell
Mr. Dennis Flanigan
Ms. Traci Forney
Mr. Robert H. Frickel

G
Dennis M. Garvey
M.G. Giridharan
Dr. Perry Gray
Mr. John Green
Dr. Abraham Grossman
Dr. Kristan Gurton

H
Mr. Peter Hairston
Mr. Jeffery Hale
Phillip Hargis
Mr. Steven Hill
Stephen Holler

I
Dr. Jeffrey Ives
Dr. Michael Izenson

J
Mr. Anthony Janiuk
Prof. Gerard Jennings
Dr. Thomas Jeys

K
Dr. Jana Kesavanathan
Dr. Bishun Khare
Michael Kierzewski
Dr. Mark Kingsley
Vladimir Kogan
Michael Kuhlman

L
Martin Lahart
Prof. M. Howard Lee
Dr. Z.Z. Li
Dr./Prof. Paul Lovett

M
Prof. Andrew McFarland
Mr. Paul Morgan
Mr. Hank Mottl

N
Prof. Thomas Netzel
Dr. Stanley Niles
Dr. Patrick Nolan
Raphael Nudezman

O
Dr. Eugene Olajos
Mr. Nils Olson
Dr. Chun-Sing Orr

P
Yongle Pan
Dr. Paul Pellegrino
Dr. Carl Peterson
Mr. Kirkman Phelps
Dr. Ron Pinnick
Wing Poon
Dr. Alice Presley
Dr. John Presley

R
Mr. Gerald Rainey
Mr. Felix Reyes
Prof. George Ritchie
Mr. Mark Rohlfs
Dominick Roselle
David L. Rosen

S
Dr. Harry Salem
Dr. Mark Seaver
Dr. Orazio Sindoni
Dr. Marek A. Sitarski
Dr. Alan Snelson
Ms. Frances Stites
Dr. Virginia Stockwell
Dr. Edward Stuebing

T
Mr. Joe Traino

V
Dr. Jacques Van Bokhoven
Willem P. Van De Merwe
Dr. Gorden Videen

W
Dr. Michael Walter
Mr. Daniel Weber
Mr. William B. Whitten
Doug Winters
Mr. Daniel Wise

THIS PAGE INTENTIONALLY LEFT BLANK

Appendix C
Conference Agenda

SESSION TOPICS

I. AEROSOL PARTICLE GENERATION AND DYNAMICS
(Moderator: Edward Stuebing, Edgewood RDEC)

II. AEROSOL CHARACTERIZATION METHODS

A. Aerosol Samplers and Collectors (Moderator: Edward Stuebing, Edgewood RDEC)

B. Fluorescence (Moderator: Burt Bronk, Edgewood RDEC)

C. General (Moderator: Jerry Bottiger, Edgewood RDEC)

III. WORKSHOP: PREPARING, AEROSOLIZING AND CHARACTERIZING ERWINIA HERBICOLA
(Moderator: Edward Stuebing, Edgewood RDEC)

IV. POSTER PROGRAM (Moderator: Edward Stuebing, Edgewood RDEC)

The poster session is a notable feature of the Conference. Posters (3'x5' poster boards with mounted display items) are set up by researchers in accordance with their respective research interests. Researchers will give a brief review of their posters (slides may be included) in the auditorium, then all Conference attendees will move to the Seminar Area adjoining the auditorium to view posters and enjoy refreshments. Poster presentations may be made singly, in groups, or in conjunction with a talk.

V. OPTICAL PROPERTIES OF AEROSOLS

(Moderator: O.I. Sindoni, Edgewood RDEC)

TUESDAY, JUNE 16

0800 REGISTRATION (Held in the Seminar Area, Building E4811 with Coffee and Refreshments)

0945 OPENING REMARKS & EDGEWOOD RDEC AEROSOL PROGRAM OVERVIEW
      Edward W. Stuebing, Team Leader, Aerosol Sciences and Technology (Edgewood RDEC)

      ADMINISTRATIVE ANNOUNCEMENTS
      Amy Coverstone (Battelle Edgewood Operations)

SESSION I - AEROSOL PARTICLE GENERATION AND DYNAMICS
(Moderator: Edward Stuebing , Edgewood RDEC)

1020 Airflow and Diffusion Simulations Over Variable Terrain
      R. Cionco (Army Research Laboratory)

1040 The Ink Jet Aerosol Generator
      J.R. Bottiger and P.J. Deluca (Edgewood RDEC)

1100 Application of Electrospray Aerosol Generation for Experimental Studies
      J. Kesavanathan, J. Carpin, R. Doherty, D. Wise, D. Weber, A. Akinyemi and E. Stuebing
      (Edgewood RDEC)

1120 A Micromachined High-Output Aerosol Generator
      M.G. Izenson and J.J Barry and (Creare, Inc.)

1140 **LUNCH**

SESSION II. - AEROSOL CHARACTERIZATION METHODS

      A. Aerosol Samplers and Collectors (Moderator: Edward Stuebing, Edgewood RDEC)

1315 An Isokinetic and Isoaxial Sampler for Outdoor Aerosols
      R.W. Doherty, P.J. Deluca, D.W. Jones, D.J. Weber (Edgewood RDEC) and E. Parry (NSWC)

1335 Sampling, Transport, and Collection of Bioaerosols
      A.McFarland, C.A. Ortiz and N.K. Anand (Texas A & M Univ.)

1430 **BREAK**

1530 XMX-1 Aerosol Concentrator
      H. Mottl (Dycor)

1550 Aerosol Collection into Fluids with Micromachined Devices
      J. Birmingham, C. Call, V. Kenning, P. Call and Yin-Fong Si (Mesosystems Technology Inc.)

      B. Fluorescence (Moderator: Burt Bronk, Edgewood RDEC)

1610 The 440-nm Fluorescence Band of Cultured Bacteria in Solution and on Surfaces
      P. Hargis (Sandia National Lab)

1630 **ADJOURN**

SESSION II. - AEROSOL CHARACTERIZATION METHODS (cont'd)

B. Fluorescence cont'd (Moderator: Burt Bronk, Edgewood RDEC)

0830   Fluorescence of Microparticles: Dependence on Size, Concentration of Fluorophors, and Intensity
    S. Hill (Army Research Laboratory)

0850   Performance of FLAPS with Front-End Concentrator for Biological Detection at JFT 4
    L. Retfalvi and P. Cherrier (DRES - Canada)

0910   Ambient Aerosol Analysis Using Fluorescence and Size
    M. Seaver, J. Eversole and D. Roselle (Naval Research Laboratory)

0930   Bio-aerosol Fluorescence Sensor
    T. Jeys, R. Brady, V. Daneu, S. DiCecca, N. Newbury, C. Primmerman, G. Rowe, A. Sanchez (MIT Lincoln Lab), F. Reyes and R. Smardzewski (Edgewood RDEC)

0950   **BREAK**

SESSION III - WORKSHOP: PREPARING, AEROSOLIZING AND CHARACTERIZING ERWINIA HERBICOLA
(Moderator: Edward Stuebing, Edgewood RDEC)

1020   Safety and Environmental Characteristics of Erwinia herbicola and Its Use in Outdoor Agriculture Trials
    V. Stockwell (Oregon State Univ.)

1035   The Use of Erwinia herbicola for Field Trials at DRES
    M. Spence (DRES)

1050   Erwinia herbicola Microbiology Methodology for Production and Assay
    D. Winters (Dugway Proving Ground)

1105   Aerosolizing and Collecting Erwinia herbicola at Dugway Proving Ground
    F. Stites (Dugway Proving Ground)

1120   Discussion

1150   **LUNCH**

SESSION II. - AEROSOL CHARACTERIZATION METHODS (cont'd)

C. General (Moderator: Jerry Bottiger, Edgewood RDEC)

1315   Chemical Composition and Optical Constants of Cometary Aerosols
    B. Khare (NASA AMES Research Center), E. Arakawa, S.J. Clemett, T. Vo-Dinh and D. Cruikshank (Oak Ridge National Labs)

1335   Bacterial Endospore Detection by Forming a Terbium Complex with a Distinctive Photoluminescence Spectrum
    D. Rosen, J. Gillespie and P. Pellegrino (Army Research Laboratory)

1355   Elastic Scattering from Spheres, Spheroids and Clusters
    J. Bottiger (Edgewood RDEC)

SESSION II. - AEROSOL CHARACTERIZATION METHODS (cont'd)

1415 Acoustic Levitation of Large Water Drops with Inclusions and Transition to Clusters
   S. Holler , Y. Zheng, R. Apfel, R. Chang (Yale University) and S. Hill (Army Research Laboratory)

SESSION IV - POSTER PROGRAM
(Moderator: Edward Stuebing, Edgewood RDEC)

1435 Poster Previews Followed by Poster Viewing

   Aerosol Collection into Fluids with Micromachined Devices
   J. Birmingham, C. Call, V. Kenning, P. Call and Yin-Fong Si (Mesosystems Tech)

   Update on Latest Advances in PHTLAAS Technology
   S. Zaromb, D. Reilly and D. Miller (Zaromb Technology)

   Background Bioaerosol Measurements at Mace Head, on the West Coast of Ireland
   S. Jennings and C. Kenny (University of Galway)

   Two-dimensional Elastic Scattering Angular Patterns from Spheres, Spheroids, and Clusters
   S. Holler, Y. Pan, R. Chang, J. Bottiger and S. Hill (Yale University)

   XMX-1 Aerosol Concentrator
   H. Mottl (Dycor)

   The Ink Jet Aerosol Generator
   J. Bottiger and P.J. Deluca (Edgewood RDEC)

   Diesel Soot Characterization Using Multi-Element Mueller Matrix Fitting
   A. Hunt, M. Quinley-Hunt and I. Sheperd (Lawrence Berkeley Lab, University of California)

   Microbial Light Scattering to Detect Metallic Toxins
   Z.Z. Li and B. Bronk (Edgewood RDEC)

1500 **GROUP PHOTO**

1700 **ADJOURN**

THURSDAY, JUNE 18

SESSION V - OPTICAL PROPERTIES OF AEROSOLS
(Moderator: O.I. Sindoni, Edgewood RDEC)

0830 Electromagnetic Field Calculations for an Arbitrary Focused Beam Incident Upon an Infinite Circular Cylinder
   J. Barton (University of Nebraska)

0850 Kramers - Kronig Relations with Log Kernel and Applications to the Phase Spectrum in the Drude Model
   H. Lee (University of Georgia)

SESSION V - OPTICAL PROPERTIES OF AEROSOLS (cont'd)
(Moderator: O.I. Sindoni, Edgewood RDEC)

0925 **BREAK**

1000 Calculation of MDRs by Hybrid Numerical Method for Solution of Maxwell Equations
    J. Brock and M-K Choi (University of Texas, Austin)

1020 Recovery of Properties of Layered Magnetic Cylinders using Obliquely Incident Radiation
    O.I. Sindoni and D. Cohoon (Edgewood RDEC)

1040 Lasing Images of Oblate and Prolate Microdroplets at Various Polar Angles
    S. Chang (Yale University)

1100 Global Methods of Inversion of Layered Spheres
    D. Cohoon and O.I. Sindoni (Edgewood RDEC)

1120 **LUNCH**

1300 Integral Equation Formulation of General Inverse Scattering
    D. Cohoon and O.I. Sindoni (Edgewood RDEC)

1320 Aerosol Backscattering Mueller Matrix from Lidar: Theory and Experiment
    A. Ben-David (Science and Technology Corp.)

1340 Spiral Cavity Modes in Circular and Deformed Optical Fiber
    W. Poon, R. Chang and J. Lock (Yale University)

1400 **CONFERENCE CLOSING**
    Edward Stuebing (Edgewood RDEC)

DISCUSSION GROUPS

A room in the Seminar Area has been reserved for the following Discussion Groups. Participation is open to all interested attendees. The time of the Discussion Group will be announced by the Host.

DAY	_TITLE_	_HOST_
WEDNESDAY	Fluorescence Detection of Biological Aerosols	Burt Bronk

AT A GLANCE...

Time	Tuesday June 16	Wednesday June 17	Thursday June 18
0800	Door Open Coffee / Donuts Registration	Door Open Coffee / Donuts	Door Open Coffee / Donuts
0900		II. Aerosol Characterization Methods (cont'd)	V. Optical Properties of Aerosols
			Break
		Break	
1000	Opening Remarks		V. Optical Properties of Aerosols (cont'd)
	I. Aerosol Particle Generation and Dynamics	III. Workshop:Preparing, Aerosolizing and Characterizing Erwinia herbicola	
1100			
	Lunch		Lunch
1200		Lunch	
1300			
	II. Aerosol Characterization Methods	II. Aerosol Characterization Methods (cont'd)	V. Optical Properties of Aerosols (cont'd)
1400			
	Break	IV. Poster Program	Conference Closing
1500			
	II. Aerosol Characterization Methods (cont'd)	Group Photo	
1600		IV. Poster Program (cont'd)	
	Adjourn		
1700		Adjourn	

Addendum

Delete

1020- Tuesday, June 16 R. Cionco (Army Research Lab) Airflow and Diffusion
Simulations Over Variable Terrain

0850- Wednesday, June 17 L. Retfalvi and P. Cherrier (DRES- Canada) Performance of
FLAPS with Front-End Concentrator for Biological Detection at JFT 4

1035- Wednesday, June 17 M. Spence (DRES) The Use of Erwinia herbicola for Field
Trials at DRES

1435- Wednesday, June 17 S. Zaromb, D. Reilly and D. Miller (Zaromb Technology)
Update on Latest Advances in PHTLAAS Technology

1435- Wednesday, June 17 A. Hunt, M. Quinley-Hunt, I. Sheperd (Lawrence Berkeley
Lab, University of California) Diesel Soot Characterization Using Multi-Element Mueller
Matrix Fitting

Add

1435- Wednesday, June 17 T. Netzel (Georgia State University) DNA-Based Photo-
Electrochemical Detection of Small Numbers of Pathogens

1400- Thursday, June 18 M. Rohlfs (University of Nebraska) Femtosecond
Backscattering From an Aerosol: Potential Standoff Detection Method

1420- Thursday, June 18 R. Cionco (Army Research Lab) Airflow and Diffusion
Simulations Over Variable Terrain

1440- Thursday, June 18 Conference Closing